

DEEP INELASTIC SCATTERING AT HERA

B. Foster*

*H.H. Wills Physics Laboratory, University of Bristol
Bristol, BS8 1TL. U.K.*

Received (September 20th, 1997)

Revised

To be published in International Journal of Modern Physics A

Results from the H1 and ZEUS experiments at HERA on deep inelastic scattering are reviewed. The data lead to a consistent picture of a steep rise in the F_2 structure function and in the gluon density within the proton. Important new information on the partonic structure of diffraction is emerging from H1 and ZEUS. The space-like region in which the weak and electromagnetic interactions become of equal strength is being explored for the first time. A possible excess of events at high x and Q^2 compared to the expectations of the Standard Model has been observed in both experiments.

1 Introduction

The study of the deep inelastic scattering of leptons on protons has been of profound importance to the development of particle physics. The pioneering electron-proton scattering experiments at SLAC in the 1960s provided evidence for the quark structure of matter. Neutrino experiments at CERN in the 1970s discovered the weak neutral current and thereby the key experimental underpinning of the Standard Model. The observation of scaling violations laid the foundations for our modern understanding of the strong interaction in terms of QCD. The current programme of deep inelastic scattering experiments has been revolutionised by the advent of the HERA electron proton storage ring, which has improved the resolution with which the proton can be explored in deep inelastic scattering by a factor of 100. Some indication of the tremendous increase in the kinematic region which can be explored at HERA is given in figure 1.

A varied programme of physics has developed at HERA, for instance in the physics of quasi-real photon interactions. This article will however concentrate on the results achieved at HERA by the H1 and ZEUS experiments in the area of deep inelastic scattering. These have had a major impact in several areas: the structure of the proton, the investigation of the mechanism of diffractive scattering, and the properties of the strong and electroweak interactions.

2 The HERA collider and the H1 and ZEUS experiments

HERA is 6.3 km in circumference and collides electrons or positrons of up to 30 GeV with protons of up to 820 GeV at four interaction points around the ring. The bunches of electrons and protons cross at each interaction point every 96 ns. The design luminosity is $1.5 \cdot 10^{31} \text{ cm}^{-2} \text{ s}^{-1}$. The electron storage ring is based on

*Supported by the UK Particle Physics and Astronomy Research Council;
email: b.foster@bristol.ac.uk

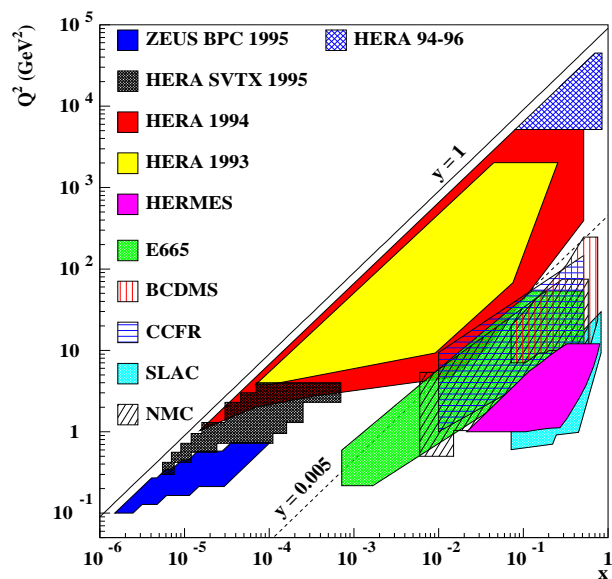


Fig. 1. The x - Q^2 plane which can be explored by the HERA experiments. The regions explored by ZEUS, H1 and HERMES in particular analyses are shown by the shaded regions. The enormous increase in phase space at HERA in comparison to the fixed target experiments (E665 etc.) is apparent.

conventional magnets but the high energy of the protons requires superconducting magnets providing a bending field of approximately 4.7 T. Both electrons and protons are produced by a complex of pre-accelerators and accelerated up to 14 GeV and 40 GeV respectively before being extracted from the PETRA storage ring and injected into HERA. HERA began operation in 1992 and has run with electrons and positrons of up to 27.7 GeV and protons of 820 GeV. The total luminosity delivered by HERA to the experiments is shown in figure 2. The maximum luminosity achieved by HERA up to spring 1997 was $\sim 0.9 \cdot 10^{31} \text{ cm}^{-2} \text{ s}^{-1}$. The majority of data has been taken with positrons although a relatively small data sample with electrons was taken in runs from 1992-1994.

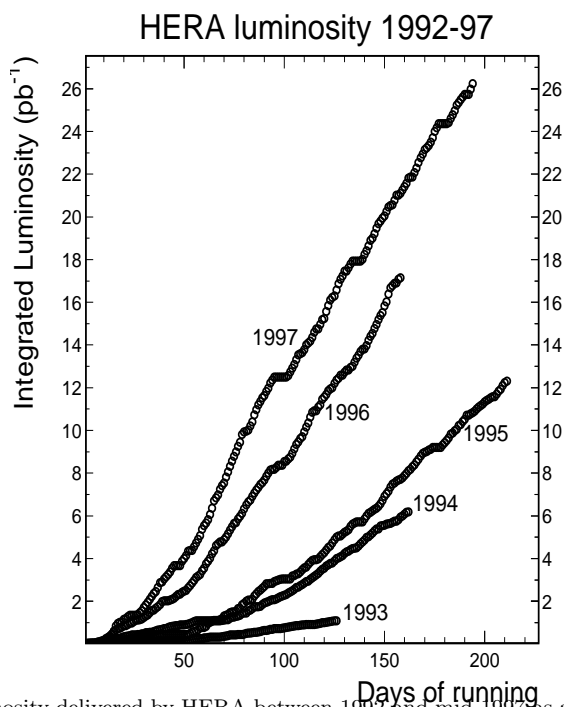


Fig. 2. The luminosity delivered by HERA between 1992 and mid-1997 as a function of day of the run.

The H1¹ and ZEUS² detectors are large, general-purpose colliding beam detectors designed for maximum hermeticity. The most important characteristics of HERA which influenced the design of the experiments were:

1. The asymmetric nature of the collisions between the low energy electrons or positrons and the high energy protons, which results in a decided asymmetry in energy deposition, with most of the energy in the proton or “forward” direction. This is reflected in H1 and ZEUS, which have deeper calorimeters and more complex instrumentation in the forward compared to the rear direction. The large centre of mass energy together with the boost means that very high energy jets may be produced and thus there is an emphasis on precise calorimetry in both experiments.
2. The very short beam crossing interval of 96 ns required the development of complex pipelined electronics to store the signals from the detectors until

such time as the fast logic at the first triggering level was able to decide if the event was of interest. The trigger electronics itself was also of unprecedented complexity.

The H1 and ZEUS collaborations eventually decided on rather different approaches to building an experiment to make accurate measurements in this difficult environment. However, both combine accurate and complex arrays of charged particle track detectors with large, high resolution calorimeters.

The major components of the H1 detector can be summarised as follows. H1 has recently installed a silicon vertex detector ³ close to the interaction point, inside a “jet chamber” ⁴ drift chamber with large drift cells and many radial measurements of tracks producing drift times and energy loss measurements. The tracking system is supplemented in the forward and rear directions by dedicated planar chambers ⁵. Surrounding the tracking detectors is an array of calorimeters. In the forward and barrel parts of the detector the calorimetry uses the lead/liquid Argon technique ⁶. In the rear direction H1 originally constructed a lead/scintillator sandwich calorimeter about one interaction length in depth. This was replaced for the 1995 data taking period with a so-called “spaghetti” calorimeter ⁷ consisting of lead and scintillating fibres with both electromagnetic and hadronic sections. The quoted resolution σ_E/E for the electromagnetic section of the liquid Argon calorimeter is $12\%/\sqrt{E} \oplus 0.01$, for the lead-scintillator calorimeter is $10\%/\sqrt{E} \oplus 0.42/E \oplus 0.03$ and for the upgraded spaghetti calorimeter is $7.1/\sqrt{E} \oplus 0.01$. The hadronic resolution of the liquid argon calorimeter is quoted as $0.50/\sqrt{E} \oplus 0.02$. Outside the calorimeter is a superconducting magnet producing a uniform magnetic field of 1.15 T. The iron return yoke is instrumented and acts as a “tail-catcher” to measure the leakage of hadronic showers as well as identify penetrating muons. The muon measurement is improved in the forward direction by a forward muon spectrometer.

ZEUS also had a vertex detector ⁸, a small drift chamber operating with DME which has a very slow drift velocity. This chamber was removed for the 1996 running period, and will be replaced by a silicon strip vertex detector ⁹. Surrounding this is the Central Tracking Detector (CTD) ¹⁰ which is based on small drift cells with wire planes tilted at 45° to the radial direction. The CTD provides many drift-time and energy loss measurements and in addition provides a fast first level trigger by using information on the z position of tracks obtained from a measurement of the time difference of the arrival time of pulses at both ends of the CTD ¹¹. The tracking is extended outside the central region by dedicated forward and rear tracking detectors. These are based on drift chamber layers with stereo measurements to give a space point. Between the three tracking layers in the forward detector are two layers of transition radiation detector. The forward tracking detector was only fully instrumented from the start of the 1995 data taking period. Outside the CTD is a small superconducting solenoid producing a magnetic field of 1.47 T. Surrounding the coil and tracking detectors is a uranium-scintillator calorimeter ¹² subdivided into a rear, barrel and forward detectors of differing thickness and tower size. The quoted resolution for electromagnetic showers is $\sigma/E = 18\%/\sqrt{E} \oplus 0.02$ and for hadrons is $\sigma/E = 35\%/\sqrt{E} \oplus 0.02$. The timing resolution of the calorimeter can be parameterised by the relation $1.5/\sqrt{E} \oplus 0.5ns$. The iron return yoke is instrumented to act as a tail catcher and to help in the identification of penetrating muons, which are also identified by dedicated muon chambers outside the iron. There is also a forward muon spectrometer which improves the measurement of high-momentum muons in the forward direction.

Both experiments use the bremsstrahlung process, $ep \rightarrow ep\gamma$, to measure the luminosity delivered by HERA. The cross-section for this process can be calculated in QED. Events are tagged by calorimetric detectors placed a substantial distance downstream of the main detectors in the electron direction. The luminosity is

proportional to the rate of coincidences between an electron calorimeter, positioned in order to intercept electrons which have lost energy and are therefore bent out of the beam by the HERA magnets, and a photon calorimeter, placed in a straight line from the interaction point in order to intercept the photon from the bremsstrahlung process. In practice, since the backgrounds are low and well-understood, the singles rate in the photon calorimeter is normally used as the luminosity measurement. The electron calorimeter is also used to tag photoproduction events via the coincidence of a scattered electron in the electron calorimeter with activity in the main ZEUS detector.

The accuracy of the luminosity determination has improved from typically 3.5% for ZEUS and 4.5% for H1 in 1993, to around 1.5%, although some difficulties with the bunch structure of HERA resulted in a somewhat larger uncertainty of about 2.3% in the 1996 data taking.

Both experiments have also installed detectors designed to tag “leading” protons carrying almost the full beam energy emanating from the interaction point. This is achieved via a “leading proton spectrometer”, which has a number of stations of Roman pots containing silicon strip detectors which can be lowered into the neighbourhood of the beam. The magnetic dipole elements of HERA act as a magnetic spectrometer so that very high energy protons can be tracked through the detector stations to give a reconstructed proton with very good energy resolution. Forward neutron calorimeters have also been installed. These are relatively small and crude devices intended to measure the energy of neutrons produced at the interaction point and carrying almost the full beam energy. More information on these detectors is given in sections 8.5 and 8.6.

Data from some of the major components of the H1 and ZEUS detectors can be seen in figures 3 and 4, which show typical neutral current and charged current deep inelastic scattering events as visualised by the event display programs.

3 A brief theoretical introduction to Deep Inelastic Scattering

3.1 Relativistic invariants

The scattering of a lepton from a proton at high Q^2 can be viewed as the elastic scattering of the lepton from a quark or antiquark inside the proton. As such the process can be fully described by two relativistic invariants. If the initial (final) four-momentum of the lepton is $k(k')$, the initial four-momentum of the proton is p , the fraction of the proton’s momentum carried by the struck quark is x and the final four-momentum of the hadronic system is p' then the following invariants may be constructed:

$$s = (p + k)^2 \quad (1)$$

$$t = (p - p')^2 \quad (2)$$

$$Q^2 = -q^2 = -(k' - k)^2 \quad (3)$$

$$y = \frac{p \cdot q}{p \cdot k} \quad (4)$$

$$W^2 = (p')^2 = (p + q)^2 \quad (5)$$

where s is the centre of mass energy squared, t is the four-momentum transfer squared between the proton and final state hadronic system, Q^2 is the four-momentum transfer squared between the lepton and the proton, y is the inelasticity

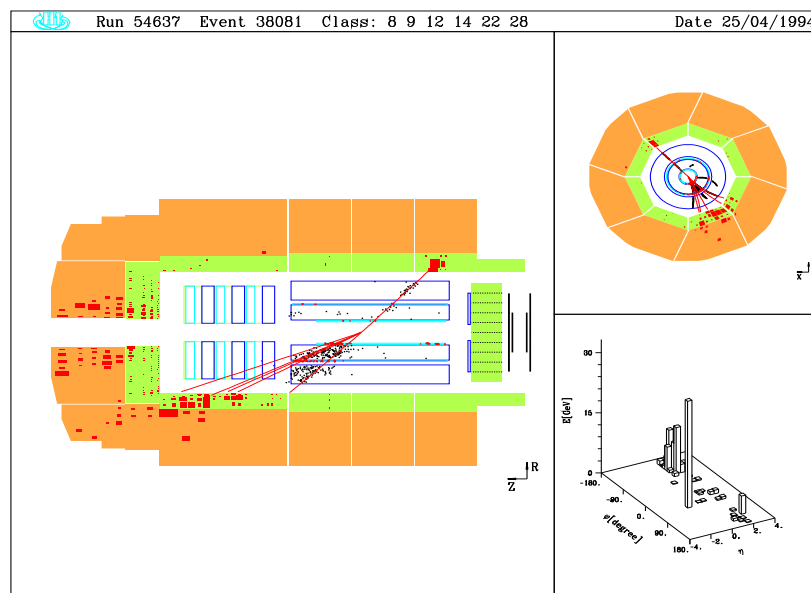


Fig. 3. A typical neutral current event as seen in the H1 experiment. The main view shows an $r - z$ section through the main H1 apparatus. The electron is clearly isolated from the other tracks in the event and extrapolates to a large electromagnetic deposit in the electromagnetic liquid argon calorimeter. The large energy deposit around the beam pipe due to the break-up of the incident proton can also be seen, as can the jet of hadrons corresponding to the current jet. The other two views show an $r - \phi$ section through the central detector and a two-dimensional map of the deposited energy.

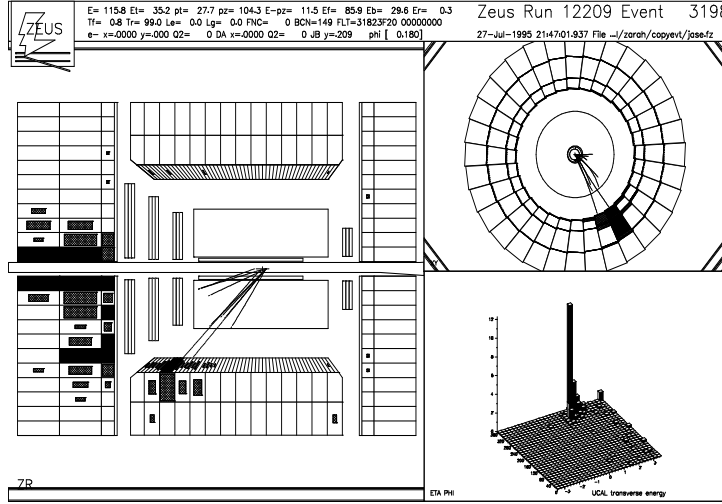


Fig. 4. A typical charged current DIS event observed in the ZEUS detector. The topology of this event is very similar to that of figure 3, except that there is no scattered electron visible. The reconstructed direction of the missing energy is such that it would be fully contained inside the detector, so that the absence of the electron cannot correspond to a loss due to the fact that the detector does not have perfect acceptance. The large missing energy is therefore assumed to correspond to a scattered neutrino.

of the scattered lepton and W^2 is the invariant mass squared of the final state hadrons. It is easy to show that energy-momentum conservation implies that

$$x = \frac{Q^2}{2p \cdot q} \quad (6)$$

and that thus

$$y = \frac{Q^2}{sx} \quad (7)$$

$$W^2 \sim Q^2 \frac{1-x}{x} \quad (8)$$

Since DIS at a given s can be specified by any two of these invariants we are free to choose the most convenient; we will normally use x and Q^2 .

3.2 Parton evolution

One of the most important experimental observations of modern particle physics has been the discovery of so-called “scaling violations”, in which the simple, three valence quark, picture of the proton had to be abandoned in favour of a dynamic, evolving parton content driven by fundamental QCD processes. The experimentally observed evolution of the differential cross-sections as a function of the kinematic

variables implies a corresponding evolution of the parton distributions. The description of parton evolution involves many different aspects of QCD depending on the kinematic range of the measurements and thus is an important testing ground of the theory. A very brief discussion of the QCD treatment of parton evolution is included in this section in order to introduce the reader to any unfamiliar notation used in the field. However, the interested reader is strongly recommended to consult a standard text, such as Ellis, Stirling and Webber¹³ for a full exposition of this complex subject.

The evolution of the parton density in the proton away from the familiar static picture of three valence quarks bound by the exchange of gluons is driven by fundamental processes of QCD. The important processes are the tendency of quarks to radiate hard gluons, and of gluons to split into quark-antiquark and gluon-gluon pairs. The probability of such splittings depends on the gauge structure of QCD and the value of the strong coupling constant and its variation with the kinematic scale. Clearly the radiation of a hard gluon from a quark, and the splitting of a gluon into a quark-antiquark or gluon-gluon, decreases the four-momentum of the radiating quark and contributes to a growth in the number of low x partons which can be found within the proton. Since these processes are virtual, their duration is controlled by the uncertainty principle; thus probes with small wavelength able to localise transient phenomena are able to resolve more and more of these splittings. At large Q^2 it is therefore to be expected that the parton distributions would grow at small x and shrink at large x , as is observed in experiment. The form of the splitting functions given below in the limit as $x \rightarrow 0$ shows that it is significantly more likely for a gluon to split into a pair of gluons than a quark-antiquark. Since quarks also radiate gluons, producing a softer gluon as well as a softer quark, the sum of the quark and gluon splitting processes causes the gluon density to increase strongly as x falls. This phenomenon of the growth of the gluon density at low x is one of the most notable characteristics of deep inelastic scattering at HERA, and forms one of the major threads in this review.

The parton splitting functions can be considered as the probability of a parton “containing” another type of parton with a fraction z of the initial momentum. The probability that a quark contains another quark of lower fractional momentum can then be written as $P_{qq}(z)$, that it contains a gluon as $P_{qg}(z)$, that a gluon contains as quark as $P_{gq}(z)$ and finally that a gluon contains a lower momentum gluon as $P_{gg}(z)$. These different processes are shown schematically in figure 5. Clearly the existence of such branchings couples the quark density in the proton to the gluon density, and vice-versa, so that the evolution of the parton densities follows a set of coupled integro-differential equations as a function of the momentum scale, known as the Altarelli-Parisi, or Dokshitzer-Gribov-Lipatov-Altarelli-Parisi (DGLAP) equations¹⁴. These can be written as

$$t \frac{\partial}{\partial t} \begin{pmatrix} q_i(x, t) \\ g(x, t) \end{pmatrix} = \frac{\alpha_s(t)}{2\pi} \sum_{q_j, \bar{q}_j} \int_x^1 \frac{d\xi}{\xi} \cdot \begin{pmatrix} P_{q_i q_j} \left(\frac{x}{\xi}, \alpha_s(t) \right) & P_{q_i g} \left(\frac{x}{\xi}, \alpha_s(t) \right) \\ P_{g q_j} \left(\frac{x}{\xi}, \alpha_s(t) \right) & P_{g g} \left(\frac{x}{\xi}, \alpha_s(t) \right) \end{pmatrix} \begin{pmatrix} q_j(\xi, t) \\ g(\xi, t) \end{pmatrix} \quad (9)$$

where t is the squared momentum scale of interest and $q_i(x, t), g(x, t)$ are the quark and gluon densities. Each of the splitting functions has a perturbative expansion in powers of α_s , and it can be shown in general that

$$xP(x, \alpha_s) = \sum_{n=0}^{\infty} \left(\frac{\alpha_s}{2\pi} \right)^n \left[\sum_{m=0}^n A_m^{(n)} (\ln 1/x)^m + x\bar{P}^{(n)}(x) \right] \quad (10)$$

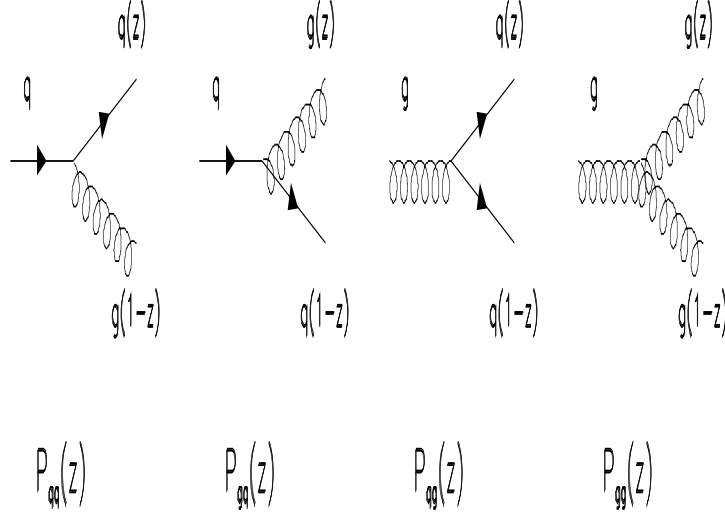


Fig. 5. The parton branchings described by the four Altarelli-Parisi splitting functions.

where $P = P_{q_i q_j}, P_{q_i g}$ etc. and $A_m^{(n)}$ are calculable coefficients. The $\bar{P}(x)$ terms correspond to expansion in terms of $\ln Q^2$. Both the leading order and next-to-leading order forms of the DGLAP splitting functions have been calculated; they depend upon the group structure of QCD. To illustrate the rather simple form of the splitting functions, we show below the leading order expressions:

$$\begin{aligned}
 P_{qq}^{(0)}(x) &= \frac{4}{3} \left\{ \frac{1+x^2}{(1-x)_+} + \frac{3}{2} \delta(1-x) \right\} \\
 P_{qg}^{(0)}(x) &= \frac{1}{2} \{ x^2 + (1-x)^2 \} \\
 P_{gq}^{(0)}(x) &= \frac{4}{3} \left\{ \frac{1+(1-x)^2}{x} \right\} \\
 P_{gg}^{(0)}(x) &= 6 \left\{ \frac{x}{(1-x)_+} + \frac{1-x}{x} + x(1-x) \right\} \\
 &+ \delta(1-x) \frac{(33-2n_f)}{6}
 \end{aligned} \tag{11}$$

where the $+$ subscript implies continuity from below as $x \rightarrow 1$.

The existence of both $\ln Q^2$ and $\ln 1/x$ terms in the perturbative expansion of equation 10 can be traced to the fact that the transverse momentum, k_t , which is developed in the quark-gluon splitting process[†] must be integrated over to produce an observable quantity. This integral appears in the calculation of observables in

[†]This is another symptom of the breakdown of the quark-parton model, which assumes that partons have zero k_t .

the form of an integral over the virtuality $|k^2|$

$$\int^{k_{max}^2} \frac{d|k^2|}{|k^2|} \quad (12)$$

where $k_{max}^2 = Q^2/x$. The expansion given in equation 10 is in general truncated, depending on the kinematic conditions, to produce several well-known approximations. The standard leading order (LO) approximation is given by ignoring all terms except for those with $n, m = 0$ and $\overline{P}^{(1)}$; the NLO approximation keeps terms in $n, m = 0, 1$ plus $\overline{P}^{(0)}, \overline{P}^{(1)}$; the double-leading log. approximation (DLA) has $n, m = 0$; the leading logarithm approximation in $1/x$ has $n \geq 0, m = n$, etc. The latter approximation is resummed by the BFKL equation¹⁵, and is appropriate when Q^2 is small and $1/x$ very large; the DGLAP equation by contrast is appropriate for Q^2 much larger than $1/x$. Whereas the DGLAP equation corresponds to considering the gluon emission to be strongly ordered in k_t , the BFKL equation is not ordered in k_t , but rather in x . It would be useful to have a formalism which was valid and soluble in all kinematic ranges; work to this end is reported below in section 4.2.

The limits of applicability of these various approximations is one of the interesting areas of QCD which can in principle be studied at HERA, where the increased kinematic region available compared to fixed target experiments means that regions where Q^2 is very much greater than $1/x$, and *vice-versa*, can be investigated. It may be possible to establish the breakdown of “normal” DGLAP evolution and the applicability of BFKL evolution. Such studies form another of the major threads of this review.

3.3 Differential cross-sections in DIS

Equation 13 shows the general form for the spin-averaged neutral current differential cross-section in the one-boson exchange approximation in terms of the structure functions F_1 , F_2 and F_3 .

$$\begin{aligned} \frac{d^2\sigma}{dx dQ^2} &= \frac{2\pi\alpha^2}{xQ^4} [2xy^2 F_1 + 2(1-y)F_2 \\ &+ \{1 - (1-y)^2\}xF_3] \end{aligned} \quad (13)$$

The structure functions are products of quark distribution functions and the couplings of the current mediating the interaction. They are in general functions of the two invariants required to describe the interaction, x and Q^2 .

In the naive quark-parton model in which quarks are massless, have spin $\frac{1}{2}$ and in which they develop no p_T , the Callan-Gross relation¹⁶

$$2xF_1(x) = F_2(x) \quad (14)$$

is satisfied. In the QCD improved parton model p_T must be taken into account and this relation is violated. This is usually quantified by defining a longitudinal structure function, F_L , such that $F_L = F_2 - 2xF_1$. Substituting into equation 13 gives

$$\begin{aligned} \frac{d^2\sigma}{dx dQ^2} &= \frac{2\pi\alpha^2}{xQ^4} [\{1 + (1-y)^2\}F_2(x, Q^2) \\ &- y^2 F_L(x, Q^2) + \{1 - (1-y)^2\}xF_3(x, Q^2)] \end{aligned} \quad (15)$$

In general, the form of the structure functions beyond zeroth order (*vis.* the quark-parton model) depends on the renormalisation and factorisation scheme used. In the so-called ‘‘DIS’’ scheme¹⁷, the logarithmic singularity produced by collinear gluon emission is absorbed into the definition of the quark distribution, so that the structure functions can be expressed as

$$F_2(x, Q^2) = \sum_{f=u,d,s,c,b} A_f(Q^2) [xq_f(x, Q^2) + x\bar{q}_f(x, Q^2)] \quad (16)$$

$$xF_3(x, Q^2) = \pm \sum_{f=u,d,s,c,b} B_f(Q^2) [xq_f(x, Q^2) - x\bar{q}_f(x, Q^2)] \quad (17)$$

where the positive sign in the expression for xF_3 is appropriate to electron scattering, the negative sign to positron scattering. The parton distributions $q_f(x, Q^2)$ and $\bar{q}_f(x, Q^2)$ refer to quarks and anti-quarks of type f . The flavour dependent coefficients $A_f(Q^2)$ and $B_f(Q^2)$ contain the electric charge of the fermion, e_f , the electro-weak axial (c_A) and vector (c_V) coupling constants and propagator terms P_Z ,

$$A_f(Q^2) = e_f^2 - 2e_f c_V^e c_V^f P_Z + (c_V^e{}^2 + c_A^e{}^2)(c_V^f{}^2 + c_A^f{}^2) P_Z^2, \quad (18)$$

$$B_f(Q^2) = -2e_f c_A^e c_A^f P_Z + 4c_V^e c_V^f c_A^e c_A^f P_Z^2, \quad (19)$$

$$\text{where } P_Z = \frac{Q^2}{Q^2 + M_Z^2} \quad (20)$$

$$c_V^f = T_3^f - 2e_f \sin^2 \theta_W \quad (21)$$

$$c_A^f = T_3^f \quad (22)$$

$$\text{and } T_3^f = +\frac{1}{2} \text{ for } f = \nu, u, c, t \quad (23)$$

$$= -\frac{1}{2} \text{ for } f = e, d, s, b \quad (24)$$

In the $\overline{\text{MS}}$ scheme¹⁸, another scheme in common use, equations 16 and 17 have a more complex form. For example, F_2 is given in first order QCD by

$$F_2(x, Q^2) = \sum_{f=u,d,s,c,b} A_f(Q^2) \int_x^1 \frac{dy}{y} \left(\frac{x}{y}\right) \left[\left\{ \delta\left(1 - \frac{x}{y}\right) + \frac{\alpha_s}{2\pi} C_q^{\overline{\text{MS}}} \left(\frac{x}{y}\right) \right\} \right. \\ \left. \cdot (yq_f(y, Q^2) + y\bar{q}_f(y, Q^2)) + \left\{ \frac{\alpha_s}{2\pi} C_g^{\overline{\text{MS}}} \left(\frac{x}{y}\right) \right\} yg(y, Q^2) \right] \quad (25)$$

where $g(x, Q^2)$ is the gluon density in the proton, $\alpha_s(Q^2)$ is the QCD running coupling constant and $C_q(x)$ and $C_g(x)$ are scheme-dependent ‘‘coefficient functions’’, closely related to the integrals of the DGLAP splitting functions discussed in section 3.2.

In contrast, the longitudinal structure function contains no collinear divergence at first-order in QCD so that

$$F_L(x, Q^2) = \frac{\alpha_s(Q^2)}{2\pi} \sum_{f=u,d,s,c,b} A_f(Q^2) \left\{ 2 \int_x^1 \frac{dy}{y} \left(\frac{x}{y}\right)^2 \left(1 - \frac{x}{y}\right) yg(y, Q^2) \right. \\ \left. + \frac{4}{3} \int_x^1 \frac{dy}{y} \left(\frac{x}{y}\right)^2 [yq_f(y, Q^2) + y\bar{q}_f(y, Q^2)] \right\} \quad (26)$$

independent of the factorisation scheme employed. This can also be expressed in terms of F_2 as

$$F_L(x, Q^2) = \frac{\alpha_s(Q^2)}{2\pi} \left\{ \frac{4}{3} \int_x^1 \frac{dy}{y} \left(\frac{x}{y} \right) F_2(y, Q^2) + 2 \sum_{f=u,d,s,c,b} A_f(Q^2) \int_x^1 \frac{dy}{y} \left(\frac{x}{y} \right)^2 \left(1 - \frac{x}{y} \right) yg(y, Q^2) \right\} \quad (27)$$

These structure functions can be related to the differential cross-section, taking account of electroweak radiative corrections, e.g. virtual loops and photon bremsstrahlung¹⁹ via the term δ_r . Provided that $Q^2 \ll M_Z^2$ the terms proportional to P_Z can be neglected, $x F_3$ vanishes and equation 16 reduces to that for photon exchange. Equation 15 can then be written as:

$$\begin{aligned} \frac{d^2\sigma}{dx dQ^2} &= \frac{2\pi\alpha^2}{xQ^4} [\{1 + (1-y)^2\} F_2(x, Q^2) \\ &- y^2 F_L(x, Q^2)] (1 + \delta_r(x, Q^2)) \end{aligned} \quad (28)$$

Equation 28 shows that the differential cross-section for one-photon exchange is proportional to two structure functions, F_2 and F_L . However, it is only possible to isolate the contribution from F_L directly by measuring the cross-section at different centre of mass energies for fixed x and Q^2 . Since this is a difficult procedure at HERA this has not yet been attempted, although an indirect determination is reported in section 4.3. In order to determine F_2 from the differential cross-section data reported in section 4, the value of F_L has been assumed to be that given by QCD using parton densities from fits to many data sets including from fixed target DIS experiments. In the range of x, Q^2 used in the results presented here, F_L is generally expected to be much smaller than F_2 and suppressed by the factor y^2 in equation 28.

For charged current processes, the quark-parton model ignoring the b quark contribution will be sufficiently accurate for our purposes. This gives the following expressions for the spin-averaged electron and positron induced reactions respectively:

$$\begin{aligned} \left. \frac{d^2\sigma}{dx dQ^2} \right|_{e^-} &= \frac{G_F^2}{2\pi} \left(\frac{M_W^2}{M_W^2 + Q^2} \right)^2 \\ &2x \cdot \{u(x) + c(x) + (1-y)^2(\bar{d}(x) + \bar{s}(x))\} \end{aligned} \quad (29)$$

$$\begin{aligned} \left. \frac{d^2\sigma}{dx dQ^2} \right|_{e^+} &= \frac{G_F^2}{2\pi} \left(\frac{M_W^2}{M_W^2 + Q^2} \right)^2 \\ &2x \cdot \{\bar{u}(x) + \bar{c}(x) + (1-y)^2(d(x) + s(x))\} \end{aligned} \quad (30)$$

where $q(x), \bar{q}(x)$ etc. refer to the density distribution of the quark or antiquark of flavour q .

3.4 Reconstruction of the kinematic variables

As noted above, two invariants are required to specify inclusive deep inelastic scattering processes fully. Both the H1 and ZEUS detectors are sufficiently hermetic

that the invariants can be reconstructed from measurements on the electron, on the hadronic final state corresponding to the struck quark, or on a mixture of the two. The optimal method depends on the kinematic region of interest and on the properties and resolutions of the detectors. The size of the radiative corrections is also very dependent on the reconstruction method employed. The basic measurements made are the angles and energies of the electron and current jet, where the angles are defined with respect to the proton beam direction, i.e. $\theta_e = 180^\circ$ corresponds to zero electron scattering angle. From these angles and energies the following quantities can be constructed:

- **The Electron method**

$$y_e = 1 - \frac{E'_e}{E_e} \sin^2 \theta_e/2 \quad (31)$$

$$Q_e^2 = 4E_e E'_e \cos^2 \theta_e/2 \quad (32)$$

- **The Jacquet-Blondel ²⁰ (JB) method**

$$y_{JB} = \frac{\Sigma}{2E_e} \quad (33)$$

$$Q_{JB}^2 = 2E_e \frac{(p_\tau^h)^2}{2E_e - \Sigma} \quad (34)$$

where

$$\Sigma = \sum_i (E_i - p_{z,i}) \quad (35)$$

$$(p_\tau^h)^2 = \left(\sum_i p_{x,i} \right)^2 + \left(\sum_i p_{y,i} \right)^2 \quad (36)$$

where the summations exclude the scattered electron or positron.

- **The Double Angle (DA) ²¹ Method**

$$y_{DA} = \frac{\Sigma}{p_\tau^h \tan(\theta_e/2) + \Sigma} \quad (37)$$

$$Q_{DA}^2 = 4E_e^2 p_\tau^h \left[\frac{\cot(\theta_e/2)}{p_\tau^h \tan(\theta_e/2) + \Sigma} \right] \quad (38)$$

or alternatively

$$y_{DA} = \frac{\sin \theta_e (1 - \cos \gamma_h)}{\sin \gamma_h + \sin \theta_e - \sin(\gamma_h + \theta_e)} \quad (39)$$

$$Q_{DA}^2 = 4E_e^2 \frac{\sin \gamma_h (1 + \cos \theta_e)}{\sin \gamma_h + \sin \theta_e - \sin(\gamma_h + \theta_e)} \quad (40)$$

- **The Sigma²² Method**

$$y_{\Sigma} = \frac{\Sigma}{\Sigma + E'_e(1 - \cos \theta_e)} \quad (41)$$

$$Q_{\Sigma}^2 = \frac{E_e'^2 \sin^2 \theta_e}{1 - y_{\Sigma}} \quad (42)$$

- **The PT²³ Method**

This method is rather more complex than the others, and proceeds in two steps. In the first step, the event-by-event p_T balance is used to correct the hadronic energy estimate of y using a functional form derived from Monte Carlo studies. Then the electron, JB and DA methods using the corrected hadronic energy are combined to give the best reconstruction over the full kinematic range. In the ideal case

$$y = y_{JB} / \left(\frac{p_T^h}{p_T^e} \right) \quad (43)$$

However, hadronic energy flow between the proton remnant and the current jet causes a correction to this formula

$$y = y_{JB} / C \quad (44)$$

where C is determined from Monte Carlo as a function of $p_T^h/p_T^e, p_T^h$ and γ_h . At high y the balance between p_T^h and p_T^e is less efficient at correcting y , so that the Sigma method is used in this region. This corrected y is then used to calculate the hadronic angle γ_{PT} using

$$\cos \gamma_{PT} = \frac{(p_T^e)^2 - 4E_e^2 y^2}{(p_T^e)^2 + 4E_e^2 y^2} \quad (45)$$

which can then be used in equations 39 and 40.

In all cases x can be derived from any of the above methods using equation 7.

4 The quark substructure of the proton

4.1 Measurement of F_2

Both ZEUS and H1 published F_2 measurements from the data taken in 1992 and 1993^{24,25}. These results showed a rapid rise in F_2 as x decreases below 10^{-2} . Subsequent data taking, together with upgrades to the experimental apparatus in the two experiments, have resulted in a major improvement in both the kinematic range and the accuracy of the F_2 measurement. The most important factor here has been a decrease in the minimum scattering angle of the positron which can be used in the analysis due to improvements in instrumentation near to the beam pipe in the rear direction, i.e. the direction of the positron beam. In addition, some special runs were taken with the interaction vertex displaced by about 67 cm in the proton direction. This means that positrons scattered at even smaller angles, and hence lower Q^2 , emerge into the well instrumented and understood parts of the detector and hence can be accepted for the F_2 analysis. The experiments accumulated some

58 nb⁻¹ of shifted vertex data in the 1994 data taking period. In addition H1 utilised data accumulated from the small “proton satellite” bunches which accompany the main proton bunch in adjacent buckets. This data corresponds to an effective interaction point of 68 cm in the proton direction and gives an effective luminosity contribution of about 68 nb⁻¹.

In order to determine F_2 the following steps are carried out. Firstly a sample of DIS events is selected, basically by requiring an identified electron or positron in the main detector. The data are binned in x, Q^2 with bin sizes determined by detector resolution, statistics, migration in and out of the bin due to the finite resolution of the experiments, etc. Estimates of the background in each bin are made and the background statistically subtracted. The data are corrected for acceptance, radiative effects and migration via Monte Carlo simulation. Multiplying the corrected number of events by the appropriate kinematic factors shown in equation 28 and subtracting an estimate for F_L gives values of F_2 and hence the quark and antiquark densities in the chosen bins.

Several independent positron finding algorithms are used. ZEUS requires a minimum scattered positron energy of 10 GeV, whereas H1 requires 11 GeV. As discussed in section 3.4, the method of kinematic variable reconstruction employed varies between the experiments and in different kinematic regions. ZEUS uses the Electron Method for the low Q^2 data and the PT Method for $Q^2 > 3$ GeV², whereas H1 uses the Electron Method for $y > 0.15$ and the Sigma Method for $y < 0.15$. Both experiments use data from unpaired positron and proton bunches to show that the background from non- ep processes such as beam-gas interactions is very small over the entire kinematic range. The comparison of Monte Carlo simulation of DIS processes with the data shows excellent agreement except for kinematic regions where photoproduction background would be expected to be important. Photoproduction has a much larger total cross-section than DIS, and can form a background when the scattered positron escapes undetected down the beam pipe, but a fake positron is produced by a π^0 or γ produced in the hadronic final state. Since it is easier to fake low energy positrons by this mechanism than high energy positrons, this background becomes progressively more important at high y . Both experiments use MC simulation of photoproduction processes to estimate this background. These estimates can be cross-checked by examining the subset of photoproduction events which have the scattered electron detected in the luminosity monitor. In addition ZEUS uses fits to the data plotted as a function of the total $E - p_z$ in the event to estimate the photoproduction background, which occurs predominantly at $E - p_z \ll 2E_e$ in contrast to DIS which peaks at $E - p_z \sim 2E_e$. All of these methods give consistent results. The highest levels of photoproduction background occur at high- y and are typically $\sim 2\%$ in ZEUS and $\sim 3\%$ in H1. The F_L value is calculated from equation 26 using the GRV²⁶ (H1), or MRSA²⁷ (ZEUS) parton distributions (see section 4.2).

A careful estimation of the systematic error on the F_2 measurement has been carried out by both experiments. A great many systematic checks are necessary, and space limitations permit only a cursory summary here. The most important sources for ZEUS are the uncertainty on the efficiency of the electron finding algorithm at high y and the energy scale at low y . For H1 the most important uncertainties are also the energy scale at low y and the photoproduction background subtraction at high y and low Q^2 .

In addition to the runs taken with shifted event vertex, the large increase in data taken allowed the experiments to analyse events with an energetic photon produced by initial state radiation (ISR). Since such radiation produces an effective reduction in the energy of the deep inelastic scattering process, a positron scattered at a given angle corresponds to a lower Q^2 than would have been the case for an event at the nominal centre-of-mass energy. Thus this type of event extends the Q^2 reach of the experiment in a similar and complementary way to the shifted vertex running.

In H1, these events are isolated by the detection of a photon with energy greater than 4 GeV in the photon calorimeter of the luminosity monitor together with a scattered positron detected in the main detector with energy greater than 8 GeV. In ZEUS the photon energy requirement is between 6 and 18 GeV and additionally less than 3 GeV in the luminosity electron calorimeter, together with a scattered positron in the main detector with energy greater than 10 GeV. Many of the sources of systematic error associated with ISR events are similar to those associated with the nominal and shifted vertex data, although there are important and sizeable additional sources of uncertainty. These include the energy scale of the photon calorimeter of the luminosity monitor, the maximum energy allowed to be detected in the luminosity electron calorimeter (for ZEUS), the effect of F_L and higher order radiative corrections and the subtraction of the Bethe-Heitler background.

Figure 6 shows the 1994 F_2 data from H1²⁸ and ZEUS²⁹ together with the fixed target data at higher x from the BCDMS³⁰, NMC³¹ and E665³² experiments. The improvements in the detectors, the shifted vertex running and the increase in integrated luminosity has resulted in a major extension of both the accuracy and of the x , Q^2 reach of the measurements. It can be seen that there is good agreement between the ZEUS and H1 data points. The strong rise in F_2 as x decreases persists to the lowest values of Q^2 measured in 1994 data, $Q^2 \sim 1.5 \text{ GeV}^2$.

As will be discussed in the next section, there is considerable theoretical interest in measuring F_2 at very low Q^2 and x . Both H1 and ZEUS have been able to extend the range of F_2 measurement to very low x and Q^2 by improvements to their detectors. H1 replaced their rear calorimeter with a lead/scintillating fibre calorimeter⁷ with an energy resolution of $7.5\%/\sqrt{E(\text{GeV})} \oplus 2.5\%$ and a spatial resolution of about 4 mm. They have also added an 8-layer drift chamber which gives a precision of about 0.5 mm and 2.5 mm in the radial and azimuthal directions respectively. ZEUS added a ‘‘Beam pipe calorimeter’’, consisting of two tungsten-scintillator sandwich calorimeters placed in front of thin windows in the beam pipe at a distance of about 2.94 m from the interaction point. The detectors cover the positron scattering angle range from 17 to 34 mrad. The energy resolution of these devices is estimated to be $17\%/\sqrt{E(\text{GeV})}$. These upgrades greatly improve the electron identification capabilities of both experiments down to very small angles.

The kinematic variables are reconstructed by both experiments using the electron method. In addition, depending on the region of phase space considered, H1 uses the Sigma method while ZEUS uses the Jacquet-Blondel method. The data from H1³³ are shown in figure 7 and extend down to a Q^2 of 0.35 GeV^2 . The ZEUS data³⁴ extend to even lower values of Q^2 and x , reaching Q^2 of 0.11 GeV^2 .

4.2 Theoretical implications of F_2 measurement

We have seen above that the ZEUS and H1 collaborations have been able to make precision measurements of F_2 over an unprecedented range in both x and Q^2 . This has acted as a tremendous stimulant to theoretical activity, so that it is appropriate at this point to give an overview of some of this theoretical work. Within the framework of perturbative QCD there are several possible explanations for the strong rise of F_2 as x decreases. There are essentially three relevant issues. The first is the appropriate form of the evolution equations within the relevant kinematic range, i.e. whether Altarelli-Parisi (DGLAP)¹⁴, BFKL¹⁵, or indeed other forms are most appropriate. Secondly, the form of the non-perturbative input which is required in all models must be specified. Finally, the starting scale from which a perturbative evolution can be carried out must be decided upon. It is possible to get a good description of the data with various combinations of assumptions about these three factors. The experimental challenge is to measure accurately as large a number of independent quantities, such as F_2 , F_L , F_2^{charm} , etc., in as large a kinematic range

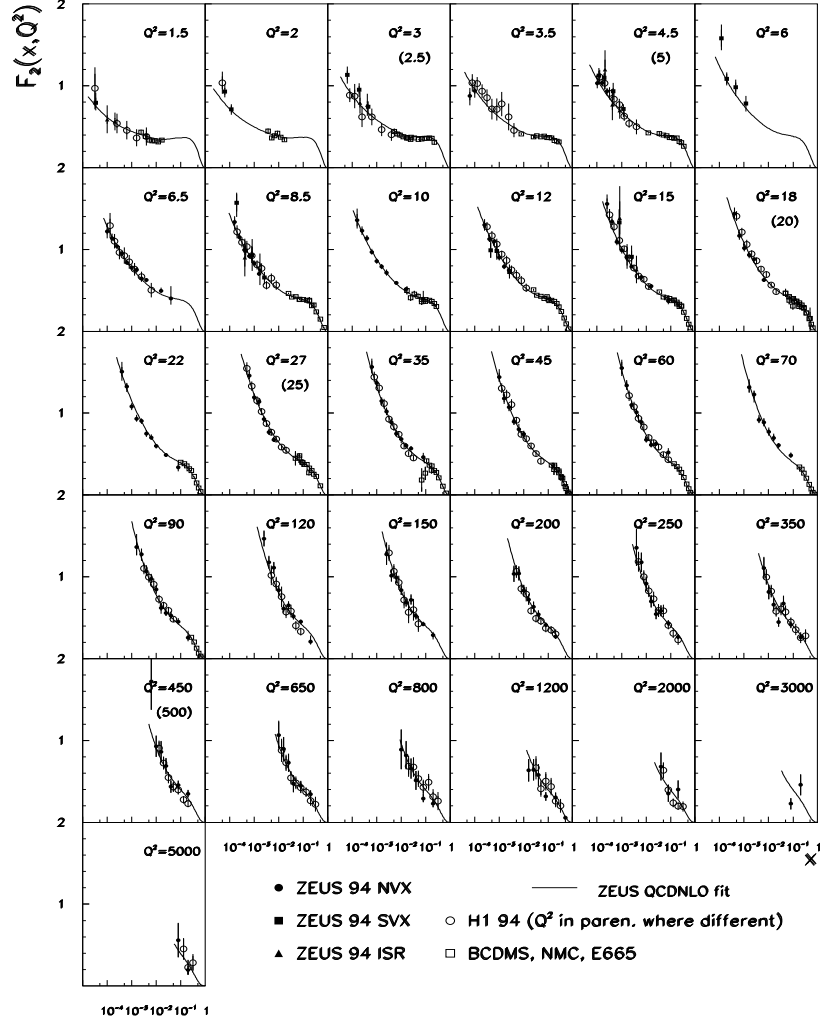


Fig. 6. Values of F_2 in selected Q^2 intervals as determined from the 1994 ZEUS (filled circles, squares, and triangles) and H1 (open circles) data plotted as a function of x . The error bars correspond to the statistical and systematic error added in quadrature, not including the uncertainty on the overall luminosity determination. In those bins with only one Q^2 value, both experiments have used identical binning, otherwise the data from the nearest equivalent Q^2 value have been used and the H1 and ZEUS values are denoted separately. The BCDMS, E665 and NMC data (open squares) are shown in those bins for which measurements have been published, predominantly at high x and low Q^2 . Also shown is a parameterisation from the ZEUS QCD fit to the data.

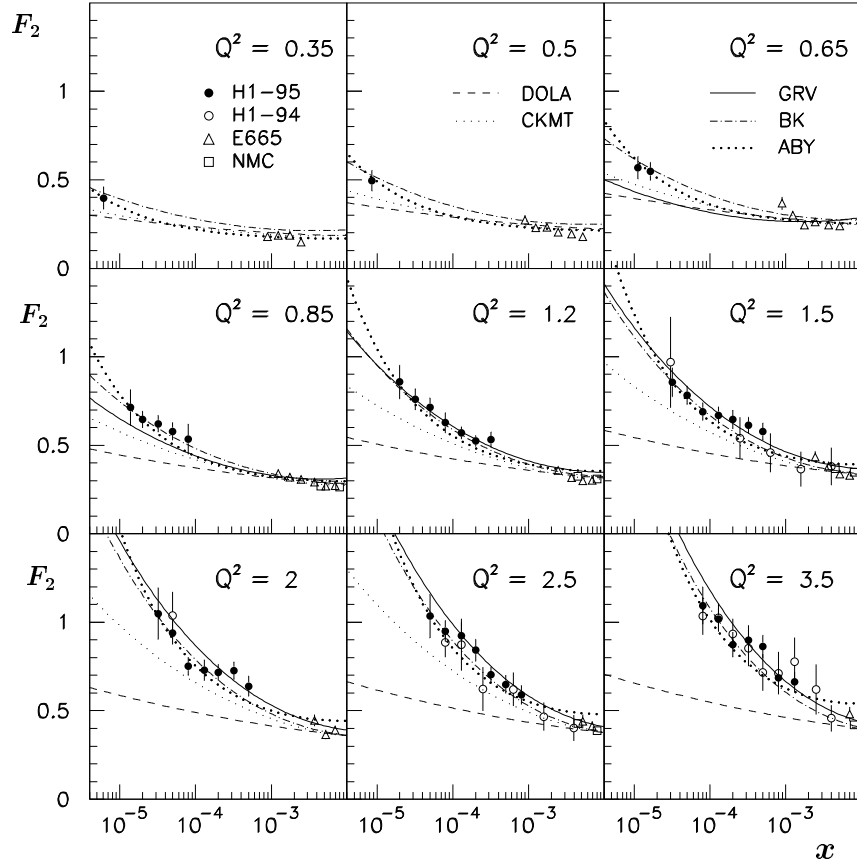


Fig. 7. H1 1995 data at low Q^2 together with previously published data from 1994²⁸ and data from the E665³² and NMC³¹ experiments. The predictions of Donnachie and Landshoff³⁵ (DOLA) are shown by a dashed line, those of Capella *et al.*³⁶ (CKMT) by a line with small dots, those of Badelek and Kwiecinski³⁷ (BK) by a dashed-dotted line, those of Glück *et al.*³⁸ (GRV) by a full line and those of Adel *et al.*³⁹ (ABY) by a line with large dots. Overall normalisation uncertainties are not included in the error bars.

as practicable, so that the theoretical implications are unambiguous.

Qualitatively, the rise of the structure functions at low x was predicted in the double leading log limit of QCD some twenty years ago⁴⁰. It seems possible to generate the strong rise of F_2 as x decreases from either the conventional DGLAP evolution in $\ln Q^2$, or from BFKL evolution in $\ln(1/x)$. At some point both these evolutions must be modified by the very large parton densities encountered at low x , where non-linear parton recombination effects⁴¹ must become important, although this is not expected to take place within the kinematic range accessible to HERA. Attempts have been made to embody both DGLAP and BFKL behaviour in a single equation based on angular ordering of gluon emission⁴², in the so-called CCFM equation, explicit solutions of which have been obtained for the small x region⁴³. In contrast to the above approaches, which are based on perturbative QCD and parton dynamics, other models based on Regge considerations, in which the virtual photon can be considered as a hadron, have been proposed. Such models, which predict a much softer rise with decreasing x were championed by Donnachie and Landshoff³⁵. However, the Donnachie and Landshoff approach, which generically has been so successful in describing the total cross-section data for a wide variety of “soft” hadronic processes, including real photoproduction, falls significantly below the F_2 data even at $Q^2 \sim 1 \text{ GeV}^2$.

Several groups have developed very sophisticated procedures to combine all data relevant to the determination of proton parton distributions. This data comes from the HERA experiments, fixed target DIS experiments, W^\pm data from $p\bar{p}$, Drell-Yan processes and direct photon production. Since parton distributions at very low Q^2 are not calculable perturbatively the procedure is to introduce simple functional forms for the parton distributions motivated by QCD at a sufficiently large Q^2 (typically $Q^2 \sim 4 \text{ GeV}^2$) that next to leading order Altarelli-Parisi evolution equations can be used to evolve to higher Q^2 . The data are then compared to predictions based on the parton distributions evolved to the relevant scale in order to obtain the best values for the free parameters in the assumed functional forms. The groups most active in performing such fits are Martin, Roberts and Stirling⁴⁴ and the CTEQ group⁴⁵. A somewhat different approach is adopted by Glück, Reya and Vogt²⁶. They utilise the fact that as $Q^2 \rightarrow 0$ parton distributions are fully constrained by the charge and momentum sum rules. By assuming valence-like distributions for the quarks at a very low starting Q^2 , in principle the gluon and sea distributions can be generated purely dynamically. However, it is found that such a procedure generates parton distributions which are too steep as x decreases⁴⁶, and in addition the theoretical validity of such a procedure is open to doubt⁴⁷. More theoretically respectable, although perhaps not so intuitively attractive, is to input “valence-like” distributions for both quarks and gluons fixed by high- x data at a larger though still very small Q^2 . The starting Q^2 value, Q_0^2 , is determined by the point at which the input gluon distribution is of the same order as the input u valence quark distribution. Q_0^2 is of order $0.3 - 0.5 \text{ GeV}^2$ in NLO QCD⁴⁸. Although there are quite large uncertainties on the value of Q_0^2 and on the valence-like distributions assumed at Q_0^2 , the effect of these is suppressed in the comparison with the HERA data by the long evolution distance. Figure 6 shows a comparison of the ZEUS QCD fit with the ZEUS and H1 F_2 data. Similarly good agreement is obtained with the parameterisations of GRV, MRS and CTEQ; all of these approaches have a rather similar number of free parameters.

It is instructive to plot F_2 converted to a total virtual photon-proton cross-section using the approximate relations

$$W^2 \sim \frac{Q^2}{x} \quad (46)$$

$$\sigma_{tot}^{\gamma^*p}(W^2, Q^2) \sim \frac{4\pi^2\alpha}{Q^2} F_2(x, Q^2) \quad (47)$$

based on the assumption that the ep cross-section can be factorised into the product of a photon flux factor and a virtual photon-proton cross-section. The σ^{γ^*p} thus obtained is plotted against W^2 for various Q^2 values in figure 8. Also shown is the

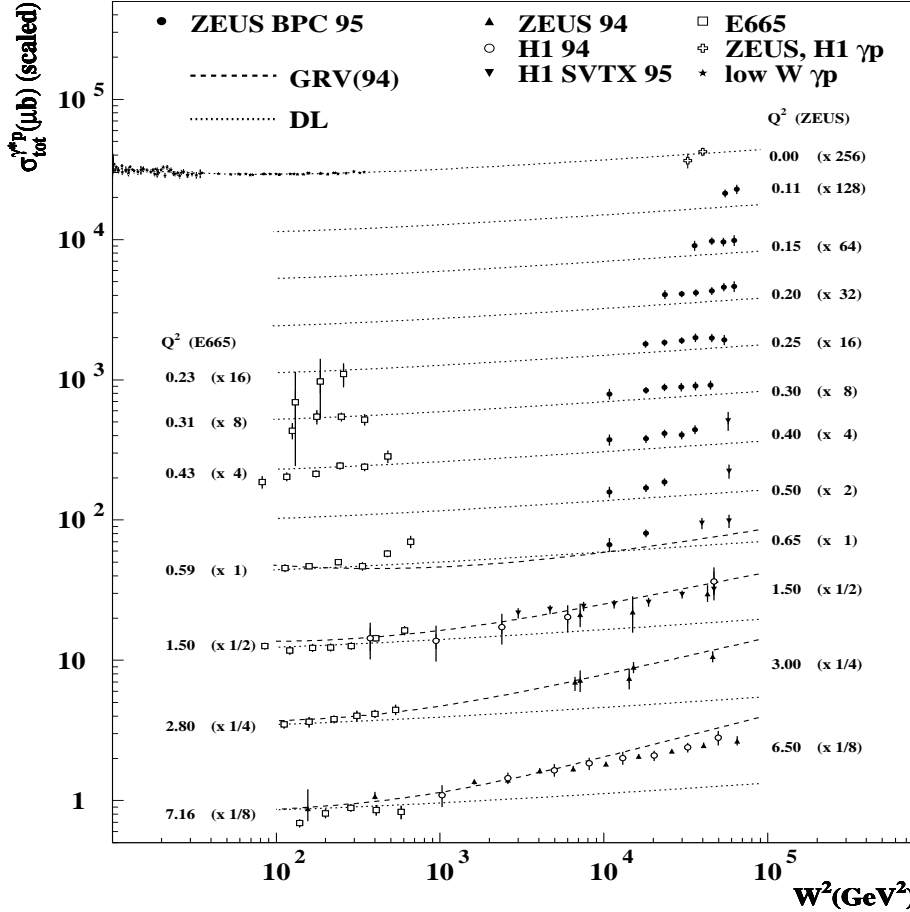


Fig. 8. Values of the total virtual photon-proton cross-section for various Q^2 (in GeV 2). The ZEUS and H1 points are obtained from a variety of analyses and run periods, including shifted vertex running (SVTX) and using the ZEUS Beam Pipe Calorimeter (BPC). The points at high W^2 and $Q^2 = 0$ are obtained by averaging the total photoproduction cross-section measurement of ZEUS⁴⁹ and H1⁵⁰. The remaining points at low W^2 are taken from a variety of fixed target experiments, in particular E665³². The dotted lines are parameterisations from Donnachie and Landshoff³⁵ while the dashed lines are parameterisations from GRV⁵¹.

total photoproduction cross-section as measured by ZEUS⁴⁹ and H1⁵⁰, together with data from fixed target experiments. The striking feature of this plot is that the steeply rising cross-section as a function of W^2 seen at high values of Q^2 persists down to the lowest measured values of Q^2 . However, as shown by the dotted line

in figure 8, at $Q^2 = 0$ the rise is less steep and is well represented by Donnachie-Landshoff (DL)-type models using a “soft” prescription based on Regge theory. There must therefore be a transition region between the “high” Q^2 region in which perturbative QCD gives a good description of the data and the photoproduction region which is well described by “soft” physics. This transition can be seen in figure 8 and also in the data from H1 shown in figure 7. Other Regge-inspired models shown in this figure, such as that of Capella *et al.* ³⁶, although nearer to the data than DL, still fail to give a good representation. Models based on perturbative QCD evolution, such as GRV, typically work well for higher Q^2 , $Q^2 \geq 1 \text{ GeV}^2$, but do not fit the data at lower Q^2 . The model of Badelek and Kwiecinski ³⁷ combines vector meson dominance with perturbative QCD in a smooth way. This model gives a good fit to the data. The model of Adel *et al.* ³⁹ assumes that perturbative QCD is applicable to very low Q^2 and modifies this behaviour by adding a singular “hard” contribution and assuming that the strong coupling “saturates” below 1 GeV^2 . This also leads to good agreement with the data.

It is interesting to take a very-simple minded approach to the data, determining a slope in W for each value of Q^2 . Such a plot for the ZEUS data shows a monotonic decrease in the slope until $Q^2 \sim 0.65 \text{ GeV}^2$, after which the slope is consistent with being flat or even slightly rising. Fits to a simple vector dominance model (VDM), in which the virtual photon is considered to consist of a superposition of light vector meson states and therefore to behave essentially as a hadron, give an acceptable χ^2 until Q^2 reaches 1 GeV^2 , after which the χ^2 becomes rapidly unacceptable. Similarly the QCD fit has a strong increase in χ^2 above about 0.65 GeV^2 . The transition between acceptable fits for these two different models of the interaction seems rather rapid ⁵². Clearly some variation of models which engineer a transition between “soft” and “hard” behaviour ought to be able to describe the data. In particular, Schildknecht and Spiesberger ⁵³ revive the old idea of generalised vector dominance ⁵⁴ (GVD) and apply it to the HERA data. Schildknecht and Spiesberger make a couple of simple assumptions on the form of the energy dependence of the forward scattering amplitude in the GVD formalism and obtain a remarkably good fit to the ZEUS and H1 data even below $Q^2 < 1 \text{ GeV}^2$, as shown in figure 9. Further more accurate measurements at even lower Q^2 can be expected in the future, which should shed further light on this very interesting region at the boundaries of applicability of perturbative QCD.

Returning now to the region which is well described by perturbative QCD, it has been known for many years that conventional DGLAP evolution leads to a strong growth of F_2 as x decreases ⁴⁰. Ball and Forte ⁵⁵ have shown that DGLAP also predicts a “double asymptotic scaling” in the two variables ρ and σ where

$$\sigma = \sqrt{\ln \frac{x_0}{x} \cdot \ln \frac{t}{t_0}} \quad (48)$$

$$\rho = \sqrt{\ln \frac{x_0}{x} \cdot \left(\ln \frac{t}{t_0}\right)^{-1}} \quad (49)$$

$$t = \ln \frac{Q^2}{\Lambda^2} \quad (50)$$

where $x_0 = 0.1$ and $t_0 = \ln(Q_0^2/\Lambda^2)$ with $Q_0^2 = 0.5 \text{ GeV}^2$, are the initial values from which the DGLAP evolution begins and $\Lambda = 185 \text{ MeV}$ is the leading order QCD Λ value appropriate to four active flavours of quark. The observation of this scaling implies that DGLAP evolution is sufficient to explain qualitatively the behaviour of the HERA data; deviations from scaling at large ρ (which is equivalent to small x at fixed small Q^2) might indicate the importance of logarithmic terms not summed in

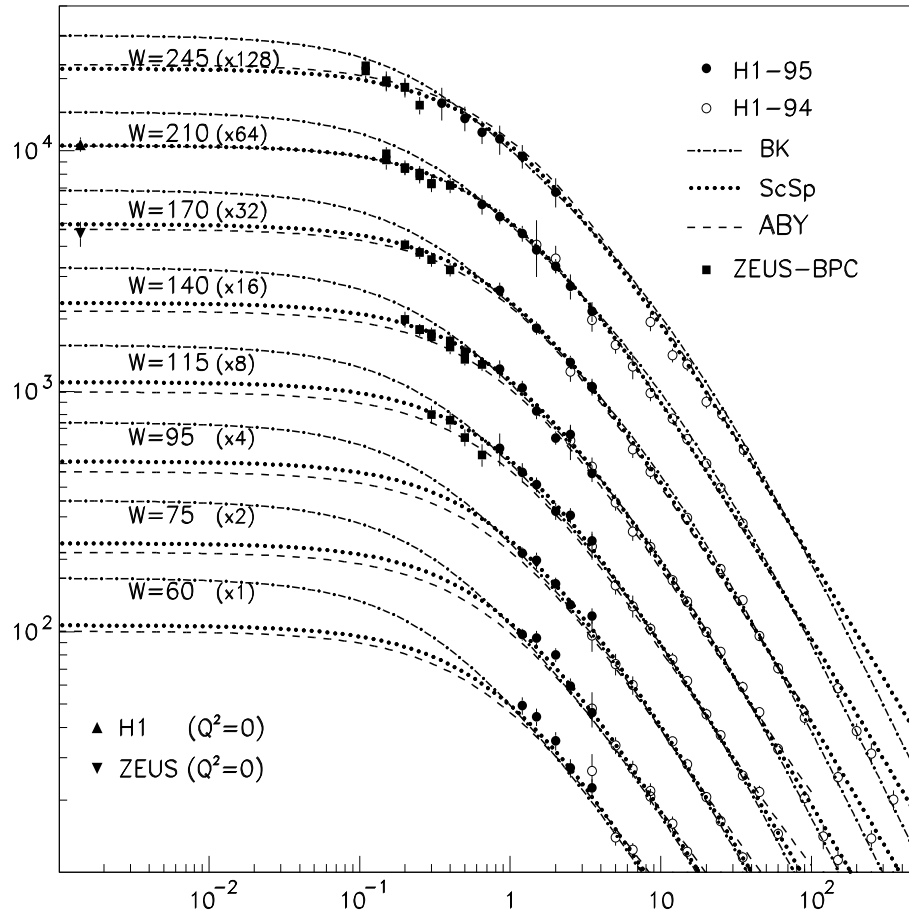


Fig. 9. Values of the total virtual photon-proton cross-section from ZEUS and H1 for various W (in GeV), plotted as a function of $\ln Q^2$. The curves show the GVD fits of Schildknecht and Spiesberger⁵³.

conventional DGLAP evolution e.g. $\ln 1/x$ terms not accompanied by leading $\ln Q^2$ terms, often referred to as ‘‘BFKL behaviour’’, although other explanations are also possible. Figure 10 shows the H1 F_2 values re-scaled by

$$R'_F(\sigma, \rho) = 8.1 \exp\left(\delta \frac{\sigma}{\rho} + \frac{1}{2} \ln \sigma + \ln \frac{\rho}{\gamma}\right) \quad (51)$$

which removes the calculable model independent terms and leads to a linear rise with σ . The upper picture shows F_2 scaled by

$$R_F = R'_F \exp\{-2\gamma\sigma\} \quad (52)$$

In these equations γ and δ are factors unambiguously predicted from NLO QCD. With sufficiently accurate data these can be fit and compared to the QCD expectation. The data do indeed exhibit approximate double asymptotic scaling; any possible deviations at high ρ will require higher accuracy data to be established.

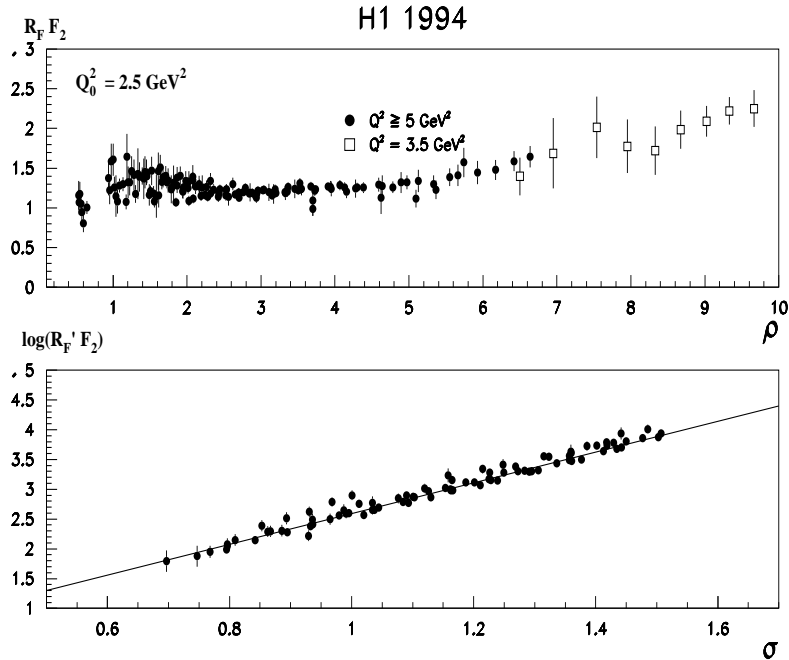


Fig. 10. The F_2 structure function from H1 scaled by R_F and R'_F . The data are binned in two Q^2 bins as a function of ρ . In the plot against σ only those points with $\rho > 1.5$ are plotted.

The approach taken by Ball and Forte is one of several possible ways in which a perturbative QCD ansatz can be approximated to produce tractable formulae in particular kinematic conditions (see also for example ^{56,57,58,59}). Their approach essentially corresponds to following the Altarelli-Parisi evolution and summing terms leading in $\ln Q^2$; another approach (see for instance ⁶⁰) is to follow a BFKL evolution by summing the leading $\ln 1/x$ terms, leading to a power-type behaviour in x of the form $x^{-\lambda_S}$. There have been attempts to unite these two approaches, using for instance the CCFM equation ⁴² (see for instance ⁴³). The work of Thorne ⁶¹,

building on the work of Catani⁶², has demonstrated that a factorisation and renormalisation scheme-independent approach implies the necessity of summing *both* the leading $\ln Q^2$ *and* leading $\ln 1/x$ terms. This scheme gives a good fit to the HERA and fixed target data and also has some limited predictive power on the form of the structure functions at small x .

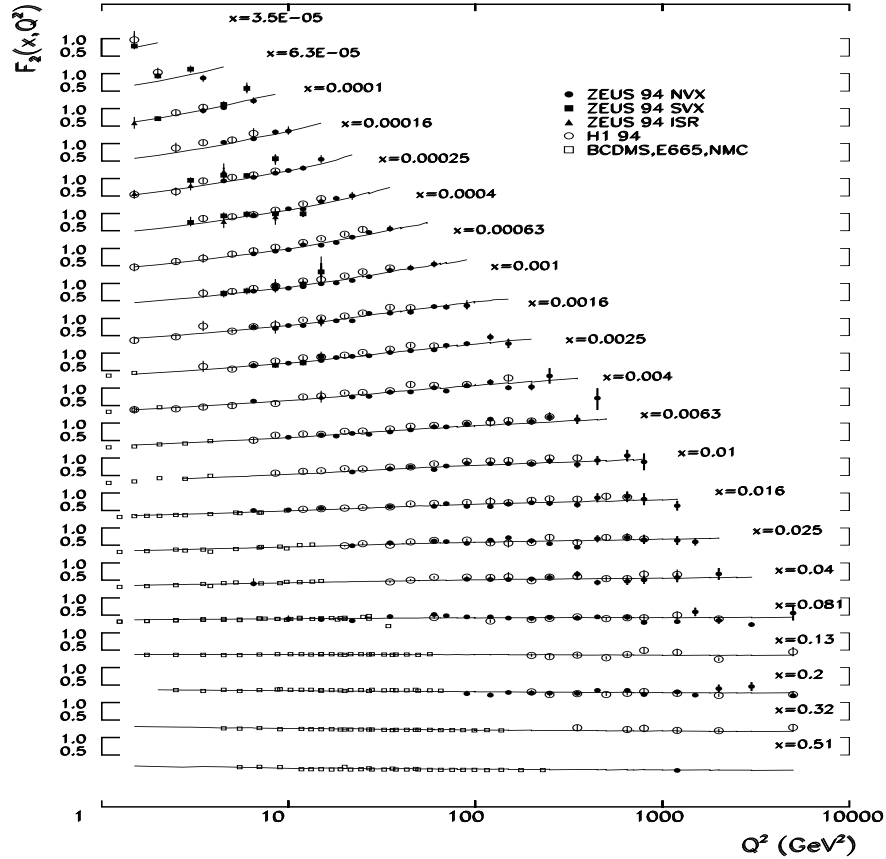


Fig. 11. F_2 from ZEUS, H1,BCDMS³⁰, NMC95³¹ and E665³² in x bins plotted as a function of Q^2 . The curve shows the prediction from a NLO QCD fit to the ZEUS data.

Finally in this section we show in figure 11 the F_2 data from both experiments plotted as a function of Q^2 for different x bins. The data now extend over four orders of magnitude both in x and Q^2 . The pronounced change in slope as x rises is clear evidence for scaling violations and the excellent agreement of the QCD fit with the data shows that these violations are consistent with the expectations of QCD. Since these scaling violations are generated by gluon emission and splitting, fits using a full QCD formalism would be expected to yield information on the gluon density in the proton. This leads us into section 5, in which the determination of the gluon structure function of the proton is discussed. Section 6 discusses the first data on the determination of F_2 for particular quark flavours (i.e. F_2^{charm}), which

is not only a major part of the inclusive F_2 , but also will give us important new information on the gluon density.

In conclusion, it is clear that the results on F_2 from HERA have had a profound effect on our understanding of QCD and have stimulated much theoretical activity. The quality of the data is now such that QCD can be quantitatively tested. However, the difference in F_2 predicted at low x if BFKL behaviour dominates compared to that from DGLAP is rather small. Moreover, there is a great deal of freedom in fitting the steep rise in F_2 in the DGLAP analyses, either in the MRS and CTEQ approaches by varying the steepness of the starting gluon distributions or in the GRV approach by changing slightly the starting Q^2 distribution, Q_0^2 . The H1 collaboration⁶³ have performed QCD fits to their F_2 data in which they have compared pure DGLAP evolution to a mixed DGLAP-BFKL formalism; both ansatzes give equally acceptable fits to the data. Currently the precision of the data is insufficient to distinguish these options.

Our lack of knowledge of F_L will probably dominate the systematic error on F_2 at the higher values of y in the near future. Since F_L is in principle sensitive to properties of QCD which cannot be explored from measurements of F_2 , it is also of intrinsic importance to measure F_L . This measurement is however notoriously difficult, and forms the subject of the next section.

4.3 Measurement of F_L

The DIS differential cross-section given in equation 15 shows that F_L and F_2 have differing contributions depending on the value of y . One method for measuring F_L would therefore be to measure the differential cross-section at fixed Q^2, x but varying y . Since these quantities are related by equation 7, this can only be achieved by changing s .

One obvious way in which s could be changed would be to change either the positron or proton beam energy by an amount large enough to produce a sizeable change in y and therefore to separate out the contributions of F_L and F_2 to the cross-section. Increasing the HERA beam energies is severely limited by technology and cost; unfortunately there are also severe penalties associated with reducing beam energies to the sort of level required to make a reasonable measurement of F_L . These penalties include both a loss of luminosity and increase in systematic errors associated with for example the identification of the scattered electron. For these reasons, although there have been feasibility studies⁶⁴ and the possibility continues to be discussed, the option of reducing the beam energies has not been used at HERA to date.

An alternative possibility is to utilise the unavoidable tendency of the incoming positron to radiate a hard photon. Such hard radiation results in an effective reduction of s . Several studies of utilising such events to measure F_L have indeed been carried out⁶⁵. However, the radiation of hard photons is clearly less likely by a factor α and together with the limitations of phase space on the emitted photon energy the fraction of such radiative events is very small. This fact together with additional systematic effects which also plague such determinations mean that a useful measurement of F_L using radiative events has yet to be achieved.

The H1 collaboration has recently carried out an extraction of F_L which utilises neither of these techniques⁶⁶. Instead they choose the kinematic region which maximises the size of the contribution of F_L to the differential cross-section ($y \rightarrow 1$) and subtract the value of F_2 . The disentanglement of the F_L and F_2 contributions is achieved by using data at low y where F_L has a negligible contribution to the cross-section to determine F_2 , and then evolving this value of F_2 to high y using the NLO Altarelli-Parisi equations. Given that this procedure involves an extrapolation which makes strong assumptions both on the form of the extrapolation and on the value of F_L in a different region of phase space, clearly this method is not as

satisfactory as the two alternative methods mentioned above. It does however have the inestimable advantage of producing a significant determination of F_L .

The region of y selected by H1 for the F_2 measurement was $0.6 < y < 0.78$, divided into six bins of Q^2 between 8.5 and 35 GeV² and x between 1.4 and $5.5 \cdot 10^{-4}$. In order to achieve such large values of y it is necessary to identify very low energy scattered electrons, in this case between 6.5 and 11 GeV. Since high y events also tend to produce current jets in the rear direction, there is significant background from hadronic and photonic energy deposits which mimic a scattered electron. Such factors were evaluated by modifying the normal electron finding strategy, which considered only the highest energy electromagnetic energy deposits in an event, to include also the second highest deposits. A careful estimation of the photoproduction background was also made using “tagged” photoproduction events, which have the scattered electron detected in the luminosity detector, but which otherwise satisfied the selection criteria. The photoproduction background was never larger than 20% and fell to $\sim 5\%$ at the highest values of Q^2 . The systematic errors on the cross-sections in the chosen high y range were between 6 and 8%.

A QCD fit similar to the standard H1 analysis of F_2 was carried out but using only data with $y < 0.35$ and omitting fixed target data from NMC. BCDMS data³⁰ was used to constrain the high x data. The Sigma method (see section 3.4) was used for the low y data, while the electron method was used for the reconstruction of the kinematic variables in the high y region used in the F_L determination. The starting point for the Altarelli-Parisi evolution of the F_2 determined from the low- y data was $Q^2 = 5$ GeV². The values for F_2 thus determined were subtracted from the measured cross-sections to produce the values for F_L shown in figure 12. It can be seen that the extreme values of $F_L = F_2$ and $F_L = 0$ are excluded (at more than two standard deviations). The F_L values are clearly dominated by the systematic error. They agree well with F_L constructed from the parton distributions produced from the QCD fit to F_2 assuming the QCD prediction for F_L (see equation 26).

It is clear that this is an interesting determination of F_L at unprecedentedly low x ; equally clearly, it is dominated by the systematic error and the theoretical assumptions employed. Further progress in the measurement of F_L must come from either greatly increased luminosity (via radiative events) or from a reduction in one or both of the beam energies at HERA.

5 The gluon density inside the proton

Several different methods can be used at HERA to estimate the gluon structure function of the proton. The “classic” way of measuring $G(x)(\equiv xg(x))$ is to measure the scaling violations in F_2 as a function of Q^2 . Other processes can give information, although usually in a rather more model dependent way. The crucial element is that something in the process should provide a hard scale about which a QCD evolution can be anchored. This can either be the Q^2 of the process, a large p_T jet, or a large mass from heavy quark production. The rate of multi-jet events from boson-gluon fusion processes and their kinematic properties allow a reconstruction of the momentum density of the initial gluon. Another source of information is the measurement of vector meson production in deep inelastic scattering. We also mention for completeness two photoproduction processes, J/ψ production and inclusive charm production, which, because of the hard scale given by the charm quark mass, can also be used to determine the gluon density within the proton.

The importance of these methods in determining $g(x)$ is not only the different experimental conditions involved. They also have different sensitivities to the gluon density. In scaling violations $g(x)$ is proportional to the derivative of the measured cross-sections; for jet production and open charm production $g(x)$ is directly pro-

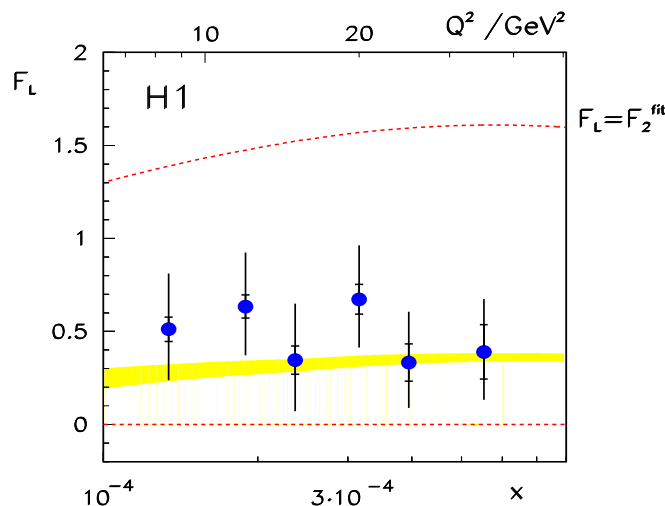


Fig. 12. F_L as a function of x for $\langle y \rangle = 0.7$. The inner error bars correspond to statistical errors, the outer error bars to statistical and systematic errors in quadrature. The shaded band corresponds to the allowed range in F_L from the parton distributions determined from the QCD fit for the low y data evolved according to NLO QCD. The dashed lines correspond to the limits of $F_L = 0$ and $F_L = F_2$.

portional to the measured cross-sections; whereas in vector meson production the cross-section is proportional to $\|g(x)\|^2$. Determinations by all of these methods therefore, while subject to differing degrees of model dependency, give important constraints and cross-checks on the value of the gluon density over a wide kinematic range.

It is important to note that the gluon distribution is not uniquely defined in NLO QCD (see section 3.3). Both ZEUS and H1 use the \overline{MS} scheme¹⁸ in their determinations.

5.1 $G(x)$ from scaling violations in F_2

The ZEUS and H1 data presented in figure 11 show qualitatively the behaviour to be expected from QCD, i.e. a growth in the sea quark density at lower x which increases as Q^2 increases. It is therefore instructive to make a quantitative comparison with QCD via a full QCD fit to next-to-leading order. As we have already discussed, this has also been done by a number of groups, who make global fits to all available data in order to produce the “best-fit” parton distributions. The approach of the HERA experiments is somewhat different, in that they use the minimum amount of extra data necessary to produce a reasonably constrained fit, particularly at high x , which is kinematically difficult to access at HERA, and are able to make full use of their knowledge of the correlations between the experimental errors^{28,67}.

Equation 54 shows the functional forms at an initial Q^2 value of $Q_0^2 = 4 \text{ GeV}^2$ used by the H1 collaboration in their QCD fit on their 1993 data.

$$\begin{aligned} xg(x) &= A_g x^{B_g} (1-x)^{C_g} \\ xq_{NS}(x) &= A_{NS} x^{B_{NS}} (1-x)^{C_{NS}} (1 + D_{NS}x) \end{aligned} \quad (53)$$

$$xq_{SI}(x) = A_{SI}x^{B_{SI}}(1-x)^{C_{SI}}(1+D_{SI}x)$$

The singlet quark density is defined as $q_{SI} = u + \bar{u} + d + \bar{d} + s + \bar{s}$. The non-singlet quark density is given by $q_{NS} = u + \bar{u} - q_{SI}/3$. ZEUS used a rather different form, as shown in equation 5.1.

$$\begin{aligned} xg(x) &= A_g x^{B_g} (1-x)^{C_g} \\ xq_{NS}(x) &= A_{NS} x^{B_{NS}} (1-x)^{C_{NS}} \\ xq_{SI}(x) &= A_{SI} x^{B_{SI}} (1-x)^{C_{SI}} (1 + D_{SI}x + E_{SI}\sqrt{x}) \end{aligned} \quad (54)$$

It is important to impose a constraint on the momentum fraction carried by the gluon at low Q^2 , which in the H1 case was set at 0.44⁶⁸ at $Q_0^2 = 4 \text{ GeV}^2$, the point from which their evolution begins. The momentum sum rule then gives the normalisation of the singlet quark density. ZEUS preferred to input the valence quark distribution directly from the MRSD-' parameterisation, assuming that the strange quark distribution is 20% of the quark sea and using $Q_0^2 = 7 \text{ GeV}^2$. Only the three light quarks are involved in the DGLAP evolution. The effect of the charm quark was included via the photon-gluon fusion process as discussed in^{69,70}; ZEUS used the leading-order calculation for this effect for the analysis of the 1993 data, while H1 used the next-to-leading order according to⁷¹. At the Q^2 of interest here, the effects of the b quark can be neglected. However, it is important⁷² to ensure that $\alpha_s(Q^2)$ remains continuous across the c and b thresholds. Since diffractive events (see section 8) presumably occurred in fixed target experiments but were not separated out, diffractive events were also retained in these analyses.

Since the whole basis of the DGLAP equations is a strong link between gluon and sea, with the sea quark distributions being driven by the gluon distribution at small x , it has been conventional until recently to assume that these distributions have identical x behaviour. However, the quality of the HERA data, particularly when taken in conjunction with other experimental data, is now sufficiently good to indicate a preference that these distributions should be decoupled⁷³. ZEUS and H1 have therefore performed fits in which the x dependence of the sea and gluon is allowed to be different.

Figure 13 shows the results of the full QCD analysis from the 1993 ZEUS data⁶⁷. The Prytz method⁷⁴ uses a Taylor expansion about $x/2$, ignoring the contribution from the quarks in the DGLAP evolution equation, to give the approximate result at leading order

$$xg(x, Q^2) = \frac{\partial F_2(x/2, Q^2)}{\partial \log(Q^2)} \left[\frac{40}{27} \frac{\alpha_s(Q^2)}{4\pi} \right]^{-1} \quad (55)$$

which at next-to-leading order becomes

$$\begin{aligned} xg(x, Q^2) &= \frac{\partial F_2(x/2, Q^2)}{\partial \log(Q^2)} \left[\left(\frac{40}{27} + 7.96 \frac{\alpha_s}{4\pi} \right) \frac{\alpha_s(Q^2)}{4\pi} \right]^{-1} \\ &\quad - \frac{5\alpha_s}{9\pi} N(x/2, Q^2) \left[\frac{40}{27} + 7.96 \frac{\alpha_s}{4\pi} \right]^{-1} \end{aligned} \quad (56)$$

where $N(x/2, Q^2)$ is a correction function which depends on the already measured gluon density at high x . The EKL⁵⁷ method assumes a particular functional form for $g(x)$ and includes both the gluon and singlet quark contribution to the DGLAP evolution.

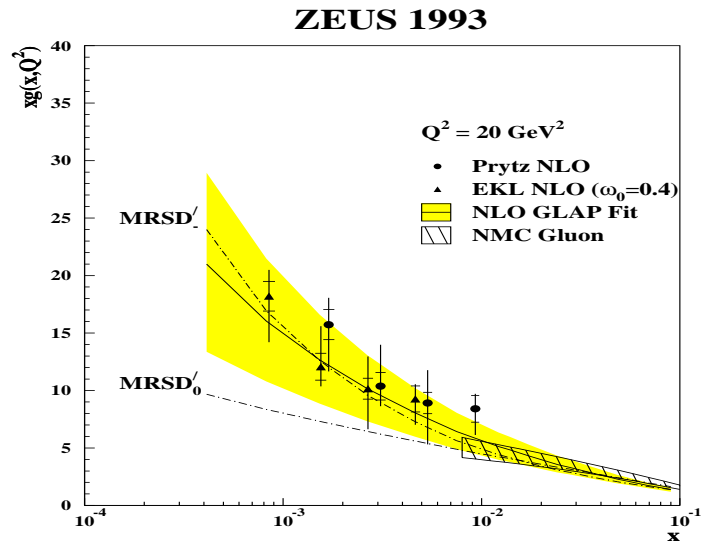


Fig. 13. $xg(x)$ as a function of x as determined from scaling violations in the 1993 ZEUS F_2 data. Two approximate determinations from Prytz and Ellis, Kunszt and Levin are shown. The angled shaded region shows a determination at higher x from the NMC experiment. The shaded region shows the full QCD fit to the ZEUS 1993 data. Also shown as dashed-dotted lines are the $MRSD'_0$ and $MRSD'_J$ parameterisations of $G(x)$ ⁴⁴. Also shown are two methods using approximations to the QCD evolution equations to extract $G(x)$ in bins of x , due to Prytz ⁷⁴, and Ellis, Kunszt and Levin ⁵⁷.

Figure 13 shows that these approximate methods are consistent with the full ZEUS QCD fit, which in turn matches well to a determination of $G(x)$ by NMC⁶⁸. H1 have also compared the leading order Prytz approximation with their full QCD fit and find good agreement.

Figure 14 shows the results of the QCD analyses of both experiments for the 1993 data. They are in very good agreement, and map on well to the NMC gluon determination at $x > 10^{-2}$.

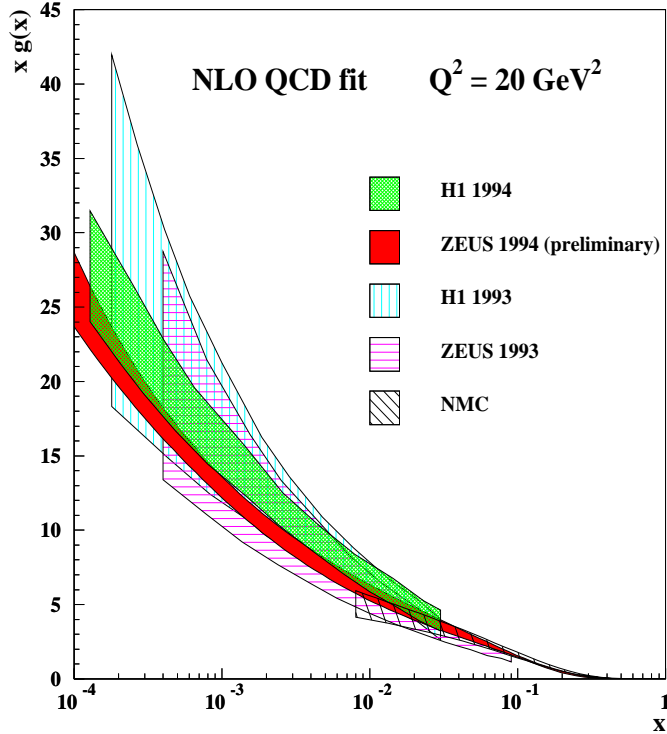


Fig. 14. The gluon density $xg(x)$ as determined by the H1 and ZEUS collaborations using NLO QCD fits to both the 1993 F_2 data and the 1994 data, together with the determination at higher x from NMC⁶⁸.

The shaded areas in Figure 14 show the allowed regions of the full NLO QCD fits in which the statistical and systematic errors, and the point-to-point correlations between them, are taken properly into account. A comprehensive list of the systematic effects studied can be found in the relevant experimental publications^{63,67}. Whereas in principle the value of α_s can be determined from the fit, in practice the scaling violation data is relatively insensitive to it. However, Ball and Forte have described a procedure in the double scaling regime which is sensitive to α_s using a fit of truncated parton distributions from global analyses to the HERA data at low x ⁷⁵. As the HERA data become more accurate, this may well become an important technique. Nevertheless, the attitude of the experiments until now has been to estimate the systematic error by redoing the fits using the limits of error values of α_s . It transpires that the resultant additional systematic error is negligible at low x .

The greatly increased statistics in the 1994 data allow a significant reduction in the error of the gluon determination. H1²⁸ have modified their 1993 fitting procedure to parameterise the parton distributions at $Q^2 = 5 \text{ GeV}^2$ and to allow the non-singlet distributions to be split into separate u and d quark distributions, viz.

$$\begin{aligned}
 xg(x) &= A_g x^{B_g} (1-x)^{C_g} \\
 xu_v(x) &= A_u x^{B_u} (1-x)^{C_u} (1 + D_u x + E_u \sqrt{x}) \\
 xd_v(x) &= A_d x^{B_d} (1-x)^{C_d} (1 + D_d x + E_d \sqrt{x}) \\
 xS(x) &= A_S x^{B_S} (1-x)^{C_S} (1 + D_S x + E_S \sqrt{x})
 \end{aligned} \tag{57}$$

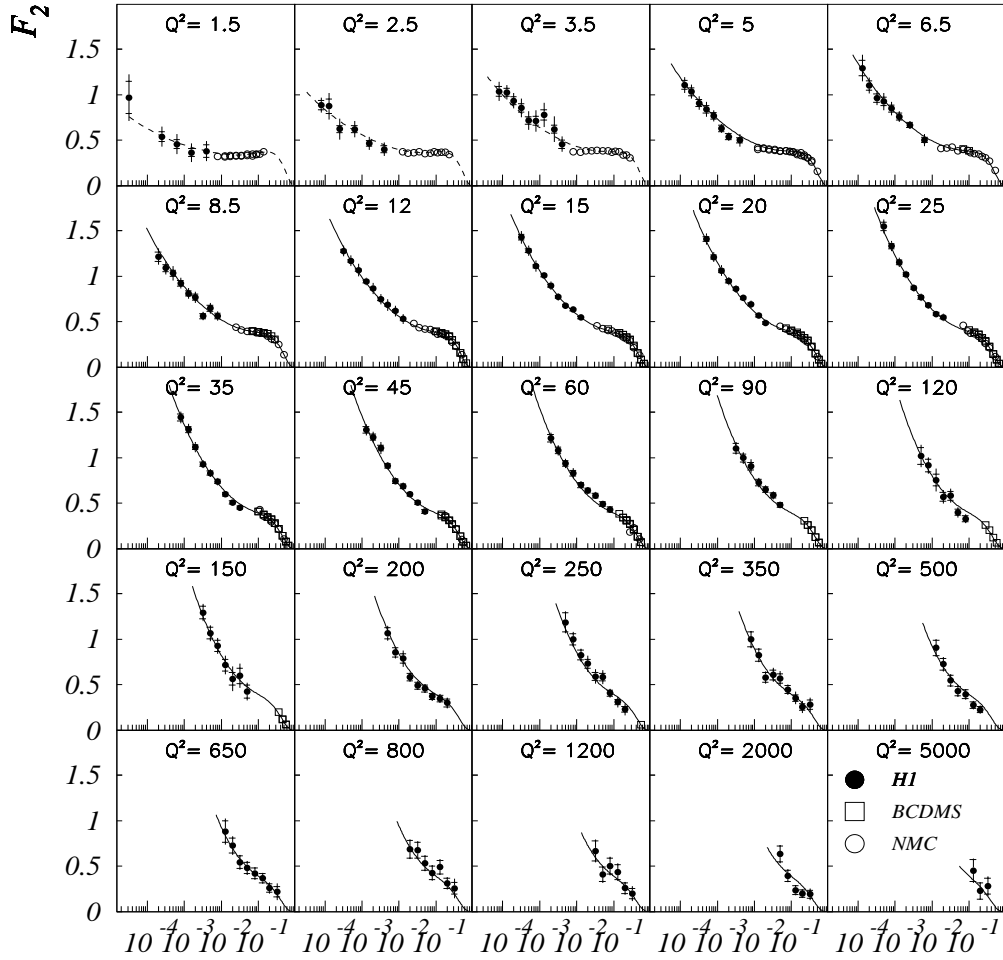
In order to constrain the valence quark densities at high x , it is necessary to include some fixed target data from BCDMS³⁰ and NMC⁶⁸. The H1 F_2 data were fit for $Q^2 > 5 \text{ GeV}^2$. The relative normalisation of these data sets and the H1 normal and shifted vertex data were allowed to vary within the quoted errors; no data set requires a normalisation change of more than $\pm 4\%$. The overall χ^2 for the fit was acceptable. The result of the fit in Q^2 bins as a function of x is shown in figure 15. The quality of the fit and the change of slope as a function of Q^2 can clearly be seen.

ZEUS have carried out a similar fit to their 1994 data, but this analysis is as yet still preliminary. Figure 14 shows the result of the gluon determination from the 1994 data from both experiments as a function of x , as well as the 1993 determinations. The 1994 data are in good agreement with the 1993 determinations and both experiments show a steep rise as x falls. While the two experiments are compatible, the 1994 H1 result does seem to be somewhat steeper than that of ZEUS. The GRV parameterisation has problems in fitting the relatively shallow ZEUS data and maintaining a good fit at higher x ; the higher precision 1995 and 1996 data, which are now starting to be analysed, may well be able to rule out some of the *ansätze* currently in use.

In conclusion, the measurement of the gluon distribution via a NLO QCD analysis of scaling violations in F_2 has extended our knowledge of $G(x)$ by almost two orders of magnitude in x . Scaling violations, while a relatively insensitive technique for measuring $G(x)$, remain the least model dependent method available.

5.2 $G(x)$ from jet rates in DIS

In the previous section we discussed the measurement of the gluon distribution by means of a fully inclusive DIS measurement, the scaling violations in F_2 as a function of Q^2 . It is possible by studying more exclusive processes to obtain greater sensitivity to the gluon distribution, although usually at the price of greater model dependence. One such method is to study jet production in a region of phase space where gluon-induced reactions can be cleanly isolated. Figure 16 shows the process of boson-gluon fusion, which is clearly sensitive at the Born level to the gluon density in the proton. Since each of the quarks at high enough Q^2 will give rise to a jet, such a reaction can be isolated in a sample of “2+1” jet events, where the proton remnant jet referred to as the “+1” is predominantly lost in the beam pipe. Unfortunately, similar processes initiated by a quark from the proton rather than a gluon and where the second visible jet originates from hard gluon radiation, known as the “QCD Compton” process, also populates this sample. To leading order, the total rate of “2+1” jets is proportional to the sum of these two processes, $\alpha_s(A \cdot g + B \cdot q)$, where g and q refer to the gluon and quark densities in the proton respectively and A and B can be calculated in perturbative QCD. Clearly it is possible in principle to measure α_s , g and q from the “2+1” jet events.



x

Fig. 15. The H1 F_2 data as a function of x in bins of Q^2 . The inner error bar is statistical, while the full error bar represents statistical and systematic errors added in quadrature. The overall scale uncertainty due to the luminosity is not included. The full curves represent the result of the QCD fit described in the text. The dotted lines represent the result of that fit evolved to lower Q^2 according to the QCD prescription.

However in practice it has until now been necessary to either assume α_s from other measurements and measure parton distributions or *vice-versa*. The latter procedure is discussed in section 7.3. In this section we assume that α_s can be fixed from other processes and concentrate on the determination of $g(x)$.

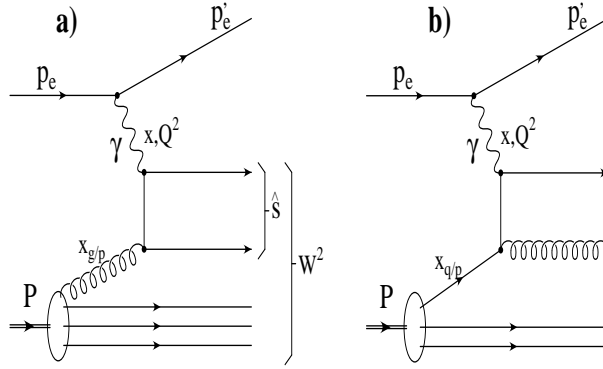


Fig. 16. Feynman diagrams appropriate to “2+1” jet production in DIS. The first, a), shows the boson-gluon fusion process; b) shows the QCD Compton process. Note that hard gluon radiation from the struck quark after it has absorbed the virtual photon is also a QCD Compton process, but it not shown here.

In the processes illustrated in figure 16, the x of the parton from the proton ($x_{i/p}$) is not identical with the “Bjorken- x ” seen by the virtual photon. Indeed

$$x_{i/p} = \frac{\hat{s} + Q^2}{ys} = x \left(1 + \frac{\hat{s}}{Q^2} \right) \quad (58)$$

The hard sub-process energy squared, \hat{s} , can be measured either directly from the invariant mass of all particles p_j of the two jets belonging to the hard sub-system

$$\hat{s} = \left(\sum_j p_j \right)^2 \quad (59)$$

or from the jet directions in the hadronic centre-of-mass system

$$\hat{s} = W^2 e^{-(\eta_1^* + \eta_2^*)} \quad (60)$$

where η_1^* and η_2^* are the pseudo-rapidities ($\eta = -\ln(\tan \theta/2)$) of the partons taking part in the hard sub-process.

The struck partons in both the BGF and QCD Compton processes emerge into the detector as jets of particles whose reconstructed energies and directions approximate to those of the partons. The ability of the analysis to discriminate on kinematic grounds between the BGF and QCD Compton processes is therefore crucially dependent on the quality of the jet measurement.

The event selection in the H1 analysis⁷⁷ is based on the identification of exactly two jets via the cone algorithm with $\Delta R = \sqrt{\Delta\eta^2 + \Delta\phi^2} = 1$ and $p_{T^*} > 3.5$ GeV. A series of kinematic cuts is made designed to enhance the proportion of “2+1” jet events emanating from the BGF process and to improve the jet finding efficiency.

In order to improve the resolution on \hat{s} and hence on $x_{g/p}$, both equations 59 and 60 are evaluated and only those events with $|\Delta\sqrt{\hat{s}}| \leq 10$ GeV, where $\Delta\sqrt{\hat{s}}$ is the difference between $\sqrt{\hat{s}}$ found from the two reconstruction methods, are retained in the analysis. This requirement removes about 20% of candidates, and not only suppresses tails in the resolution but also discriminates against contamination from “1+1” jet events, where the two methods in general produce different answers. The sample produced in this way consists of 328 “2+1” jet events.

Good agreement is observed between the data and Monte Carlo predictions using the LEPTO 6.1 generator, which is used both to estimate the acceptance for the BGF process and also to calculate the background from quark initiated contributions such as the QCD Compton process. The cross-section can be parameterised as

$$\begin{aligned} \sigma_{obs.}^{2+1}(x_{i/p}^{rec}) &= \int M(x_{g/p}, x_{g/p}^{rec}) x_{g/p} g(x_{g/p}) dx_{g/p} \\ &+ \sigma_{MC}^{QCD-C}(x_{q/p}^{rec}) + \sigma_{MC}^{QPM}(x_{q/p}^{rec}) \end{aligned} \quad (61)$$

After subtraction of the backgrounds from QCD Compton processes (σ_{MC}^{QCD-C}), and from “1+1” jet events faking “2+1” jet events (σ_{MC}^{QPM}), the gluon distribution may be deduced by de-convoluting with the function M , which contains the QCD matrix element and the effects of hadronisation. After unfolding in five bins the results shown in figure 17 are obtained.

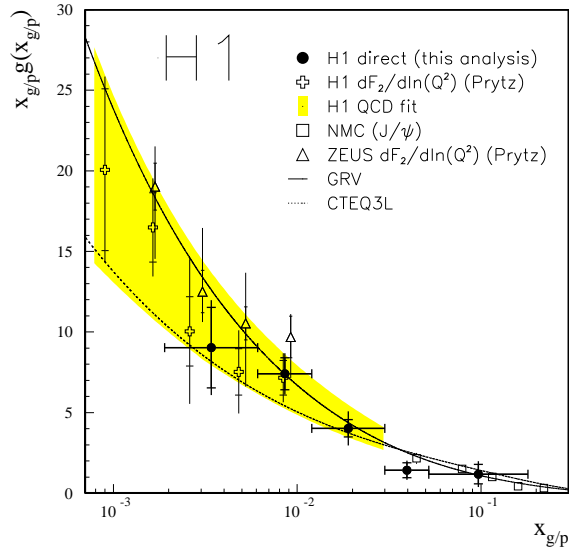


Fig. 17. The measured gluon density at $\langle Q^2 \rangle \sim 30$ GeV² as a function of the fractional gluon momentum as determined in the H1 “2+1” jet analysis. Also shown are the determinations by H1 and ZEUS referred to in section 5.1 at $Q^2 = 20$ GeV² as well as a determination from J/Ψ production by NMC ⁷⁶ evolved to $Q^2 = 30$ GeV²

The unfolding procedure produces a full covariance matrix of the statistical errors. The systematic error in each bin is obtained from reasonable variation in the

assumptions used in the analysis. The largest systematic effects are the uncertainty in the absolute hadronic energy scale in the H1 Liquid Argon calorimetry at low x and the variation in the cut on $|\Delta\sqrt{\hat{s}}|$ at high x . The error on the BGF and QCD Compton acceptance was estimated by using different models in the Monte Carlo, e.g. HERWIG. Figure 17 shows good agreement between this analysis and other methods from H1, ZEUS and NMC. The data from this analysis lies in an x region between those from other methods at HERA and NMC ⁷⁶. It demonstrates the consistency over the full x_g range and also exhibits a strong rise in the gluon density as x_g falls.

Subsequent to this analysis, which uses leading order matrix elements, Mirkes and Zeppenfeld ⁷⁸ derived the next to leading order corrections. The main effect of these corrections is to reduce the dependence on the renormalisation and factorisation scale. Although the effect on the \hat{s} and x distributions is quite large, the effect on the final parton distribution functions is relatively small due to cancellations. However, the unfolding of the gluon density becomes significantly more complicated.

5.3 Light vector meson production

In DIS, the hard scale in the production of light vector mesons such as the ρ and ϕ is fixed by the Q^2 of the deep inelastic process. The link between this phenomenon and the gluon density in the proton is found in many perturbative QCD models of the production mechanism ^{79,80}. Such models consider the reaction to proceed in leading order via the colour singlet exchange of two gluons. For example, in the model of Brodsky *et al.* ⁸⁰ the cross-sections of vector mesons produced by longitudinally polarised photons are proportional to the square of the gluon density in the proton:

$$\frac{d\sigma_L}{dt} \Big|_{t=0} (\gamma^* N \rightarrow V^0 N) = \frac{A}{Q^6} \alpha_s^2(Q^2) \cdot \left| \left[1 + i\frac{\pi}{2} \left(\frac{d}{d \ln x} \right) \right] xg(x, Q^2) \right|^2 \quad (62)$$

where A is a constant predicted by the model. In principle this quadratic dependence increases the sensitivity to the gluon density compared to methods such as those described earlier, which are related to single gluon processes. However, the extraction of the gluon distribution from vector meson data using these methods is only correct to leading order and furthermore relies on explicit theoretical assumptions which currently cannot be unambiguously established by the data.

Deep inelastic vector meson production has a very distinctive and clean signature at HERA. This means that the data selection is straight-forward. Two charged tracks consistent with being hadrons and a scattered positron indicative of deep inelastic scattering are required. Kinematic cuts are used to reduce the photoproduction background caused by the mis-identification of energy deposits in the calorimeter as a scattered positron. Both H1 and ZEUS see clear signals for ρ^0 production. The signal obtained by H1 is shown in figure 18, where a clear ρ signal with the expected mass and width is observed with very little background. Figure 19a shows the total elastic ρ cross-section as a function of W as measured by ZEUS ⁸¹ and H1 ⁸² in two bins of Q^2 . NMC ⁸⁴ points at lower W are also shown. The ZEUS data seem substantially higher than those of H1, although the quoted overall normalisation uncertainties of 31% for ZEUS and 7% for H1 mean that the discrepancy is not significant. The slope of the H1 cross-section as a function of W seems to lie between the “soft” value which fits the ρ photoproduction data ⁸³, and the “hard” value appropriate to QCD-type models ⁸⁰, whereas that of ZEUS is

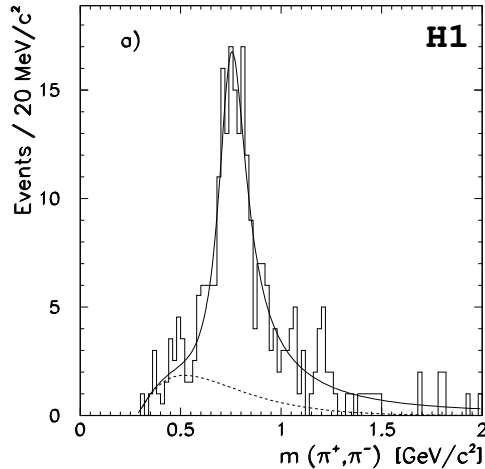


Fig. 18. The $\pi^+\pi^-$ invariant mass distribution for ρ candidates in deep inelastic scattering for $7 < Q^2 < 25 \text{ GeV}^2$ and $40 < W < 130 \text{ GeV}$.

compatible with the “hard” expectation. Only ZEUS therefore has used the ρ data to extract a gluon distribution.

The γ^*p cross-section for ρ production from ZEUS is shown in figure 20 as a function of x in the two measured Q^2 bins. The ZEUS measurement for the gluon distribution from the F_2 scaling violations can be used within the framework of the model of Brodsky *et al.* to obtain a prediction for ρ production which is also shown in figure 20. The ρ data is consistent with this prediction.

5.4 Heavy quark processes in DIS and photoproduction

There are two particular processes of interest in heavy quark production. The first is the production of vector mesons containing heavy quarks, in particular J/ψ production. In some models the elastic process proceeds via a two gluon exchange mechanism very similar to that described above in deep inelastic ρ production⁷⁹. Inelastic J/ψ production can result from photon-gluon fusion followed by the emission of a second gluon from one of the heavy quark lines. Although produced dominantly at $Q^2 \sim 0$, deep inelastic J/ψ production has also been observed. The second class of processes consists of inclusive production of charmed particles, typically observed either via detecting D^* mesons or high- p_T leptons and also seen in both photoproduction and deep inelastic regimes. Here the dominant production mechanism is photon-gluon fusion. In the case of photoproduction, the hard scale provided by the charm quark mass allows QCD to be used to interpret the measured cross-section in terms of a gluon density.

5.4.1 Elastic J/ψ photoproduction

One particularly clean channel is elastic J/ψ production. Pairs of oppositely charged leptons, either with well reconstructed charged tracks matching energy deposits in the calorimeter consistent with e^+ or e^- , or with charged tracks pointing to hits

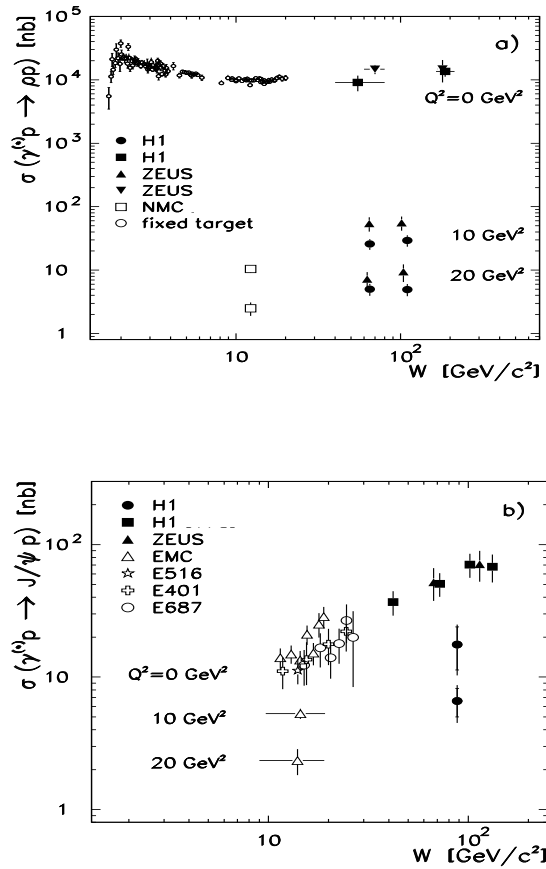


Fig. 19. W dependence of the elastic DIS vector meson cross-section in fixed target and HERA experiments a) for ρ production (computed for $m_{\pi^+\pi^-} < 1.5$ GeV) and b) for J/ψ production (see section 5.4). For the ρ data, an overall normalisation uncertainty of 31% for ZEUS and 20% for NMC is not included in the plot.

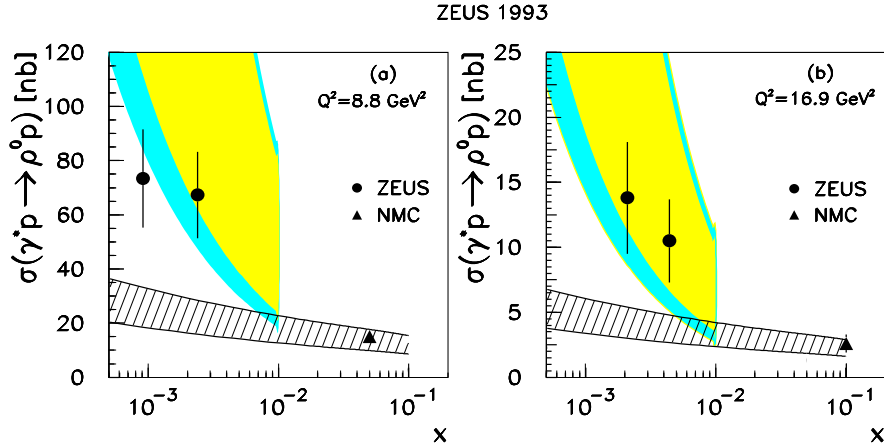


Fig. 20. a) $\sigma(\gamma^*p \rightarrow \rho^0 p)$, as a function of x at $Q^2 = 8.8 \text{ GeV}^2$. The errors shown include both statistical and systematic uncertainties added in quadrature. Also shown is the NMC result ⁸⁴. The dashed curve is a prediction from ⁸³. The hatched area corresponds to the predictions of Brodsky *et al.* ⁸⁰ for $x < 0.01$, where the upper and lower limits are obtained from the limits on $xg(x)$ from ⁶⁷. b) a similar plot for data at $Q^2 = 16.9 \text{ GeV}^2$.

in the muon chambers consistent with μ^+ or μ^- , are selected from events with no other activity in the detectors. The effective mass of the leptons shows a clear peak at the J/ψ mass with very little background.

The total γ^*p cross-section obtained from these signals can be plotted as a function of W . ZEUS data from 1993 have been published ⁸⁶ which, in conjunction with data from fixed target experiments, showed that the J/ψ cross-section was rising quickly with W , much faster than would be predicted from models based on vector meson dominance or Regge theory. These data, together with results from H1 based on the 1994 running, confirm this from HERA data alone. Figure 21 shows the H1 and ZEUS γ^*p cross-sections plotted as a function of W together with fixed target data from Fermilab. The HERA data lie substantially above the prediction from the “soft” Donnachie-Landshoff model ⁸⁷. A fit to all the data gives a slope with W of 0.90 ± 0.06 , to be compared with the Donnachie-Landshoff prediction of 0.32 for $t = 0$. A similar conclusion is drawn from the analysis of the ZEUS 1994 data ⁸⁸. Figure 21 shows the results of calculations using a two gluon exchange model, the Ryskin model ⁷⁹, with two different forms for the gluon. There is clearly some discrimination between different gluon distributions, with the steeper gluon from GRV being disfavoured.

5.4.2 Inelastic J/ψ photoproduction

Inelastic J/ψ production is thought to proceed by photon-gluon fusion followed by the emission of either a hard gluon or several soft gluons. The former is a colour-singlet process whereas the latter is a colour-octet. An inelastic J/ψ sample can be obtained by a similar selection on lepton pairs as in the elastic case but requiring additional tracks to emanate from the interaction point. In practice the greater

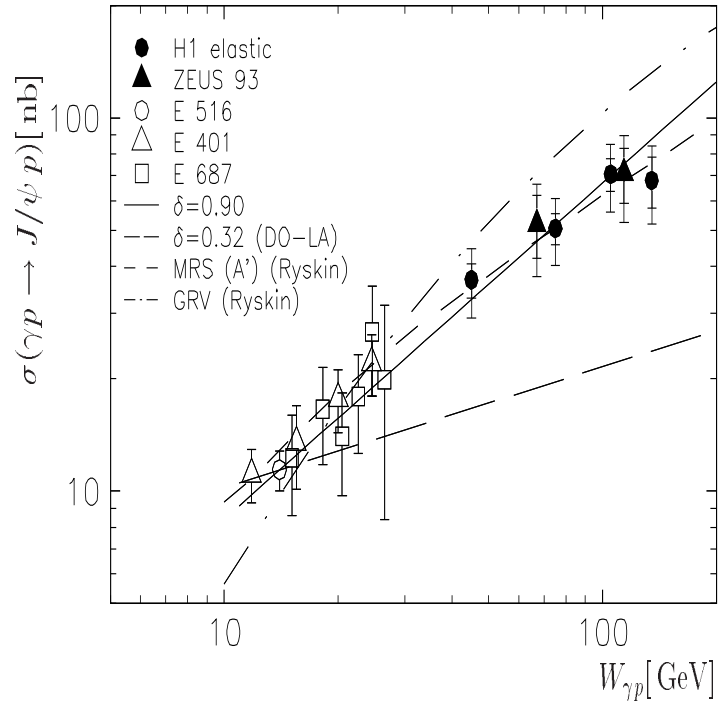


Fig. 21. The J/ψ cross-section as a function of W . The inner error bars on the HERA data points are statistical, the outer error bars show the systematic and statistical errors added in quadrature. The fixed target data points^{89,90,91} have been where necessary scaled with the most recent J/ψ branching ratio; the error bars correspond to both statistical and systematic errors added in quadrature. The full and long-dashed curves obey W^δ with $\delta = 0.90$ and 0.32 respectively. The other curves show calculations from the Ryskin model⁷⁹ with differing parameterisations of the gluon.

activity present in inelastic events makes electron identification more difficult so that muons pairs are normally used. Both H1⁸⁵ and ZEUS⁹² have presented clear inelastic signals with small backgrounds.

The inelastic sample can be clearly distinguished from the elastic sample by cutting on the elasticity variable z as defined by

$$z = \frac{y_{\psi}}{y} \quad \text{with} \quad y_{\psi} = \frac{(E - p_z)_{J/\psi}}{2E_e}. \quad (63)$$

For elastic events $y_{\psi} = y$ and thus $z = 1$. The inelastic sample is defined between $0.45 \leq z \leq 0.90$. The shape of the cross-section variation with W is relatively insensitive to different parton distributions. However, the absolute normalisation of the cross-section does show a significant dependence on parton distribution sets, and the variation of the cross-section as a function of z is sensitive to the importance of colour singlet or octet production mechanisms.

Figure 22 shows the inelastic cross-section as a function of W . In addition to the ZEUS and H1 points, fixed target data from the FTPS⁸⁹, NA14⁹³, and EMC⁹⁴ collaborations is shown. There is clear discrimination between models, depending on the assumed values of m_c and Λ_{QCD} , which implies that future data may well be able to give information on the gluon distribution in the proton.

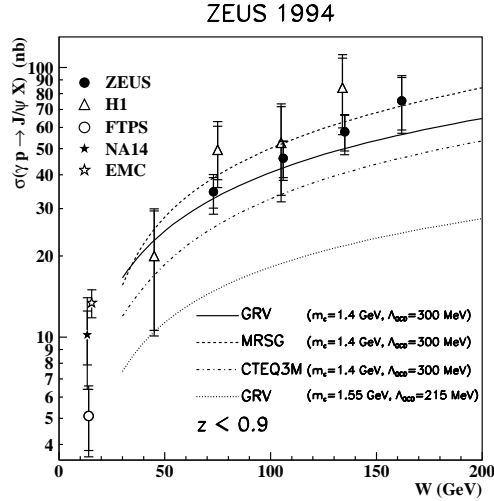


Fig. 22. The direct inelastic J/ψ photoproduction cross section as a function of W for $z < 0.9$. Data from ZEUS, H1, FTPS⁸⁹, NA14⁹³ and EMC⁹⁴ are shown. The ZEUS result at the lowest W value is obtained with the muon channel only, whereas the other ZEUS measurements come from the combination of the electron and muon results. Except for the latter three points, the inner error bars indicate the statistical uncertainty, the outer error bars the quadratic sum of the statistical and systematic uncertainties. For the high W ZEUS points, the inner error bars represent the statistical and decay channel specific errors added in quadrature, the outer ones the statistical, decay specific and common systematic errors added in quadrature. The lines correspond to the NLO prediction from⁹⁷ assuming the GRV²⁶ (continuous), MRSG⁷³ (dashed) and CTEQ3M⁴⁵ (dotted-dashed) gluon distributions with $m_c = 1.4$ GeV and $\Lambda_{QCD} = 300$ MeV, the dotted curve was obtained with GRV, $m_c = 1.55$ GeV and $\Lambda_{QCD} = 215$ MeV. The curves are scaled up by a factor of 1.15 to take into account the contribution from $\psi' \rightarrow J/\psi X$.

Figure 23 shows the cross-section as a function of z as measured by ZEUS and H1. The solid line shows the expectation from a colour singlet exchange model and agrees well with the data. The colour octet model is strongly peaked towards $z = 1$ and thus the octet contribution allowed by this data is very small. The dashed line shows the expectation⁹⁵ if the octet normalisation were fixed to explain the excess production seen in the CDF data⁹⁶. It is clearly ruled out by the HERA data.

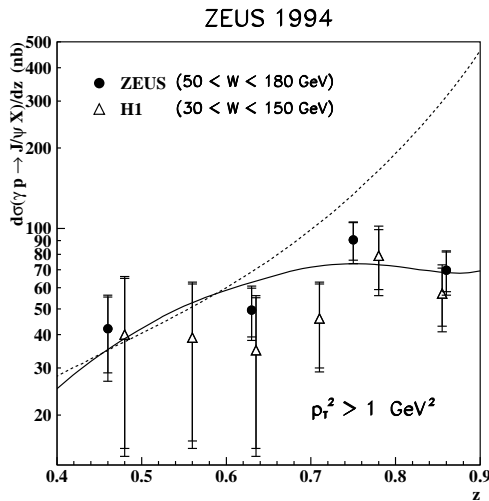


Fig. 23. Differential cross section $d\sigma/dz$ for the inelastic $J/\psi \rightarrow \mu^+\mu^-$ sample with $50 < W < 180 \text{ GeV}$ and $p_T^2 > 1 \text{ GeV}^2$. Data from ZEUS and H1 are shown. The inner error bars indicate the statistical uncertainties, the outer error bars the quadratic sum of the statistical and systematic uncertainties. The NLO computation⁹⁷ with the GRV²⁶ structure function, $m_c = 1.4 \text{ GeV}$ and $\Lambda_{QCD} = 300 \text{ MeV}$ is shown as a solid line. The dashed line is given by the sum of the colour-singlet and the colour-octet leading order calculations⁹⁵. In the theoretical curves the 15% contribution of the ψ' has not been included.

5.4.3 Elastic J/ψ production in Deep Inelastic Scattering

Elastic J/ψ production has been observed at both H1⁸² and ZEUS⁸⁶ at Q^2 up to 40 GeV^2 . The selection criteria are similar to those for the elastic J/ψ in photoproduction discussed in section 5.4.1, with the additional requirement of a well-identified scattered positron.

In contrast to the behaviour observed in ρ production, the J/ψ cross-section seems to show a steep rise as a function of W for all values of Q^2 including $Q^2 = 0$. This implies that the hard scale provided by the charm quark mass is already sufficient to allow the QCD “hard pomeron”-like behaviour to be observed in photoproduction. Figure 19 shows the value of the total virtual photon-proton cross-section for ρ and J/ψ as a function of W for different Q^2 bins. Despite the fact that at $Q^2 = 0$ and low W , J/ψ production is suppressed by a factor of almost 1000, at $Q^2 \sim 20 \text{ GeV}^2$ the J/ψ and ρ cross-sections are almost equal. In fact, H1 obtain⁸² $\sigma(J/\psi)/\sigma(\rho) = 0.64 \pm 0.13$ for $Q^2 = 10 \text{ GeV}^2$ and 1.3 ± 0.5 for $Q^2 = 20 \text{ GeV}^2$. This implies that, as expected in both soft and hard models of vector meson

production, approximate $SU(4)$ symmetry is restored for $Q^2 \gg m_V^2$. The fact that the $J/\psi : \rho$ ratio is so high at Q^2 as low as $\sim 10 \text{ GeV}^2$ is perhaps surprising and is not expected in some QCD models which take into account the effects of quark Fermi motion within the light-cone wave function of the J/ψ ⁹⁸.

5.4.4 Production of open charm

Finally in this section we discuss the use of heavy quark resonances other than vector mesons to determine the gluon distribution. The dominant mechanism for production of charm-anticharm quark pairs at HERA is photon-gluon fusion. In deep inelastic scattering, a gluon from the proton can split into a $c\bar{c}$ pair which interacts directly with the virtual photon. This process is also important in photoproduction, as is the additional process in which a constituent of the photon interacts with the heavy quark or antiquark in a so-called “resolved photon” interaction. In either case the cross-section for charm production depends on the probability of finding a gluon in the proton and therefore measurement of these cross-sections in principle allows an unfolding of $G(x)$.

Two distinct methods which isolate charm production have been used. The first uses the kinematic characteristics of heavy quark decay to enhance the charm signal. A particularly useful method ⁹⁹ uses the decay $D^* \rightarrow D\pi_{slow}$, where the slow pion, π_{slow} , is restricted to a very small area of phase space just above threshold. Several different D decay modes have been used by ZEUS and H1. For the mode $D^0 \rightarrow K\pi$ a clear signal is produced by a cut on the mass difference between the $K\pi\pi$ and $K\pi$ combinations. Particle identification, for example by energy loss in drift chamber gas, has been used to help in the identification of charmed particles. The hard fragmentation of heavy quarks also permits the enhancement of the charm signal. The momentum fraction, x_D , of the D candidate compared to the incident proton is evaluated in the γp centre-of-mass system. True D candidates tend to have large x_D , a fact which also implies that the leading particles in jets will preferentially come from D mesons. By utilising these effects a clear charm signal can be obtained by suitable selections on both leading particles and x_D .

The second method to enhance charm uses high p_T leptons, usually muons, as a signal for inclusive charm production. Since bottom production is negligible at current HERA luminosities, a cleanly identified high p_T lepton is an excellent signature for charm production.

5.4.4.1 Photoproduction of charm

Figure 24 shows the cross-sections obtained by ZEUS ¹⁰⁰ and H1 ¹⁰¹. The signals were obtained using the methods discussed in the previous section, and are plotted as a function of W , together with low energy data from fixed target experiments ¹⁰². The solid curve shows the predictions of a next to leading order QCD model by Frixione *et al.* ¹⁰³, using as input the proton structure function parameterisation of $MRSD - '44$ and the photon structure prediction due to Glück, Reya and Vogt ¹⁰⁴. The dotted lines on either side of the solid line show the variation in the cross-section obtained using alternative parameterisations which are broadly compatible with the data on photon and proton structure functions. The size of these variations and the fact that they depend on the photon structure as well as the proton structure imply that much more data will be necessary before this method can lead to an accurate determination of the gluon density in the proton.

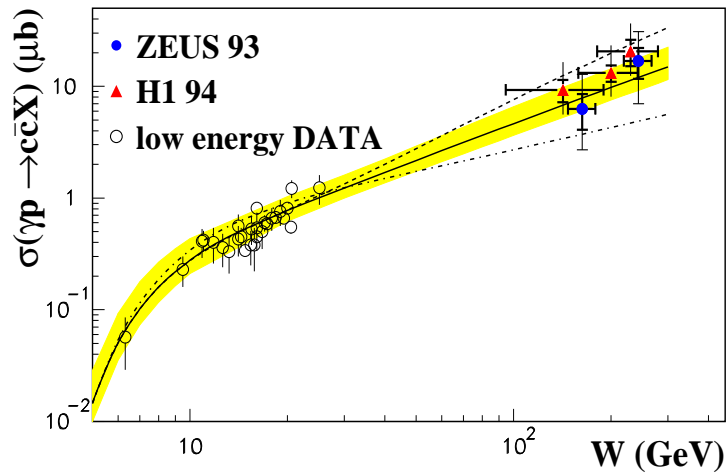


Fig. 24. The total cross-section for charm photoproduction as a function of W derived from the observation of inclusive D^* mesons. The solid circles represent the ZEUS results, while the triangles are data from H1. The open circles show data from fixed-target experiments¹⁰². The solid line shows the predictions of the model by Frixióne *et al.*, based on the $MRSD'$ and GRV(HO)¹⁰⁴ structure functions for the proton and photon respectively. The shaded area shows the uncertainty due to renormalisation scale. The higher dotted line shows similar predictions based on $MRSD'$ and LAC1¹⁰⁷, while the lower dotted line is based on $MRSD_0$ and GRV(HO).

5.5 Summary

The above data demonstrate that a consistent picture is emerging for the gluon density using a variety of different methods, including the “classic” method of scaling violations in DIS. Now that next-to-leading order corrections are available, the measurement of $G(x)$ from jet rates should become more important. At the moment however, the other methods are really only consistency checks. A better understanding of the theoretical uncertainties but in particular more precise data are required before a measurement of $G(x)$ can be obtained from inclusive charm and vector meson production.

6 Determination of F_2^{charm}

Our discussion of the quark and gluon content of the proton concludes with the determination of the fraction of F_2 arising from the production of charm. This is not only a measure of part of the quark content of the proton, but, since it is dominated by boson-gluon fusion, it is very sensitive to the gluon density. Thus this topic unites the previous two sections.

Both the H1 and ZEUS experiments have observed signals for the production of charmed mesons in deep inelastic scattering events. The experiments select DIS events as described in section 4. Both the ZEUS¹⁰⁵ and H1¹⁰⁶ collaborations have published data using rather similar methods; we concentrate on a discussion of the H1 analysis in this section.

Events containing D mesons are selected via methods described in the previous section. The events are restricted by the requirement for high efficiency for the trigger and the reduction of photoproduction background to the kinematic region $y < 0.53$ and $10 \text{ GeV}^2 < Q^2 < 100 \text{ GeV}^2$. H1 isolate signals from both D and D^* production, in the former into $K\pi$ and in the latter into $K\pi\pi_{slow}$. The D^0 events are isolated by employing a selection on x_D , whereas D^* events are obtained by use of the kinematic properties of the slow pion. Clear signals are obtained for both channels. The two samples lead to differential cross-sections and other kinematic quantities which are in good agreement, justifying taking an average of both channels. This leads to a total charm cross-section of

$$\sigma(ep \rightarrow c\bar{c}X) = (17.4 \pm 1.6 \pm 1.7 \pm 1.4) \text{ nb.} \quad (64)$$

where the errors are statistical, systematic, and dependent on the Monte Carlo model used to extrapolate to the full phase-space, respectively. This cross-section is somewhat higher than that expected in theoretical predictions based on NLO calculations^{108,109}.

The normalised x_D distributions are able to discriminate between possible charm production mechanisms. The x_D distribution is sensitive to both the fragmentation function of the charm quark and to the charm production spectrum. Assuming a universal fragmentation as determined dominantly by the LEP experiments, then the x_D distribution strongly supports the boson-gluon fusion production mechanism for charm.

The H1 data is binned into 9 bins in Q^2 and x and the cross-section determined per bin, corrected for QED radiation, is converted into F_2 using equation 28 under the assumption that F_L is zero. The result, together with the ZEUS data, which extends the data to somewhat lower Q^2 , is shown in figure 25. At the current level of accuracy, the data are in reasonable agreement with the predictions from the GRV parton distributions. Low energy data from EMC¹¹⁰ suggested a strong increase of the ratio F_2^{charm}/F_2 as a function of Q^2 . Such an effect is not seen in the ZEUS and H1 data, which is compatible with no increase with Q^2 . The average fraction

which F_2^{charm} contributes to F_2 is determined by H1 to be

$$0.237 \pm 0.021^{+0.043}_{-0.039}$$

a growth of about an order of magnitude compared to the EMC result, in agreement with the strong rise in the gluon density at small x . The ZEUS analysis leads to a similar result. Thus charm quark production forms a sizeable fraction of all the leading quarks produced in DIS, particularly at low x .

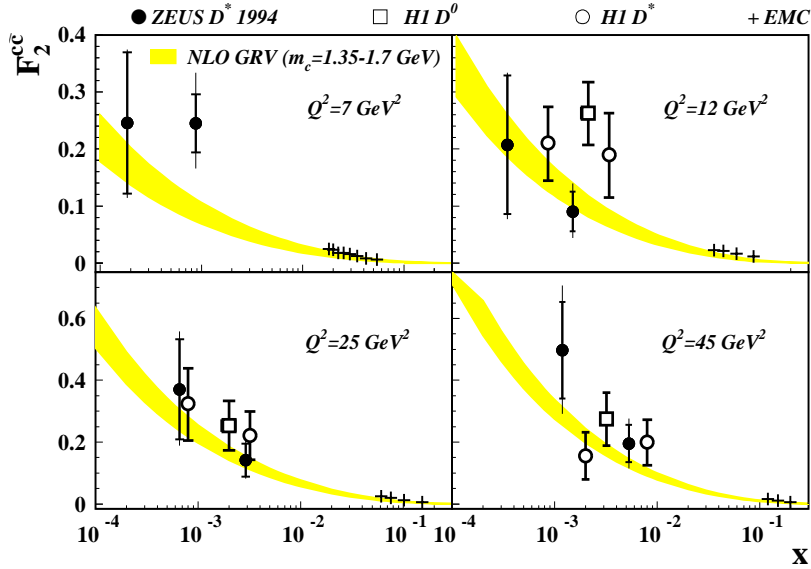


Fig. 25. F_2^{charm} as measured from D^0 events by H1 (open squares) and D^* events by H1 (open circles) and ZEUS (closed circles). For the ZEUS data, the inner error bars on the data points are the statistical errors, the full bars correspond to statistical and systematic errors added in quadrature. The error bars on the H1 points correspond to the statistical and systematic errors added in quadrature. The shaded band shows the result of the NLO QCD prediction based on the GRV-HO parton distributions; the width of the band corresponds to varying m_c between 1.3 and 1.7 GeV. Data from EMC¹¹⁰ are also shown as crosses.

7 Properties of the final state in Deep Inelastic Scattering

The large increase in centre of mass energy at HERA greatly improves the sensitivity of studies in perturbative and non-perturbative aspects of QCD compared to fixed target experiments. Studies of inclusive distributions have been made in both the γ^*p centre of mass system and in the Breit frame, and the general features compared with e^+e^- annihilation. In addition both H1 and ZEUS have studied details of fragmentation by the observation of inclusive strange neutral particle production. Finally, studies on perturbative aspects of QCD have been carried out by studying energy flows and inclusive jet production.

7.1 Inclusive charged particle distributions

7.1.1 Distributions in the γ^*p CM system

Inclusive particle distributions in neutral current deep inelastic scattering are sensitive both to the hadronisation process and to the underlying QCD processes at the parton level. We first discuss charged particle distributions in variables aligned with the exchanged virtual photon; the fractional momentum along the virtual photon direction known as the Feynman variable, $x_F = 2p_l^*/W$, where p_l^* is the track momentum along the virtual photon direction, and the momentum perpendicular to the virtual photon direction, p_T^* . In H1, charged tracks reconstructed in the central jet chamber were used in the analysis provided that they were of good quality and associated with the primary event vertex. In order to keep within the well-understood and high-acceptance region of the detector charged tracks were required to satisfy $0.15 < p_T < 10$ GeV and $22^\circ < \theta < 158^\circ$. Charged tracks in ZEUS are reconstructed principally using the Central Tracking Detector. Only those charged particles with $p_T > 0.2$ GeV and $25^\circ < \theta < 155^\circ$, where θ is the polar angle, are analysed. This restricts the range in Q^2 and W to $10 < Q^2 < 160$ GeV² and $75 < W < 175$ GeV.

Figure 26 shows the differential charged hadron multiplicities for deep inelastic scattering events, excluding those with a large rapidity gap in the forward direction indicative of a diffractive type interaction (see section 8). The distributions from both H1¹¹¹ and ZEUS¹¹² are shown as a function of x_F , while the ZEUS data is shown versus p_T^* . Also shown is the H1 and ZEUS $\langle p_T^{*2} \rangle$ as a function of x_F , the so-called “seagull” plot. The H1 and ZEUS data are in good agreement, and show the typical features associated with hard gluon radiation. This is particularly visible in the seagull plot, where much greater p_T is developed than expected from the naive quark parton model. On the assumption that fragmentation is a long-distance phenomenon and does not depend on the details of the perturbative origin of the fragmenting quarks, it would be expected that the general features of DIS events would be similar to those from e^+e^- , provided that one half of the multiplicity observed in e^+e^- is compared with the DIS multiplicity (since the current jet corresponds to the fragmentation of one quark or antiquark, whereas in e^+e^- both quark and antiquark fragment). This picture does indeed seem to be borne out by the HERA data. Figure 27 shows the ZEUS data in comparison to data from the DELPHI experiment¹¹³ at a similar mean W . It can be seen that the ZEUS and e^+e^- data are in good agreement with each other and with the solid line which is the prediction of the MEPS model. In contrast, the lower energy data from fixed target μp scattering are consistent with the quark-parton model prediction and do not agree with the ZEUS data. Similar results have been obtained by H1¹¹⁴, who also observe KNO scaling¹¹⁵ with similar characteristics to that observed in e^+e^- annihilation, and discuss detailed comparisons with Monte Carlo models and hadron-hadron scattering.

Figure 28 shows $\langle p_T^{*2} \rangle$ as a function of W for different ranges of x_F . The ZEUS data agree well with the predictions of the MEPS model, shown as a solid line, and show a much steeper rise in $\langle p_T^{*2} \rangle$ than the fixed target data for a similar range in W . Figure 29 shows that $\langle p_T^{*2} \rangle$ for the ZEUS data increases strongly with Q^2 , in contrast with the EMC data which show almost no rise over a similar range of Q^2 . Thus the expected rise in $\langle p_T^{*2} \rangle$ due to hard gluon radiation can be more clearly seen in the HERA data than in the EMC data, where the phase space for gluon radiation is severely restricted.

H1¹²² have also used the transverse momentum spectra of charged particles as a function of Q^2 and x to study various models of fragmentation and soft gluon radiation. For $x > 0.001$, all models give a good description of the data. For smaller x , however, and in the central rapidity region, the p_T distributions are significantly higher than the MEPS (LEPTO 6.4) and HERWIG 5.8¹²³ predictions, but in

ZEUS 1993

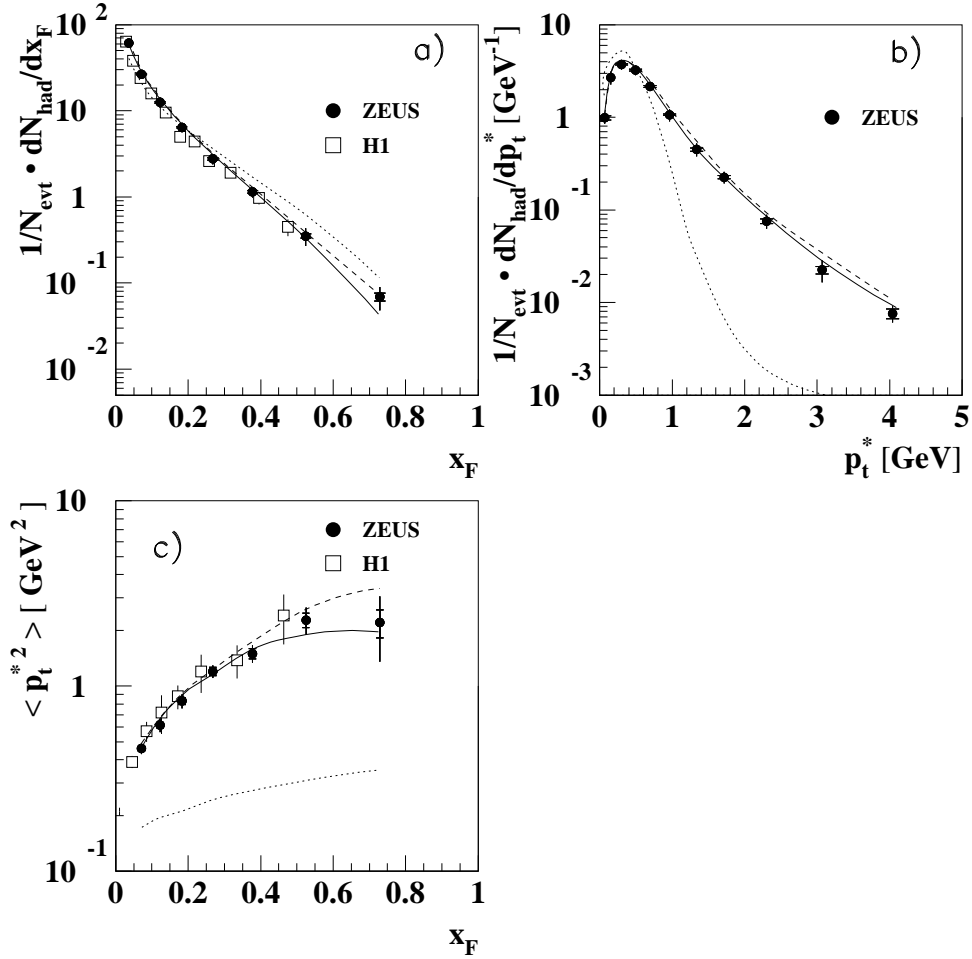


Fig. 26. Differential normalised charged hadron multiplicities for DIS events as a function of a) x_F b) p_{T^*} for $x_F > 0.05$ c) $\langle p_{T^*}^2 \rangle$ as a function of x_F . The solid line shows the result of the MEPS¹¹⁶ Monte Carlo model, whereas the dashed curve is the result of CDMBGF¹¹⁷. The dotted curve shows the result of a phase-space model which does not include hard gluon radiation and therefore corresponds to the expectation from the naive quark-parton model.

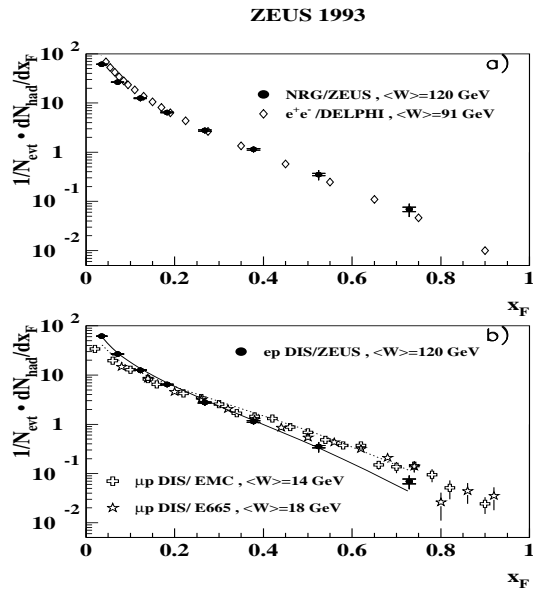


Fig. 27. a) Normalised x_F distributions for charged particles for the ZEUS deep inelastic scattering data together with the distribution for e^+e^- data from the DELPHI experiment ¹¹³ at similar $\langle W \rangle$. b) ZEUS data in comparison with fixed target data at much lower $\langle W \rangle$ from EMC ¹¹⁸ and E665 ¹¹⁹. The solid line is the prediction of the MEPS Monte Carlo model ¹¹⁶. The dotted line shows the prediction from a phase space model excluding the effects of hard gluon radiation.

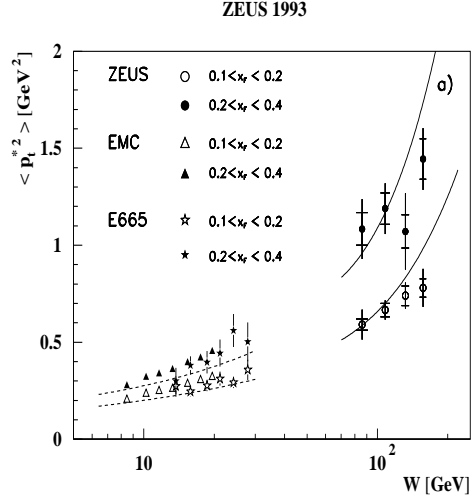


Fig. 28. $\langle p_T^{*2} \rangle$ distributions in two ranges of x_F for charged particles for the ZEUS deep inelastic scattering data together with the EMC¹²⁰ and E665¹²¹ distributions at lower $\langle W \rangle$. The solid line shows the prediction from the MEPS Monte Carlo model, the dotted line shows the prediction from a phase space model excluding the effects of hard gluon radiation.

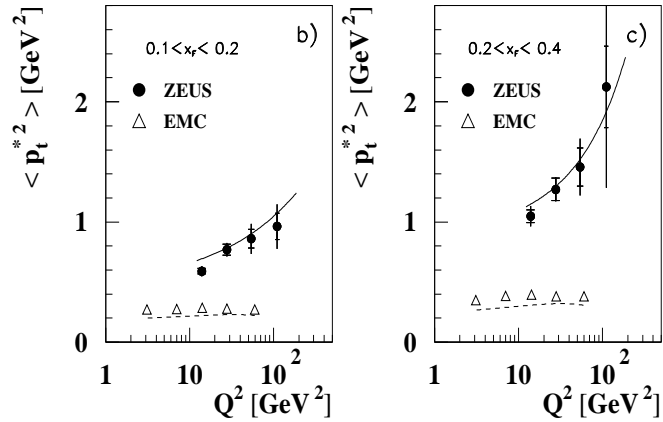


Fig. 29. $\langle p_T^{*2} \rangle$ distribution as a function of Q^2 for the ZEUS and EMC experiments for two different ranges in x_F . The solid line shows the prediction from the MEPS Monte Carlo model, the dotted line shows the prediction from a phase space model excluding the effects of hard gluon radiation.

good agreement with the ARIADNE 4.08 predictions. Such an excess of high p_T in the central region would be expected in models in which BFKL behaviour (see section 7.4) was important.

7.1.2 Distributions in the Breit Frame

In ep collisions, in contrast to the situation in e^+e^- , there is no “natural” frame in which to study fragmentation effects. In the γ^*p centre of mass system discussed in the previous section, the struck quark is back-to-back with the proton remnant in the naive quark-parton model. In the Breit frame, the struck quark is back-to-back with the exchanged virtual photon, so that in the naive quark-parton model the momentum of the quark is $Q/2$ before the interaction and $-Q/2$ after it, where Q^2 is the virtuality of the exchanged photon. Since in this frame the quark scattering can be viewed as a t -channel process closely related to the s -channel $e^+e^- \rightarrow q\bar{q}$, it is a particularly suitable frame in which to compare with e^+e^- results. The direction of the outgoing struck quark defines a hemisphere to which particles may be assigned and considered as part of the current fragmentation region. However, there is ambiguity in this assignment which complicates the comparison with e^+e^- particularly at low Q .

Both ZEUS¹²⁴ and H1¹²⁵ have published results on charged particle distributions in the Breit frame. The variable used is normally x_p , where $x_p = 2p/\sqrt{s}$, together with the related variable $\xi = \ln(1/x_p)$. QCD in the modified leading log approximation predicts that at the parton level ξ is approximately Gaussian and that the maximum of ξ increases as Q . Figure 30 shows the evolution in the H1 data¹²⁶ of both the maximum and the width of the ξ distribution as a function of Q , together with predictions from a modified leading logarithm approximation (MLLA) QCD model¹²⁷. There is good agreement between the H1 and ZEUS¹²⁴ data and between the DIS and e^+e^- data¹²⁸ (note that the e^+e^- data has been refitted to make it directly comparable to the H1 results). Although the HERA data agree quite well with the MLLA predictions, other models with varying degrees of QCD coherence are also able to give good fits. H1 finds essentially no dependence of the peak of ξ on the Bjorken x of the DIS event, so that the evolution takes place only as a function of Q , as predicted by MLLA QCD.

In summary, the features of the HERA data do indeed generally support QCD based models and the general process independence of fragmentation.

7.2 Production of neutral strange particles in DIS

In principle the study of strange particles can give information on both the strange quark content of the proton and the flavour properties of fragmentation. In practice however it is very difficult to disentangle these two aspects since the rate of strange particles is dominated by the production via fragmentation.

The long lifetimes of the K^0 and Λ mean that very clear signals with small backgrounds can be obtained by selecting tracks which are not associated with the primary production vertex. Reasonable agreement between the H1¹²⁹ and ZEUS¹³⁰ results is observed. Both experiments observe that the rate of neutral strange particle production increases logarithmically with W , in line with expectations from QCD. By comparing the rates of K^0 and Λ production with predictions of Monte Carlo models, both experiments find that the default value of 0.3 for the ratio of strange to non-strange quark production in fragmentation in the JETSET hadronisation scheme is too high, and prefer values nearer to 0.2, in agreement with observations at LEP¹³¹ and in previous DIS experiments¹³². However, there are some indications of a disagreement between ZEUS and H1 in the rate of Λ production; ZEUS observe that even with the smaller value for the strangeness suppression

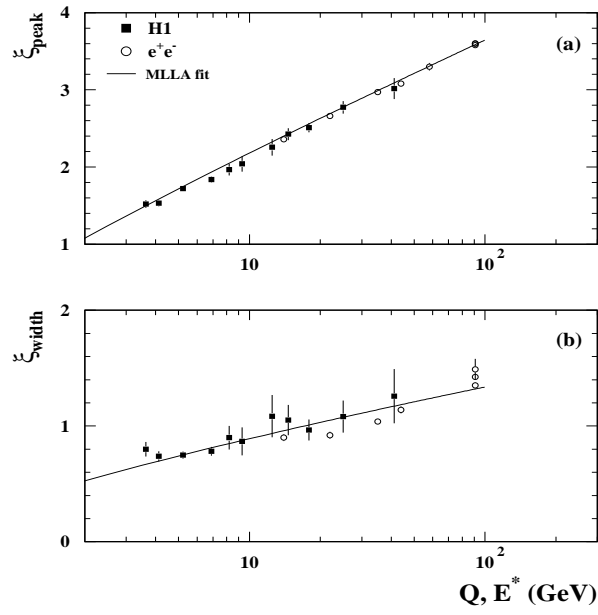


Fig. 30. a) The peak position and b) the width of the ξ distribution according to a Gaussian fit. Data from H1 and e^+e^- experiments are shown. The solid line is a 2 parameter MLLA fit to the H1 data.

the data lie somewhat below the Monte Carlo, whereas H1 are broadly compatible. However, more data will be required to determine if this is a real disagreement and hence whether other fragmentation parameters of the models need to be tuned.

H1 have also investigated the possible production of QCD instantons. Were such objects to be produced at HERA, large changes in the number of strange particles produced in the final state would be expected¹³³. The production rate of K^0 is compared to standard fragmentation models plus an instanton model; there is no evidence for anomalous K^0 production, leading to an upper limit on the production cross-section for instantons of 0.9 nb at 95% confidence level.

7.3 Determination of α_s from jet multiplicity

At high Q^2 the strongly accelerated struck quark from the proton can radiate hard gluons which may lead to resolvable jets in the final state. The rate of jet production is thus proportional to the value of the strong coupling constant, α_s . Measurement of this jet rate in a kinematic region which minimises uncertainties from parton distribution functions and hadronisation can therefore lead to a measurement of α_s .

Both H1¹³⁴ and ZEUS¹³⁵ have measured α_s using the above technique. Jets are found using the JADE jet algorithm¹³⁶. The rate of events containing two identifiable jets together with the forward jet resulting from the break-up of the proton (“2+1” jet events) was compared with the rate expected in a Monte Carlo model including next to leading order QCD effects. The effect of hadronisation on this rate is large and varies depending on the exact criteria used in defining a jet. In order to reduce uncertainties in the hadronisation process and to avoid the very forward region which is not well modelled, the two experiments made the following cuts :

H1: $10 < Q^2 < 100 \text{ GeV}^2$; $y < 0.5$ and $Q^2 > 100 \text{ GeV}^2$; $y < 0.7$

ZEUS: $0.1 < y < 0.95$, $0.01 < x < 0.1$ and $120 < Q^2 < 3600 \text{ GeV}^2$.

For both sub-samples, the additional cut $W > 5000 \text{ GeV}^2$ was also imposed. The variable $y_{ij} = m_{ij}^2/W^2$, where i and j are two massless objects (in this case jets) was used to define resolved jets. A cut in this variable, $y_{cut} > 0.02$, was applied by both experiments. In addition, H1 restrict the polar angle of the jets to $10^\circ < \theta_{jet} < 145^\circ$, which reduces the dependence on the influence of parton showers (10° cut) and improves the measurement of the jet energies (145° cut).

With the above cuts good agreement was obtained between the data and NLO QCD models for the rate of “2+1” jet events. H1 divided their data into 5 bins in Q^2 while ZEUS used 3 bins. The values of α_s obtained by H1 are shown in figure 31 and indicate a variation with Q^2 . Averaged over the full Q^2 range and evolving to $Q^2 = M_Z^2$, the experiments obtain values of α_s at the Z mass of

$$\begin{aligned}\alpha_s(M_Z) &= 0.117 \pm 0.005(stat.)_{-0.009}^{+0.008}(syst.) : (\text{ZEUS}) \\ \alpha_s(M_Z) &= 0.123 \pm 0.005(stat.) \pm 0.013(syst.) : (\text{H1})\end{aligned}$$

which can be averaged to give $0.121 \pm 0.004 \pm 0.008$. This is in good agreement with the world average value from all determinations of 0.118 ± 0.003 ¹³⁷.

7.4 Transverse energy flow and forward jet production

The distribution of transverse energy and/or production of forward jets is in principle a sensitive test of the underlying QCD dynamics. The large increase in the

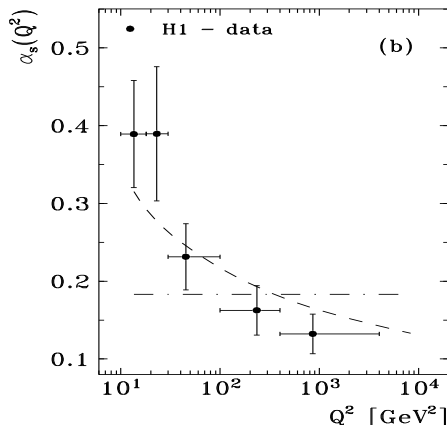


Fig. 31. Measured values of α_s for five different Q^2 regions. Only statistical errors are shown. The dashed lines show the QCD prediction and the dashed-dotted line shows a fit assuming that α_s is constant.

accessible kinematic domain provided by HERA leads to the possibility of exploring QCD in qualitatively different regimes. The DGLAP¹⁴ approach to QCD evolution of partons re-sums the leading logarithmic terms of the form $\alpha_s \ln Q^2$ in the QCD expansion. This results in a “strong ordering” in the transverse momentum of the gluons emitted between the struck quark, or “current” jet, and the proton remnant, such that gluons emitted near to the current jet direction have much larger p_T than those emitted close to the proton direction. In contrast, the BFKL¹⁵ approach re-sums the leading logarithmic terms of the form $\alpha_s \ln 1/x$, resulting in a strong ordering in x but no such ordering in transverse momenta. Thus one might qualitatively expect that, in a region in which the BFKL approach was appropriate (e.g. $1/x \gg Q^2$), there would be an excess of transverse energy in the region between the proton remnant and the current jet compared to the prediction of a DGLAP based model. In particular, BFKL dynamics would predict that the average level of transverse energy per unit pseudorapidity η in the forward direction would grow as x^{-1} . Similarly, the production of jets with $p_T^2 \sim Q^2$ and $x_{jet}(= E_{jet}/E_p) \gg x$ is strongly suppressed according to DGLAP but not BFKL. The kinematics of such jet production clearly imply that it will be dominantly in the forward direction close to the proton remnant.

The energy observed as a function of η has been shown by both H1¹³⁸ and ZEUS¹³⁹, and there does indeed seem to be an excess in the forward direction compared to the expectation from simple models based on standard DGLAP evolution. H1 prefer to work in the central rapidity region of the hadronic centre of mass system. At fixed Q^2 the mean transverse energy rises with $1/x$ as predicted by the BFKL equation¹⁴⁰. However, conventional DGLAP based models can also be tuned to reproduce the data by increasing the E_T produced in the hadronisation i.e. non-perturbative phase.

H1 have also observed jets in the very forward region^{141,142}. The jets are well separated and show typical jet properties despite being in the difficult area very

close to the proton remnant. The preliminary jet cross-section from ¹⁴² shows a steep rise as x falls which is significantly above the DGLAP-based models and falls between a parton-level analytical BFKL calculation ¹⁴³ and the CDM1 Monte Carlo ¹¹⁷, based on the colour dipole model of fragmentation. To the extent that some aspects of the CDM model mimic properties of BFKL, this is clearly a very interesting preliminary result, which needs to be compared to a full Monte Carlo model which explicitly contains the BFKL dynamics.

In summary, although the behaviour of many aspects of the data at low x is as expected from BFKL dynamics, conventional DGLAP-based models also seem able to describe the data after appropriate tuning. This is a similar situation to that discussed in section 4.1. However, the ability to look at exclusive aspects of the DIS data, such as forward jet production, does seem to offer greater hope of finding a real discriminant between the DGLAP and BFKL regimes of QCD. This can only be convincing however when a comparison with a BFKL-based Monte Carlo model is possible.

8 The structure of diffraction

By far the most likely processes to occur in the scattering of two hadrons are elastic scattering (in which the two hadrons emerge unscathed and with a relatively small deviation) or diffractive scattering (in which one of the two hadrons is excited into a relatively high mass state and the other remains unexcited and emerges with a large rapidity gap with respect to the excited system.) The description of these phenomena has been a puzzle for many decades. In the Regge picture of strong interactions, these processes were considered to be mediated by a ‘‘Pomeron’’, which however did not correspond to any known real particle and had the quantum numbers of the vacuum. In the modern language of QCD, a self-consistent picture of diffraction is complicated since elastic and diffractive scattering are of their nature predominantly soft, low momentum transfer processes where the tools of perturbative QCD are not valid (for a review see Goulianos ¹⁴⁴).

In the last few years a very striking class of events have been observed both in high energy proton-antiproton interactions ^{145,146,147} and in deep inelastic scattering ^{148,149}, in which there are large gaps in rapidity space which contain no particles. A natural interpretation is that such events correspond to diffractive processes ^{150,151}. The very large phase space available at HERA allows a systematic study of the mechanism of diffraction at momentum transfers large enough for a perturbative QCD analysis to be valid. This in turn allows an investigation of possible partonic structure in the exchanged object. Without loss of generality, we shall refer to this object generically as ‘‘the Pomeron’’.

In this section we will briefly discuss the kinematic characteristics of diffractive events at HERA, before proceeding to a more detailed study of their properties and nature.

8.1 Kinematic considerations in diffraction

As discussed in section 3.3, fully inclusive deep inelastic scattering can be described in terms of two structure functions which in principle depend on two invariants. In the case of diffractive events, it is assumed that the process being observed is of the form

$$e + p \longrightarrow e + p + X \tag{65}$$

where the proton is either observed using specialised silicon detectors far upstream of the interaction point or is inferred from the characteristics of the event[‡]. An extra

[‡]The excitation of the proton into an N^* resonance may also satisfy the criteria for diffraction.

two invariants, and if the final-state proton is measured, in principle an extra two structure functions, are required to fully specify the process. Fortunately in the kinematic regime of interest the two extra structure functions are negligible¹⁵². The invariants are usually chosen to be the familiar x , Q^2 together with two of the following set:

$$\begin{aligned} x_{\mathcal{P}} &= \frac{q \cdot (P - P')}{q \cdot P} \\ \beta &= \frac{-q^2}{2q \cdot (P - P')} \\ t &= (P - P')^2 \end{aligned} \quad (66)$$

where P, P' are the initial and final momenta of the proton and t is the four-momentum transfer at the incident proton vertex. The variables $x_{\mathcal{P}}$ and β can be expressed in terms of W^2 and M_X , (the invariant mass squared of the total hadronic system and the system excluding the scattered proton, respectively), as

$$x_{\mathcal{P}} \simeq \frac{M_X^2 + Q^2}{W^2 + Q^2} \simeq x_{\mathcal{P}/p} \quad (67)$$

$$\beta = \frac{x}{x_{\mathcal{P}}} \simeq \frac{Q^2}{M_X^2 + Q^2} \simeq x_{q/\mathcal{P}} \quad (68)$$

In the kinematic regime of HERA, in which Q^2 and W^2 can be very large and t is small, $x_{\mathcal{P}}$ may be interpreted as the fraction of the proton's momentum carried by the Pomeron, while β can be interpreted as the fraction of the momentum of the Pomeron carried by the charged constituent which interacts with the virtual photon. From these considerations the differential cross-section can be written, following equation 15, as

$$\begin{aligned} \frac{d^4\sigma}{dx dQ^2 dx_{\mathcal{P}} dt} &= \frac{2\pi\alpha^2}{xQ^4} [\{1 + (1 - y)^2\} F_2^D(x, Q^2, x_{\mathcal{P}}, t) \\ &- y^2 F_L^D(x, Q^2, x_{\mathcal{P}}, t)] \end{aligned} \quad (69)$$

where for the moment we have ignored radiative corrections as well as the possibility of charged current interactions. It is also normal to assume, similar to the case for normal non-diffractive DIS, that F_L is small and can be ignored, although, as will be seen below, the high gluon content of the Pomeron implies the possibility that this assumption may not necessarily be a good one.

In soft hadronic physics and inclusive processes, a universal Pomeron which ‘‘factorises’’, i.e. whose flux inside the proton is independent of the specific interaction, has been found to give a good representation of the data in a variety of processes^{153,154}. It is a reasonable, though unproven, hypothesis that similar factorisation occurs in the hard diffractive interactions discussed here. If this is indeed true, then equation 69 can be written as

$$\frac{d^4\sigma}{dx dQ^2 dx_{\mathcal{P}} dt} = f_{\mathcal{P}/\mathcal{P}}(x_{\mathcal{P}}, t) \frac{d^2\sigma}{d\beta dQ^2} \quad (70)$$

where $f_{\mathcal{P}/\mathcal{P}}(x_{\mathcal{P}}, t)$ is the universal Pomeron flux in the proton. Thus in analogy to the definition of the F_2 structure function we can identify a ‘‘Pomeron structure

function" F_2^{IP} such that

$$\frac{d^2 F_2^D(x, Q^2, x_{\mathcal{P}}, t)}{dx_{\mathcal{P}} dt} = f_{P/IP}(x_{\mathcal{P}}, t) F_2^{IP}(\beta, Q^2) \quad (71)$$

where β plays the same role as Bjorken- x in normal DIS.

Finally, in results published to date the scattered proton has not been detected and hence t is undetermined. Integrating over t in equation 69 leads to

$$\frac{d^3 \sigma_{diff}}{dQ^2 d\beta dx_{\mathcal{P}}} = \frac{2\pi\alpha^2}{\beta Q^4} (1 + (1 - y)^2) F_2^{D(3)}(Q^2, \beta, x_{\mathcal{P}}) \quad (72)$$

8.2 Experimental results

In retrospect, it was entirely to be expected that diffractive processes would be important at HERA. Nevertheless, the discovery of the so-called ‘‘rapidity gap events’’^{148,149}, came as a great surprise to the ZEUS and H1 experimental teams. Not only did these events have a spectacular experimental signature, they also represented a significant fraction of the DIS cross-section, initial measurements suggesting about 10%. The initial studies by the two experiments isolated diffractive events on the basis of a lack of activity between the current jet and the proton direction. By making cuts in each event on η_{max} , the largest pseudo-rapidity in the detector having a significant energy deposit, or on the largest gap between significant energy deposits, a sample of diffractive events with high efficiency and little background could be obtained.

Data taken by ZEUS and H1 in 1993 allowed a first measurement of the partonic structure of the Pomeron^{155,156}. The two collaborations found evidence that the factorisation hypothesis was approximately satisfied, i.e. that the flux was independent of the kinematics of the Pomeron-photon interaction, (β and Q^2) but was a universal function of $x_{\mathcal{P}}$, namely $x_{\mathcal{P}}^{-\lambda}$. In addition they were able to determine the integrated structure function,

$$\tilde{F}_2^D(\beta, Q^2) = \int_{x_{\mathcal{P}L}}^{x_{\mathcal{P}H}} F_2^{D(3)}(\beta, Q^2, x_{\mathcal{P}}) dx_{\mathcal{P}}, \quad (73)$$

in a number of bins of β and Q^2 . \tilde{F}_2^D can be thought of as the ‘‘structure function of the Pomeron’’, although it is important to bear in mind that, since the integration over $x_{\mathcal{P}}$ in general covers a range kinematically inaccessible for certain values of β and Q^2 , \tilde{F}_2^D does not represent the diffractive fraction of the experimentally measured F_2 . Although the errors are large, and the number of bins small, a relatively hard parton structure consistent with scaling in Q^2 was found. This approximate scaling, as well as the observation of jet structure in diffractive events¹⁵⁷, supports the picture that the Pomeron contains point-like interacting constituents.

More recently the two experiments have been able to make significant further progress. H1 has used the data taken in 1994, which gives almost a factor of ten improvement in integrated luminosity over that taken in 1993, to make much more detailed measurements of the parton structure of diffraction. ZEUS has introduced a model independent method of subtracting the non-diffractive background by fits to data distributions and used this method to determine the diffractive structure function using 1993 data. ZEUS has also used data from hard photoproduction to constrain the parton content of the Pomeron.

8.2.1 Preliminary H1 analysis of 1994 data

Although the analysis discussed here remains preliminary at the time of writing, the information presented to the 1996 Warsaw Conference ¹⁵⁸ is of sufficient interest to warrant its inclusion in this review.

The greatly increased statistics allow H1 to study diffraction over a significantly larger kinematic range. The variables used to describe the diffractive final state are functions of the variables M_X, x, y and Q^2 (see equation 68). Good reconstruction of M_X is assured by using the hadronic measurement and cutting on η_{max} in order to ensure that the hadronic system is well contained within the detector. The Σ method (see section 3.4) is used to reconstruct the other kinematic variables.

The data thus obtained are used to measure the diffractive cross-section in bins of $x_{\mathbb{P}}, \beta$ and Q^2 in the kinematic range $2.5 < Q^2 < 65 \text{ GeV}^2$, $0.01 < \beta < 0.9$ and $10^{-4} < x_{\mathbb{P}} < 0.05$. The cross-section is then converted into the structure function $F_2^{D(3)}$ using equation 72, correcting for backgrounds, losses, migration etc. bin by bin using Monte Carlo models.

Figure 32 shows $x_{\mathbb{P}} \cdot F_2^{D(3)}$ in bins of β and Q^2 . The data, particularly in the region $\beta < 0.2$, are inconsistent with the factorisation hypothesis, which predicts that $F_2^{D(3)}$ has the same dependence on $x_{\mathbb{P}}$ independent of β and Q^2 . The curves are fits to the form

$$A(\beta, Q^2)x_{\mathbb{P}}^{-n(\beta)} \quad (74)$$

where

$$n(\beta) = b_0 + b_1 \cdot \beta + b_2 \cdot \beta^2 \quad (75)$$

It can be seen that such a parameterisation gives a good description of the data. There are several possible explanations for this departure from factorisation. The most straightforward is that factorisation is simply invalid and that therefore models in which factorisation is not assumed (see for example the review by McDermott and Briskin ¹⁵⁹), or in which factorisation in soft diffraction processes is broken to satisfy unitarity (see for example the review by Goulianos ¹⁶⁰), are preferred. It is also possible that the observed behaviour is indicative of the importance of non-leading Regge trajectories, such as the $f_2^0(1270)$, which must indeed contribute at some level if the Regge picture is valid. If the partonic structure of such exchanges were to be significantly softer than the Pomeron then this could explain the behaviour of the data. Since unfortunately there is no information on the structure function of the f_2 , this is allowed to vary in a fit. H1 has carried out such a fit which does indeed give a good representation of the data and leads to values of intercepts of the trajectories which are consistent with what would be expected for the Pomeron and f_2 .

Despite the complication due to the violation of factorisation, it is still possible to obtain information on the partonic structure of the exchanged trajectories from \tilde{F}_2^D . In this situation this quantity represents some sort of average partonic structure of all contributing exchanges. \tilde{F}_2^D integrated from $x_{\mathbb{P}} = 0.0003$ to 0.05 is shown in figure 33. It is clear that \tilde{F}_2^D is essentially independent of β at fixed Q^2 , whereas it depends logarithmically on Q^2 at fixed β . The most striking aspect of the data is that this rise with $\ln Q^2$ persists even at large values of β , where, had there been a substantial valence quark contribution, the slope would have been negative. We are thus led to the qualitative conclusion that the exchanged trajectories consist dominantly of gluons.

The above conclusion can be made more quantitative by a QCD analysis, assuming a singlet $u + d + s$ quark distribution and a gluon distribution at a starting scale $Q_0^2 = 2.5 \text{ GeV}^2$ and evolving these distributions to higher values of Q^2 using

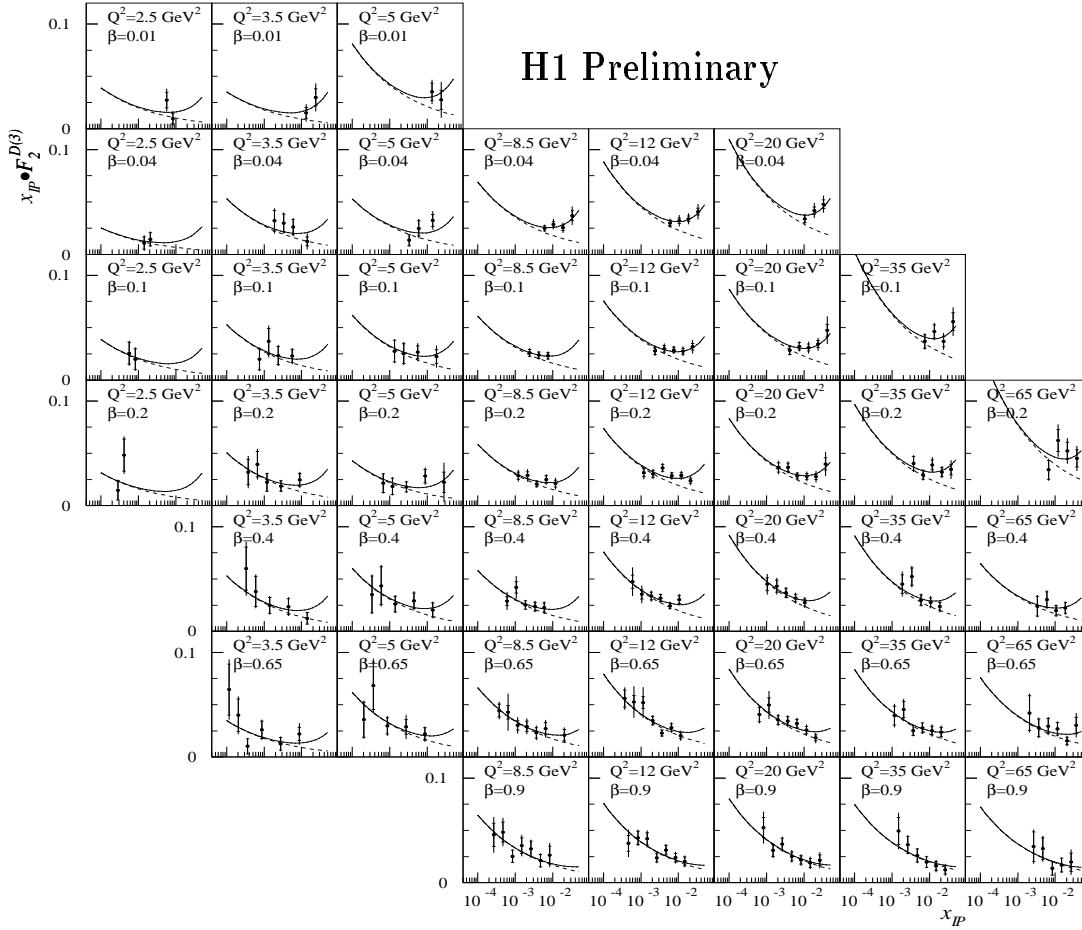


Fig. 32. Plot of $x_{IP} \cdot F_2^{D(3)}$ in bins of β and Q^2 . Statistical and systematic errors have been added in quadrature. The curves show fits to $F_2^{D(3)}$ of the form $x_{IP}^{-n(\beta)}$.

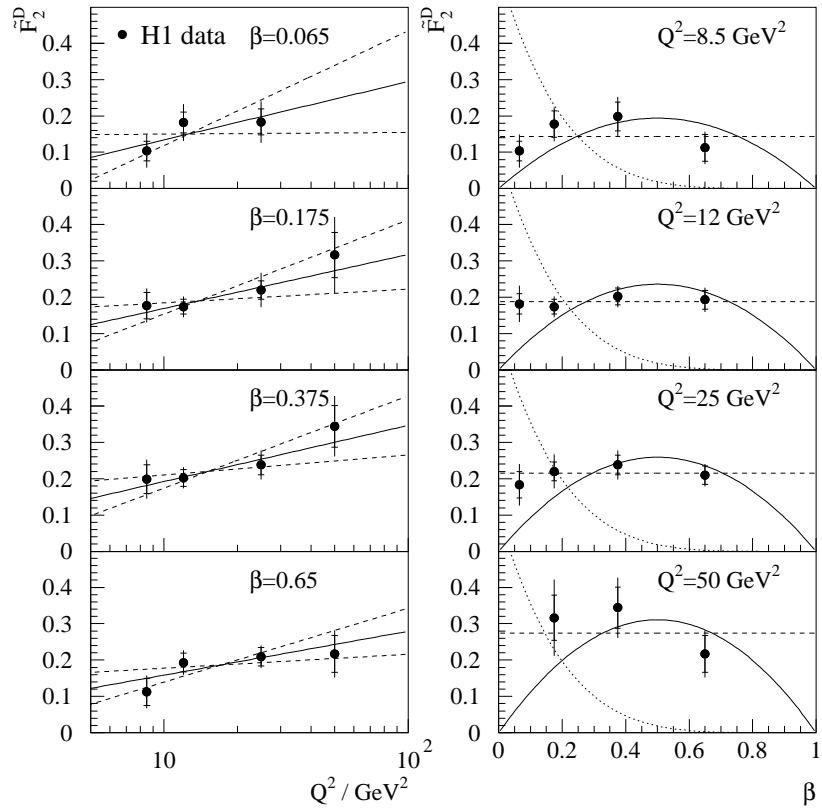


Fig. 33. Plot of \tilde{F}_2^D as a function of Q^2 for different values of β and vice-versa. The solid line on the left-hand plots corresponds to the best fit to a linear $\ln Q^2$ dependence with one sigma errors shown by the dashed lines. The dashed lines in the right-hand plots correspond to the best fits to a constant dependence with β .

the DGLAP equations. No acceptable fit to \tilde{F}_2^D can be obtained if the initial distribution is assumed to be purely quark-like, whereas with a non-zero initial gluon component, excellent fits are obtained. Figure 34 shows the results of such a fit at two values of Q^2 . At low Q^2 the dominance of the gluon is clear; at higher Q^2 the gluon distribution evolves down to lower x . However, in all cases the gluon is dominant in the parton structure of the exchange, with in excess of 80% of the momentum being carried by gluons, in good agreement with models of “leading” gluons (see for example ¹⁶¹).

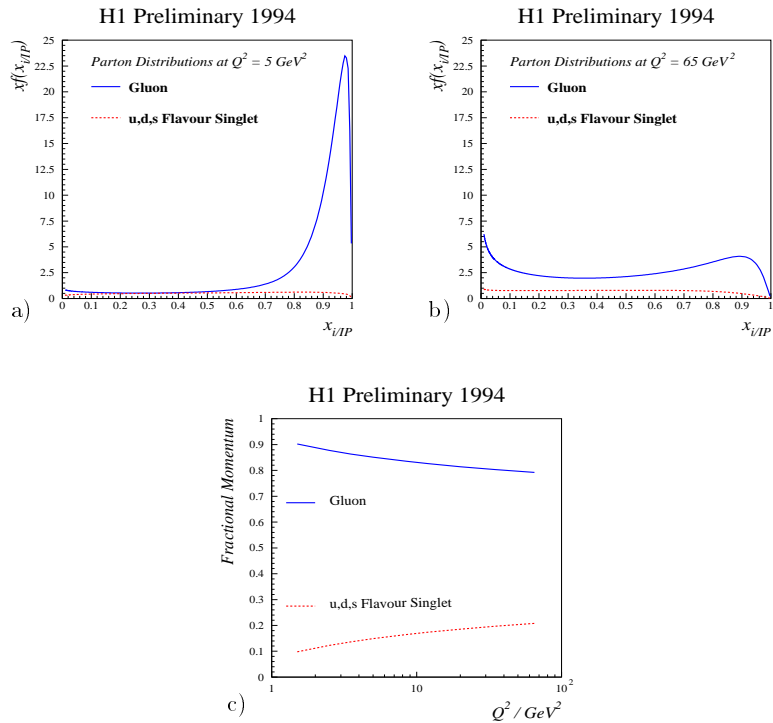


Fig. 34. Results of a DGLAP fit on the H1 \tilde{F}_2^D data at a) $Q^2 = 5 \text{ GeV}^2$ and b) $Q^2 = 65 \text{ GeV}^2$; c) shows the fraction of the total momentum carried by quarks and gluons as a fraction of the total momentum transfer as a function of Q^2 . The errors in these fits are not well determined and are therefore not shown.

It can thus be seen that the H1 data give striking evidence for a “leading” gluon behaviour of the exchange in deep inelastic diffraction, as well as evidence that exchanges in addition to the Pomeron are important. However, it is important to stress that these conclusions are clearly model dependent. The theoretical situation is very confusing, and there is no consensus on many fundamental aspects of the phenomenology. We have already commented on many models which do not assume factorisation ^{153,162,163,164}. Some papers insist that the whole concept of a parton structure of diffraction is controversial ¹⁶⁵. What is clear is that there are alternative

models, for instance making different assumptions about the form factor appropriate to the Pomeron-proton coupling, which can lead to the observed behaviour of \tilde{F}_2^D without implying QCD evolution from a “leading” gluon component. Furthermore, it is unclear whether or not a “direct” point-like coupling of the Pomeron to quarks is appropriate¹⁶⁴. An excellent review of the different types of model can be found in¹⁵⁹.

8.3 ZEUS results in DIS

ZEUS has developed a method of subtracting the non-diffractive background using fits to the distribution of M_X , which is independent of the model used for the diffractive process. It relies on the QCD prediction that in non-diffractive DIS events low M_X values are exponentially suppressed¹⁶⁶. By fitting the data at large M_X and assuming that the slope of the exponential is also valid for non-diffractive DIS events in the small M_X region, a clean model-independent subtraction of the non-diffractive background to the diffractive signal can be made.

This method has been applied to the 1993 data sample¹⁶⁷. The number of background-subtracted diffractive events is converted into a cross-section using kinematic variables calculated using the Double Angle (DA) Method (see section 3.4). The differential cross-section thus derived can be plotted as a function of M_X and fitted to the form $(W^2)^{2\alpha_P-2}$ expected in the Regge picture. The value derived for α_P is around 1.2, somewhat larger than would be expected in a “soft” Pomeron process[§].

The differential cross-section can also be used to determine the diffractive structure function $F_2^{D(3)}$ using equation 72. Since the amount of data available is substantially smaller than the H1 preliminary study discussed in the previous section (which used 1994 data), only a relatively small number of bins was used. The data are consistent with the factorisation hypothesis, and when the data are fit to a form

$$F_2^{D(3)} \propto \left(\frac{1}{x_P} \right)^a \quad (76)$$

gives a value of a of approximately $1.4 \pm 0.04(stat.) \pm 0.08(syst.)$, in good agreement with the previous ZEUS analysis. The 1993 H1 analysis produced a value of n of $1.19 \pm 0.06 \pm 0.07$, which is on the limit of compatibility with ZEUS. The 1994 preliminary H1 analysis is, as we have seen, incompatible with factorisation, but the average value of a can be determined and is similar to that in the 1993 analysis. The source of any discrepancy between the two experiments is likely partially to be found in the method of background subtraction and the definition of what constitutes a diffractive event, as well as differences in the range of β covered. ZEUS estimated the value of a obtained using a Monte Carlo model to subtract the background and obtained a substantially lower value. Nevertheless, both ZEUS and H1 agree that the value obtained for α_P is substantially less than would be expected were BFKL dynamics to play an important role. Similarly, both experiments agree that the Pomeron intercept obtained is somewhat larger than that normally obtained by analyses of “soft” hadronic processes.

8.4 ZEUS results from hard photoproduction

We once again slightly enlarge the scope of this review in order to consider some very relevant results on the partonic structure of diffraction from hard photoproduction

[§]Note that some of the results quoted here are smaller than those in the original paper¹⁶⁷ due to a correction to the treatment of the radiative effects.

events. Since the virtual photon in DIS couples only to electrically charged partons, further direct information on gluonic contributions to the Pomeron structure must be obtained by other means. We have already discussed H1's results using a QCD fit to determine the gluon fraction from an examination of the scaling violations with Q^2 . An alternative and more direct probe of the gluon content of the Pomeron can be achieved using a "resolved photon" process, in which a gluon or quark inside the photon may interact with a quark or gluon inside the Pomeron.

A clear signal for diffractive-like events in hard photoproduction can be obtained from a sample of events containing jets in the final state in the range $-1 < \eta^{jet} < 1$ and $E_T^{jet} > 8$ GeV where the most forward going hadron has $\eta_{max} < 1.8$ ¹⁶⁸. A possible contribution from non-diffractive processes to the measured cross-section is both too low and also has the wrong shape in η . In addition, predictions from Monte Carlo models assuming the Pomeron consists of soft gluons or hard quarks fall substantially below the data.

The cross-section was compared to predictions from the POMPYT Monte Carlo using the Donnachie-Landshoff¹⁵³ flux factor and allowing for a mixture of hard gluons and quarks in the Pomeron, together with some non-diffractive background. $\Sigma_{\mathbb{P}}$ is a free parameter in these fits and is defined as the sum of the Pomeron constituents such that if the momentum sum rule is satisfied $\Sigma_{\mathbb{P}} = 1$. If we assume that the Pomeron contains a fraction c_g of gluons, then for each value of c_g a fit can be made to the cross-sections by varying $\Sigma_{\mathbb{P}}$. The results are shown in figure 35. For $c_g = 0$, $\Sigma_{\mathbb{P}} = 2.5 \pm 0.9$, whereas for $c_g = 1$, $\Sigma_{\mathbb{P}} = 0.5 \pm 0.2$.

On the assumption that the parton densities in the pomeron are universal, we can combine the results from the hard photoproduction and ZEUS DIS diffractive data¹⁵⁶. Defining $\Sigma_{\mathbb{P}q}$ as the contribution to $\Sigma_{\mathbb{P}}$ coming from the quarks,

$$\int_{x_{\mathbb{P}min}}^{x_{\mathbb{P}max}} dx_{\mathbb{P}} \int_0^1 d\beta F_2^{D(3)}(\beta, Q^2, x_{\mathbb{P}}) = k_f \cdot \Sigma_{\mathbb{P}q}(Q^2) \cdot I_{flux} \quad (77)$$

where I_{flux} is the integral of the pomeron flux factor over t and k_f is either 5/18 if u, d quarks contribute or 2/9 if u, d, s contribute. Equation 77 can be evaluated using the measured $F_2^{D(3)}$ to give $\Sigma_{\mathbb{P}q} = 0.32 \pm 0.05$ assuming two flavours or 0.40 ± 0.07 for three flavours; this is also plotted in figure 35.

Taking into account the statistical errors, the result for $\Sigma_{\mathbb{P}}$, $0.5 < \Sigma_{\mathbb{P}} < 1.1$, indicates that the data are consistent with the momentum sum rule for the pomeron being satisfied. Taking also into account those systematic errors which do not cancel in this comparison, the data indicate that approximately 1/3 of the momentum of the pomeron is carried by quarks and 2/3 by gluons. Furthermore, the fraction of gluons inside the pomeron can be limited to $0.3 < c_g < 0.8$ at the 1σ level, independent both of the validity of the momentum sum rule and of the definition of the flux factor, provided that it does not depend on Q^2 . Thus there is very satisfactory agreement between H1 and ZEUS, based on very different assumptions, techniques and processes, that the pomeron is predominantly a gluonic object.

Recent results from CDF^{169,170} give the gluon fraction inside the Pomeron as $c_g = 0.7 \pm 0.2$, in good agreement with the ZEUS results. The total number of dijets observed by CDF supports the idea of factorisation breakdown.

8.5 ZEUS results on energetic forward neutrons

Although technically not a diffractive process, the production of leading forward neutrons is also a peripheral process and can also give information on the structure

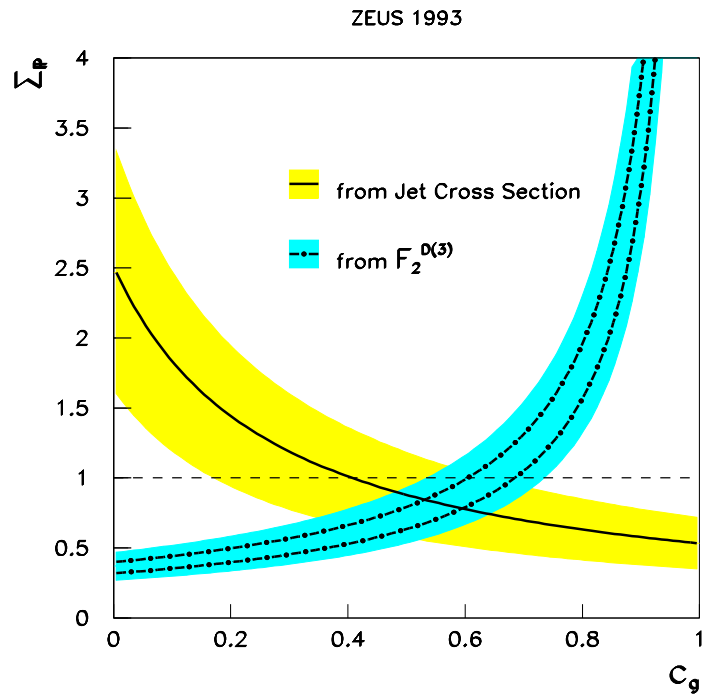


Fig. 35. Σ_{IP} against c_g . The solid line represents the χ^2 minimum and the shaded band the 1σ limits for the fit to the hard photoproduction jet cross-section. The data from the diffractive DIS structure function is represented by the dashed-dotted lines for the two choices of the number of contributing quark flavours and the shaded area is the 1σ error band.

of an exchanged colourless particle, which in this case may be thought of as a charged pion.

Both ZEUS and H1 have over the last few years installed forward neutron calorimeter (FNC) prototypes and latterly final devices. These are small sampling calorimeters situated at 0° from the interaction point and around 100 m downstream. Since the calorimeter is situated downstream of the HERA dipoles, the 820 GeV proton beam is bent upwards away from the FNC and the non-leading charged particles produced at the interaction point are swept away. Neutrons however are not affected by the magnets and leading neutrons interact in the calorimeter to produce a detectable shower. For details of the final ZEUS FNC, see ¹⁷¹.

Events from the 1993 data taking period with signals in a prototype FNC, the so-called FNC-II ¹⁷². The FNC-II has a charged particle veto based on scintillation counters which ensures that the energetic particle entering the calorimeter is neutral. Events having signals from FNC-II thought to correspond to leading neutrons were reconstructed inside the ZEUS detector using the Double Angle method. Those with $Q^2 > 10 \text{ GeV}^2$ and with neutron energies greater than 400 GeV were used in the analysis. The data with leading neutrons have similar distributions in Q^2 , x and W as other DIS events. The ratio of events containing a leading neutron is therefore independent of the kinematic variables and is around $0.45 \pm 0.02 \pm 0.02\%$. While the distribution for large η_{max} seems similar, there seems to be about a factor of two fewer events with a large rapidity gap compared to the average in DIS events. Monte Carlo models such as ARIADNE which do not contain peripheral processes reproduce neither the fraction of events with an energetic neutron nor the neutron energy distribution. However, reasonable agreement with the data is obtained from Monte Carlo models of one pion exchange.

Thus it would seem that the fraction of events containing a leading neutron is independent of the kinematic variables in DIS. There is evidence that one pion exchange is required to explain the general features of the data. This, together with the installation of the final FNCs by ZEUS and H1, promise that future data taking will allow studies of the parton structure of the pion similar to those discussed above for the pomeron.

8.6 Conclusions and outlook for diffraction studies

It is clear that tremendous progress has been made in studies of diffraction since the discovery of large rapidity gap events in DIS at HERA in 1993. ZEUS and H1 agree that there is strong evidence that diffraction is mediated by a colourless particle with the characteristics of the Pomeron. Furthermore, within specific models and with clearly stated assumptions, they agree that the Pomeron has a partonic structure which appears to be predominantly gluonic. It is gratifying to note that these conclusions have been reached with different techniques and differing assumptions. H1 in the preliminary 1994 data analysis has also shown that factorisation is broken and that a reasonable description of the data can be obtained with contributions from non-leading trajectories. Nevertheless, there remains much to be done. The theoretical situation and the basis for many of the assumptions made is still unclear. The availability of high quality experimental data has resulted in an explosion of theoretical work in response to the many open questions in this area.

There are grounds for optimism not only in the greatly increased data sample to be analysed but also in the advent of new and powerful detectors. The larger data sample should open up the study of diffractive events in charged currents, which are now beginning to be seen in the two experiments ¹⁷³. This gives sensitivity in principle to the flavour content of the quarks in the Pomeron. With regard to new detectors, we have already mentioned the forward neutron calorimeters. Both experiments now also have leading proton spectrometers (LPS) either complete or nearing completion ^{174,175}.

Leading proton spectrometers are complex devices consisting of silicon microstrip detectors inside “Roman pots” which can be inserted close to the beam line after injection. By using the HERA magnets as an analysing spectrometer, the trajectories of energetic protons as reconstructed in several stations of “Roman pots” placed downstream of the interaction point can be used to make an accurate measurement of the leading proton momentum. Since the detection of a leading proton is an unambiguous signal for a diffractive interaction, use of the LPS promises in principle the possibility of obtaining an essentially background free sample of diffractive events in DIS.

First preliminary results from the ZEUS LPS are now becoming available. ZEUS has published a study of elastic ρ^0 events with a tagged leading proton¹⁷⁴. The published distributions and properties of these events demonstrate that the LPS can be used and calibrated accurately. In addition preliminary measurements of the t distribution of diffractive events and of the diffractive structure function $F_2^{D(3)}$ ¹⁷⁶ using events tagged with the ZEUS LPS have been presented at conferences. Future publications and improvements in these measurements are to be expected, as well as the prospect for the measurement of the fully differential diffractive structure function, $F_2^{D(4)}$.

A combination of these new detectors, improved knowledge of the current detectors and a large increase in integrated luminosity also opens up the possibility of the measurement of the ratio of the longitudinal to transverse diffractive structure functions, R^D . Since as we have seen, the pomeron seems to be predominantly gluonic, next to leading order QCD necessarily predicts a non-negligible value for R^D . Such a measurement would provide an important testing ground for QCD. Another topic which should become important is the measurement of the charm diffractive cross-section. Both experiments already have indications of charm production in diffractive DIS. A measurement of the charm diffractive structure function would be very important in constraining many of the theoretical models, since the relatively large mass of the c quark provides a hard scale. This can not only allow perturbative calculations in some regions of phase space, but also strongly influence the predictions of the many models which are sensitive to the degree of virtuality of the quarks coupling to the virtual photon. A review of some of the topics in diffraction which can be investigated at HERA in the future can be found in¹⁷⁷. It is clear that the study of diffraction at HERA holds much more excitement in store.

9 High Q^2 processes

9.1 Introduction

HERA provides an unique opportunity to study the electroweak interaction at Q^2 sufficiently high that the charged and neutral currents are of similar strength.

At high Q^2 both charged and neutral current processes can be clearly identified and separated from backgrounds. Neutral current processes can be isolated by identifying the high energy scattered charged lepton, which at high Q^2 tends to be scattered at large angles and therefore into the barrel or forward sections of the calorimeters. In charged current events the fact that the outgoing and undetected ν carries away a large amount of p_T means that above a Q^2 threshold, these events can be cleanly isolated in most regions of phase space.

In section 3.3 we discussed the general form of the differential cross-section for deep inelastic scattering. Equation 13 shows the general form for the differential cross-section in terms of the structure functions F_1 , F_2 and F_3 . These structure functions are products of quark distribution functions and the couplings of the currents mediating the interaction, as discussed in detail in section 3.3.

9.2 Experimental results

As remarked earlier, the identification of both neutral and charged current events at high Q^2 is relatively straight-forward. H1 base their analysis and event selection of the kinematic variables reconstructed from the energy of the hadronic final state; the presence or absence of an electron is used only to classify an event as either a charged or a neutral current candidate. The requirement of transverse momentum from the hadronic jet of greater than 25 GeV, together with vertex and trigger selections, leads to a clean sample of high Q^2 events with little background and an efficiency of $\sim 85\%$ ¹⁷⁸. ZEUS in contrast select charged current candidates by selecting on missing transverse momentum greater than 11 GeV. Similar vertex and trigger cuts are made as for H1, although ZEUS uses a rather more complicated set of cuts to reduce backgrounds from neutral current and photoproduction events. Both experiments use a combination of pattern recognition algorithms and visual scanning to remove remaining cosmic ray interactions in the detectors.

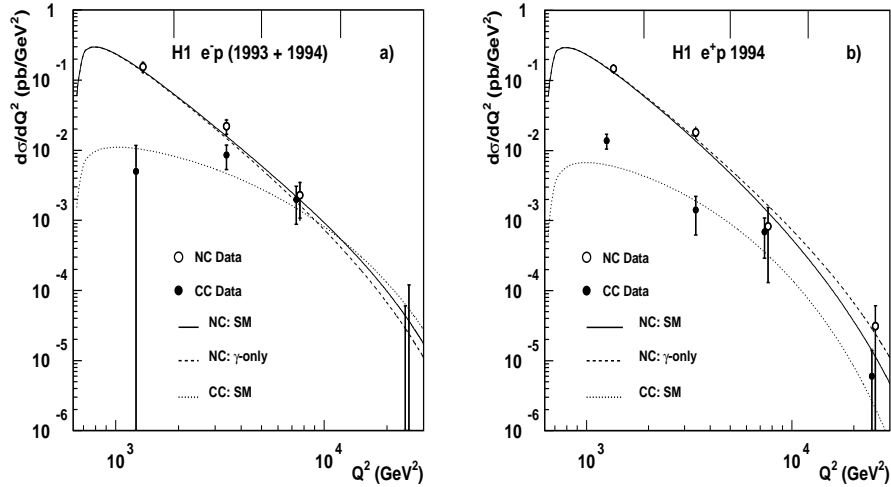


Fig. 36. Neutral current and charged current e^-p and e^+p cross-sections as a function of Q^2 from the H1 1993 and 1994 data. The boundaries of each bin are denoted by the vertical lines at the top of the plot. The solid curve shows the Standard Model prediction for neutral currents, the dashed-dotted curve the neutral current cross-section without the Z contribution and the dashed curve the Standard Model prediction for charged currents.

Figure 36 shows the differential cross-section for the charged and neutral currents as a function of Q^2 from the H1 experiment ¹⁷⁸, while figure 37 shows the ZEUS differential cross-section as a function of x . It can be seen that, for e^-p interactions, these two processes become of equal strength at $Q^2 \sim 10^4$ GeV². For e^+p interactions, the charged current cross-section approaches the neutral current cross-section, but remains below it. The reason for the smaller size of the e^+p cross-section compared to e^-p can be seen by inspection of equations 13, 29 and 30. Since at high Q^2 both $x, y \rightarrow 1$, the $(1-y)^2$ terms in the cross-section, which arise from the $V-A$ helicity structure of the charged weak current, imply that quarks dominate the cross-section in the case of electrons and sea antiquarks in the case of positrons. Since the density of sea quarks tends to 0 as $x \rightarrow 1$, the ratio of positron to electron cross-sections will fall to 0. This behaviour is shown in

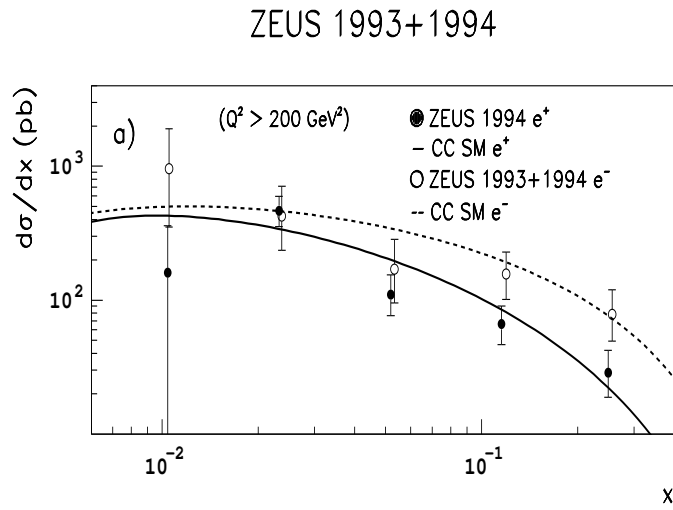


Fig. 37. Neutral current and charged current cross-sections as a function of x from the ZEUS 1993 and 1994 data. The data points are centred at the generator level average x of the points in that bin. The solid curve shows the Standard Model prediction for neutral currents and the dashed curve the Standard Model prediction for charged currents.

figure 38, which shows data on the ratio of the positron and electron cross-sections as a function of Q^2 from the ZEUS 1993 data¹⁷⁹. The ratio for neutral currents

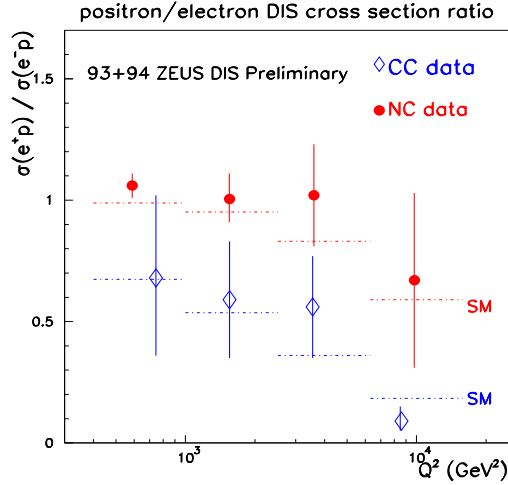


Fig. 38. Ratio of positron and electron total cross-sections as a function of Q^2 from ZEUS 1993 and 1994 data. The dotted lines show the Standard Model predictions.

also falls as Q^2 increases, again for reasons related to the current-quark coupling at high y , although the more complicated nature of the formula for the neutral current cross-section means that this is not as obvious as in the charged current case.

The fact that the charged current data are in good agreement with the Standard Model clearly excludes an infinite mass W and allows in principle a determination of the W mass. Both ZEUS and H1 have carried out such a determination. H1 uses the individual event characteristics to construct a likelihood function which is compared with the hypothesis of a varying W mass. ZEUS performs a maximum likelihood fit to the binned differential cross-section data. H1 obtains $M_W = 84^{+9}_{-6} +5_{-4}$ GeV, while ZEUS obtains $M_W = 79^{+8}_{-7} +4_{-4}$ GeV. Both of these results are in good agreement with the world average of 80.22 ± 0.26 ¹³⁷. It will clearly be some time before the mass determined in the space-like domain will approach the accuracy of the Tevatron and LEP-II in the time-like domain!

9.3 The highest attainable x, Q^2

Although we have seen in the previous section that the data taken up to 1994 showed excellent agreement with the Standard Model, the data taken in 1995 and 1996 represented an increase in luminosity of approximately a factor of 10. The analysis of this data by the two collaborations began to show very interesting possible discrepancies from the predictions of the Standard Model at the highest attainable Q^2 and x .

The data sample used by ZEUS¹⁸⁰ corresponds to 20.1 pb^{-1} , while H1¹⁸¹ uses 14.2 pb^{-1} . H1 uses a variety of methods to reconstruct the kinematic variables for neutral current events, preferring the Electron method and using the Double Angle method as a check. ZEUS prefers the DA method and uses the Electron method as

a check. In contrast to ZEUS, H1 also presents results for charged currents; ZEUS charged current data have now been presented at conferences¹⁸².

The cause of the excitement can be seen when the data are plotted as a function of x (or equivalently $M_e = \sqrt{sx}$) or Q^2 and compared with the predictions of the Standard Model. Figure 39 and figure 40 show the distributions of events as a function of $x(M_e)$, while figure 41 and figure 42 show the distributions as a function of Q^2 . Both experiments show significant deviations from the expectations of the Standard Model, shown as a solid line, in both $x(M_e)$ and Q^2 .

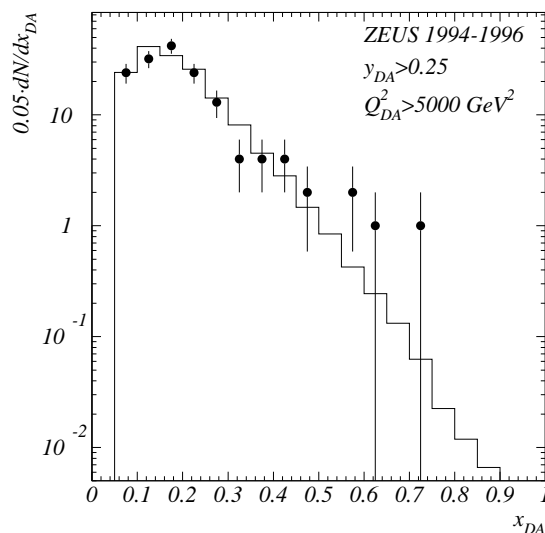


Fig. 39. The x_{DA} distribution of the observed events from ZEUS for the cuts in y and Q^2 indicated. The Standard Model prediction is shown as the histogram. The error bars correspond to the square root of the number of events in the bin.

H1 also see a small excess of 4 events compared to an expectation of 1.8 ± 0.9 for the region beyond $Q^2 = 15000 \text{ GeV}^2$ in the charged current sample. ZEUS also report a small excess, though in neither case is this excess very statistically significant.

Of course the most natural interpretation of this signal, given the amazing resilience of the Standard Model over the past 30 years, is either an instrumental or background effect, possible freedom to vary the assumed parameters of the Standard Model fits, or a statistical fluctuation. Both experiments have carried out a thorough check for possible backgrounds and systematic effects, as well as investigating the uncertainty in the predictions of the Standard Model at these thus far unattainably high values of Q^2 . Both experiments find essentially zero backgrounds from any known Standard Model processes. Neither could any systematic effects which could promote events from low to high Q^2 be identified.

Although there is some uncertainty from variations in parton distributions, α_s etc., the maximum effect which can be produced by varying the conventional parton distributions, of about 7 - 8%, is much too small to explain the effect. However, Kuhlmann et al.¹⁸³, have recently suggested that the effect could be explained

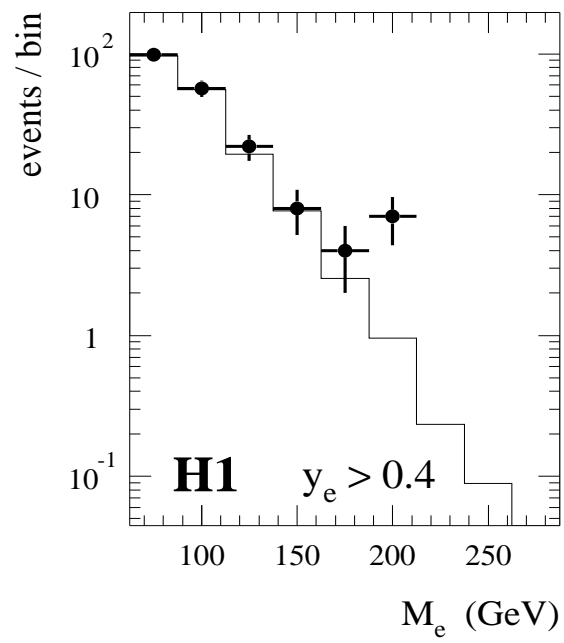


Fig. 40. Distribution of M_e for the observed events from H1 for $y_e > 0.4$. The error bars correspond to the statistical error in the bin.

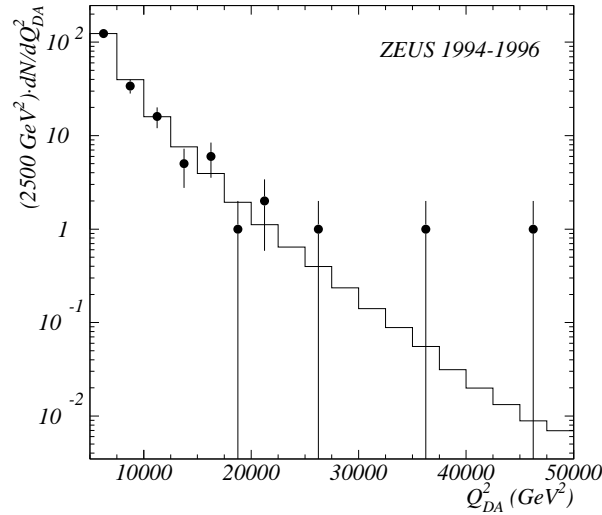


Fig. 41. The Q^2 distribution of the observed events from ZEUS. The Standard Model prediction is shown as the histogram. The error bars correspond to the square root of the number of events in the bin.

without recourse to physics beyond the Standard Model by the addition of a small admixture of valence quark at very high x , beyond the region well-measured by fixed target experiments. This could also explain the excess observed in the jet cross-section at high E_t by the CDF collaboration¹⁸⁴, although this can also be explained rather more plausibly by an increase in the poorly determined high x gluon distribution¹⁸⁵. It is pointed out by Kuhlman *et al.* that such an admixture would actually *improve* the global fit to DIS data since there is a small excess in the BCDMS data compared to the QCD fits beyond x of 0.75. The admixture at high x could also be an intrinsic charm or bottom contribution. However, given that there is no longer any experimental motivation for intrinsic charm, to introduce it in this case would seem somewhat bizarre. Furthermore, although the addition of a small valence contribution at high x would certainly not require physics beyond the Standard Model, such behaviour in hitherto well-behaved parton distributions seems scarcely less exotic.

The final possibility not involving physics beyond the Standard Model is that the signal is a statistical fluctuation. Both experiments have done a very careful evaluation of the probability of the effect which is seen in its data arising by chance. ZEUS states that this probability is 0.72% for $x > 0.55$ and $y > 0.25$, while H1 consider the probability to be 0.6%. Both observations are therefore rather unlikely to occur by chance. Furthermore, had these been fluctuations, they could have occurred anywhere in available phase space, rather than at the edge of phase space in a region hitherto unexplored.

In the above experimental situation, it certainly seems reasonable to consider possible explanations for these effects in physics beyond the Standard Model. There are a variety of possible explanations for this effect. The publication of this data have lead to a veritable explosion of theoretical papers speculating on its origin;

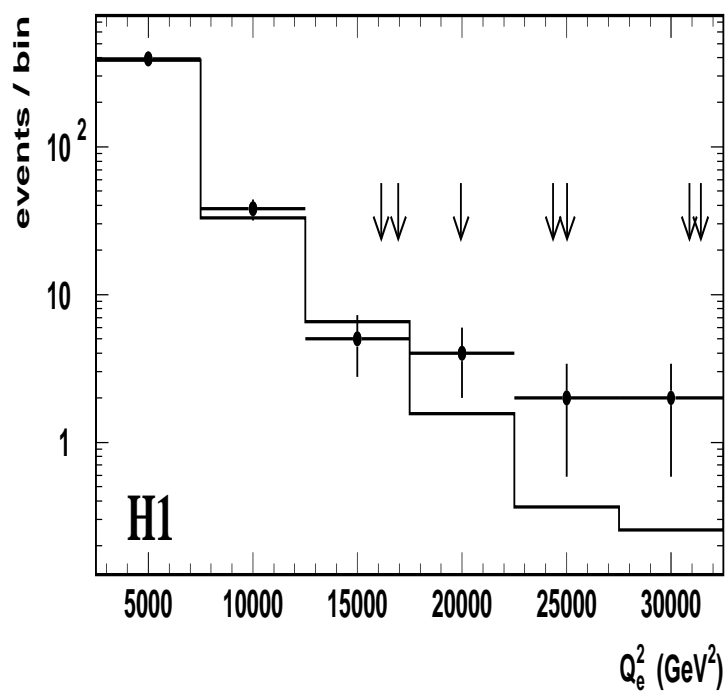


Fig. 42. Distribution of Q_e^2 for the observed events from H1. The error bars correspond to the statistical error in the bin. The arrows indicate the Q_e^2 values for those events with $Q_e^2 > 15000$ GeV 2 and $M_e > 180$ GeV.

for example one of the most comprehensive is that by Altarelli *et al.*¹⁸⁶. Here we mention the possibilities only briefly.

One possibility is an s channel quark-lepton bound state, or resonance, which we can refer to generically as a “leptoquark”, although it could be one of several varieties of scalar or vector leptoquarks, or a supersymmetric R -parity violating squark. H1’s data is presented in the variables y and M_e , suggesting an explanation in terms of the production of such a particle. In contrast ZEUS works with Q^2 and x . If the ZEUS data are expressed in terms of the H1 variables, some sort of consistency check is possible. The mean value of M_e in the H1 data is approximately $200 \pm 2 \pm 6$ GeV, where the first error corresponds to statistical and the second to a systematic effect due to the energy scale uncertainty. Using the preferred Double Angle reconstruction for ZEUS, \overline{M}_{DA} is approximately 233 ± 6 GeV, where the error contains both statistical and systematic errors. At first glance these data differ by more than three standard deviations. However, some words of caution are in order here; a Gaussian error in the contribution of the uncertainty of the calorimeter energy scale to the overall systematic error of the H1 data is scarcely justified, since their Monte Carlo studies show significant non-Gaussian tails (see figure 2d in¹⁸¹). ZEUS uses more conservative RMS’s. In addition, the overall χ^2 between the x_{DA} and x_e calculations for ZEUS is not particularly good, implying the possibility that some additional systematic error is playing a role. The actual discrepancy could therefore be somewhat less. It is also true that possible initial state radiation of hard photons, which affects the Electron and Double Angle determinations differently, could substantially improve the compatibility of the data.

Several papers have discussed the compatibility of the ZEUS and H1 data (see for example¹⁸⁷). Although the analysis of Drees as to the compatibility of the ZEUS and H1 mass values is interesting, he does not consider the instrumental effects referred to above, nor the fact that ZEUS prefer to use DA variables for good reasons related to their understanding of their detector. However, Drees is certainly correct to point out that the number of events seen in H1 compared to ZEUS seems different what would be expected from the production of an s -channel resonance given the efficiencies and luminosities of the two experiments. This can only reasonably be ascribed to a statistical fluctuation. Whereas it would seem premature to rule out the hypothesis that the signals seen in the two experiments are compatible, there is clearly doubt on our ability to multiply the probabilities they quote for their compatibility with the Standard Model. Thus it would clearly be premature to assume that the Standard Model is excluded at the 99.99% confidence level!

Should the discrepancy between ZEUS and H1 turn out to be real, the explanation for the effect would then be unlikely to be an s -channel resonance. Some sort of contact interaction, implying quark and/or lepton substructure, could be possible. Such an effect would lead to an apparent excess in Q^2 rather similar to the excess of large angle scatters observed by Rutherford when he resolved the atomic nucleus, and corresponding in this case to the resolution of substructure. Since there would be no x or equivalently M structure in such a case, the data of both experiments would be compatible, with the apparent clustering of the H1 data ascribed to a fluctuation.

Whether any of the above explanations is correct, or whether the simple and disappointing possibility of an unlikely statistical fluctuation is the source of this interesting anomaly, must await the collection of more data over the next few years.

10 Future outlook and conclusions

HERA physics is poised at a fascinating stage. The “high cross-section” physics of low x DIS and photoproduction has proved to be much more interesting than had

been anticipated when HERA was proposed. The steep rise in the gluon distribution inside the proton has been a catalyst to a great deal of theoretical work on the detailed properties of QCD. Nevertheless, as yet, no “smoking gun” for BFKL behaviour has been observed. The study of exclusive vector meson production in DIS and the first observation of charm production in DIS has also opened up the possibility of further tying down the gluon distribution. A whole new field of study of the deep inelastic structure of diffraction has been opened up by HERA. This study has already produced much of interest and has the promise of truly revolutionising our understanding of the mechanism of diffraction. Finally, the data at high Q^2 and x are allowing detailed tests of the charged and neutral weak current, and at the edge of the kinematic region currently accessible there are indications of an excess of events which could indicate new physics.

With such a wealth of interesting results it is easy to forget that the high Q^2 and x physics for which HERA was built has scarcely begun to be explored. The recent workshop on future physics at HERA has given an excellent overview of the detailed topics which HERA will be able to investigate over the next few years¹⁸⁸. The potential of HERA will be greatly increased by the proposed luminosity upgrade; it is also likely that the energy of the proton beam will be increased to at least 900 GeV. The changes in the machine configuration which are required to increase the luminosity will have consequences on the experiments, effectively excluding the study of low Q^2 physics and introducing significant complications in the operation of detectors such as the leading proton spectrometers. It is particularly important therefore in the next few years to collect sufficient data with these unique detectors properly to exploit their physics potential. The prospect of easy use of both electrons and positrons and the existence of polarisation opens up the promise of detailed studies of the structure of the weak current in an analogous way to the detailed studies of the strong interaction which are currently being carried out. There is clearly a tremendous interest in pushing back the kinematic limit to as high values of Q^2 as possible. Even if the current indications of possible new physics were not to persist with further luminosity, the potential of the future HERA programme is very great. If the high Q^2 - x anomalies were to be confirmed, then it is difficult to overestimate the interest that physics at HERA would hold over the next few years.

Acknowledgements

I am grateful to my colleagues on ZEUS and H1 for many useful conversations. I am particularly grateful to M. Lancaster, J.D. McFall and A. Quadt for carefully reading and commenting on the manuscript, and to J.D. McFall and R. Hall-Wilton for help with the figures.

References

1. H1 Collaboration, I. Abt *et al.*, DESY H1-96-01 (1996).
2. The ZEUS Detector Status Report (DESY 1993).
3. H1 Collaboration, DESY Internal Report PRC 92/01; J. Bürger *et al.*, DESY 96-200, and references therein.
4. J. Bürger *et al.*, Nucl. Instr. and Meth., A279 (1989) 217.
5. G.A. Beck *et al.*, Nucl. Instr. and Meth., A283 (1989) 471;
J.M. Bailey *et al.*, Nucl. Instr. and Meth., A323 (1992) 184;
H. Grässler *et al.*, Nucl. Instr. and Meth., A323 (1992) 401, and references therein.
6. B. Andrieu *et al.*, Nucl. Instr. and Meth., A336 (1993) 460.
7. H1 Collaboration, DESY 96-171.
8. C. Alvisi *et al.*, Nucl. Instr. and Meth., A305 (1991) 30.
9. ZEUS Collaboration, DESY Internal Report PRC 97/01.
10. B. Foster *et al.*, Nucl. Instr. and Meth., A338 (1994) 254.
11. N. Harnew *et al.*, Nucl. Instr. and Meth., A279 (1989) 290;
B. Foster *et al.*, Nucl. Phys. B (Proc. Suppl.) 32 (1993) 181;
B. Foster *et al.*, Nucl. Instr. and Meth., A338 (1994) 254.
12. A. Andresen *et al.*, Nucl. Instr. and Meth., A305 (1991) 101; A. Bernstein *et al.*, Nucl. Instr. and Meth., A336 (1993) 23.
13. R.K. Ellis, W.J. Sterling and B.R. Webber, "QCD and Collider Physics", Cambridge, ISBN 521 58189 3, (1996).
14. V.N. Gribov and L.N. Lipatov, Sov. J. Nucl. Phys. 15 (1972) 438, 675; L.N. Lipatov, Sov. J. Nucl. Phys. 20 (1975) 94; Yu. L. Dokshitzer, Sov. Phys. JETP 46 (1977) 641; G. Altarelli and G. Parisi, Nucl. Phys. B126 (1977) 298.
15. E.A. Kuraev, L.N. Lipatov, and V.S. Fadin, Sov. Phys. JETP 45 (1977) 199; Y.Y. Balitsky and L.N. Lipatov, Sov. J. Nucl. Phys. 28 (1978) 822.
16. C.G. Callen and D.J. Gross, Phys. Rev. Lett. 22 (1969) 156.
17. G. Altarelli, R.K. Ellis and G. Martinelli, Nucl. Phys. B143 (1978) 521, and Nucl. Phys. B146 (1978) 544 (erratum).
18. G. t'Hooft and M. Veltman, Nucl. Phys. B44 (1972) 189;
G. t'Hooft, Nucl. Phys. B61 (1973) 455;
W.A. Bardeen *et al.*, Phys. Rev D18 (1978) 3998.
19. See for example D. Bardin *et al.*, Proceedings of the Workshop on Future Physics at HERA, Volume 1 (1996) 13, and references therein.
20. F. Jacquet and A. Blondel, Proceedings Study of an *ep* facility in Europe, ed. U. Amaldi, DESY 79-48 (1979).
21. S. Bentvelsen, J. Engelen, and P. Kooijman, Proceedings of the Workshop on Physics at HERA, DESY (1992) 23.
22. U. Bassler and G. Bernardi, Nucl. Instr. and Meth., A361 (1995) 197.
23. ZEUS Collaboration, M. Derrick *et al.*, Z. Phys. C72 (1996) 399.
24. H1 Collaboration, T. Ahmed *et al.*, Nucl. Phys. B439 (1995) 471.
25. ZEUS Collaboration, M. Derrick *et al.*, Z. Phys. C65 (1995) 379.
26. M. Glück, E. Reya and A. Vogt, Z. Phys. C53 (1992) 127; Phys. Lett B306 (1993) 391; DESY-94-206 (1994).
27. A.D. Martin, R.G. Roberts and W.J. Stirling, Phys. Rev. D50 (1994) 6734.
28. H1 Collaboration, S. Aid *et al.*, Nucl. Phys. B470 (1996) 3.
29. ZEUS Collaboration, M. Derrick *et al.*, Z. Phys. C72 (1996) 399.

30. BCDMS Collaboration, A.C. Benvenuti *et al.*, Phys. Lett. B223 (1989) 485.
31. NMC Collaboration, M. Arneodo *et al.*, Phys. Lett. B364 (1995) 107; Nucl. Phys. B483 (1997) 3.
32. E665 Collaboration, M.R. Adams *et al.*, Phys. Rev. D54 (1996) 3006..
33. H1 Collaboration, C. Adloff *et al.*, DESY 97-042 (1997).
34. ZEUS Collaboration, J. Breitweg *et al.*, DESY 97-135 (1997).
35. A. Donnachie and P.V. Landshoff, Z. Phys. C61 (1994) 139.
36. A. Capella *et al.*, Phys. Lett. B337 (1994) 358.
37. B. Badelek and J. Kwiecinski, Phys. Lett. B295 (1992) 263.
38. M. Glück, E. Reya and A. Vogt, Z. Phys. C67 (1995) 433; As shown by A. Vogt, in Proceedings of Workshop on Deep Inelastic Scattering and QCD, Paris (1995) 261.
39. K. Adel, F. Barreiro and F.J. Yndurain, Nucl. Phys. B495 (1997) 221.
40. A. De Rújula *et al.*, Phys. Rev. D10 (1974) 1649.
41. L.V. Gribov, E.M. Levin and M.G. Ryskin, Phys. Rep 100 (1983) 1; A.H. Mueller and N. Quiu, Nucl. Phys. B268 (1986) 427
42. M. Ciafaloni, Nucl. Phys. B296 (1988) 49; S. Catani, F. Fiorani and G. Marchesini, Phys. Lett. B234 (1990) 339; Nucl. Phys. B336 (1990) 18.
43. J. Kwiecinski, A.D. Martin and P.J. Sutton, Phys. Rev. D52 (1995) 1445.
44. A.D. Martin, W.J. Stirling and R.G. Roberts, Phys. Lett. B306 (1993) 145; Phys. Lett. B309 (1993) 492 (erratum).
45. CTEQ Collab., H.L. Lai *et al.*, Phys. Rev. D51 (1995) 4763.
46. M. Glück, E. Reya and A. Vogt, Z. Phys. C48 (1990) 471; Nucl. Phys. B (Proc. Suppl.) 18C (1990) 49.
47. S.K. Brodsky and I. Schmidt, Phys. Lett. B234 (1990) 144.
48. M. Glück, E. Reya and A. Vogt, Z. Phys. C53 (1992) 127.
49. ZEUS Collaboration, M. Derrick *et al.*, Z. Phys. C63 (1994) 391.
50. H1 Collaboration, S. Aid *et al.*, Z. Phys. C69 (1995) 27.
51. M. Glück, E. Reya and A. Vogt, Z. Phys. C67 (1995) 433;
52. ZEUS Collaboration, J. Tickner, private communication.
53. D. Schildknecht and H. Spiesberger, hep-ph/9707447.
54. J.J. Sakurai and D. Schildknecht, Phys. Lett. B40 (1972) 121; B. Gorcezyca and D. Schildknecht, Phys. Lett. B47 (1973) 71.
55. R.D. Ball and S. Forte, Phys. Lett B335 (1994) 77.
56. C. López and F.J. Ynduráin, Nucl. Phys. B171 (1980) 231.
57. R.K. Ellis, Z. Kunszt and E.M. Levin, Nucl. Phys. B420 (1994) 517.
58. R.K. Ellis, F. Hautmann and B.R. Webber, Phys. Lett B348 (1995) 582.
59. J.R. Forshaw, R.G. Roberts, and R.S. Thorne, Phys. Lett. B356 (1995) 79.
60. A.J. Askew, J. Kwiecinski, A.D. Martin and P.J. Sutton, Phys. Rev. D47 (1993) 3775; Phys. Rev. D49 (1994) 4402.
61. R. Thorne, Phys. Lett. B392 (1997) 463; hep-ph/9701241
62. S. Catani, hep-ph/9609263, and Proceedings of DIS'96, Roma, ed. G. D'Agostini and A. Nigro, World Scientific (1997) 165.
63. H1 Collaboration, S. Aid *et al.*, Phys. Lett. B354 (1995) 494.
64. L. Bauerdick, A. Glazov and M. Klein, Proceedings of the Workshop on Future Physics at HERA, Volume 1 (1996) 77.
65. See for example A. Frey, Ph.D. Thesis, University of Bonn (1996) (unpublished); A. Cassidy, Ph.D. Thesis, University of Bristol (1997) (unpublished).
66. H1 Collaboration, S. Aid *et al.*, Phys. Lett. 393B (1997) 452.
67. ZEUS Collaboration, M. Derrick *et al.*, Phys. Lett. B345 (1995) 576.
68. NMC Collaboration, M. Arneodo *et al.*, Phys. Lett. B309 (1993) 222.

69. M. Glück, E. Hoffmann and E. Reya, *Z. Phys.* C13 (1982) 119.
70. M. Glück, E. Reya and M. Stratmann, *Nucl. Phys.* B422 (1994) 37.
71. E. Laenen *et al.*, *Nucl. Phys.* B392 (1993) 162, 229;
E. Laenen *et al.*, *Phys. Lett.* B291 (1992) 325;
S.Riemersma *et al.*, *Phys. Lett.* B347 (1995) 143.
72. W.J. Marciano, *Phys. Rev.* D29 (1984) 580.
73. A. D. Martin, R. G. Roberts and W. J. Stirling, *Phys. Lett.* B354 (1995) 155
74. K. Prytz, *Phys. Lett.* B332 (1994) 393.
75. R.D. Ball and S. Forte, hep-ph/9607289, and Proceedings of DIS'96, Roma, ed. G. D'Agostini and A. Nigro, World Scientific (1997) 208.
76. NMC Collaboration, D. Allasia *et al.*, *Phys. Lett.* B258 (1991) 493.
77. H1 Collaboration, S. Aid *et al.*, *Nucl. Phys.* B449 (1995) 3.
78. E. Mirkes and D. Zeppenfeld, *Acta Phys. Polon.* B27 (1996) 1393;
Proceedings of the Zeuthen Workshop on Elementary Particle Theory, "QCD and QED in Higher Orders", Rheinsberg, Germany, April 1996; presented by E. Mirkes, *Nucl. Phys. (Proc. Suppl.)* 51C (1996) 273.
79. M.G. Ryskin, *Z. Phys.* C57 (1993) 89.
80. S.J. Brodsky *et al.*, *Phys. Rev.* D50 (1994) 3134.
81. ZEUS Collab., M. Derrick *et al.*, *Z. Phys.* C69 (1995) 39.
82. H1 Collaboration, S. Aid *et al.*, *Nucl. Phys.* B468 (1996) 3.
83. A. Donnachie and P.V. Landshoff, *Phys. Lett.* B185 (1987) 403.
84. NMC Collab., P. Amaudruz *et al.*, *Z. Phys.* C54 (1992) 239;
M. Arneodo *et al.*, *Nucl. Phys.* B429 (1994) 503.
85. H1 Collaboration, S. Aid *et al.*, *Nucl. Phys.* B472 (1996) 3.
86. ZEUS Collab., M. Derrick *et al.*, *Phys. Lett.* B350 (1995) 120-134.
87. A. Donnachie and P.V. Landshoff, *Phys. Lett.* B348 (1995) 213.
88. ZEUS Collab., J. Breitweg *et al.*, *Z. Phys.* C75 (1997) 215.
89. FTPS Collaboration, B.H. Denby *et al.*, *Phys. Rev. Lett.* 52 (1984) 795.
90. E401 Collaboration, M. Binklet *et al.*, *Phys. Rev. Lett.* 48 (1982) 73.
91. E687 Collaboration, P.L. Frabetti *et al.*, *Phys. Lett.* B316 (1993) 197.
92. ZEUS Collab., M. Derrick *et al.*, DESY 97-147 (1997) and hep-ex/9708010.
93. NA14 Collaboration, R. Barate *et al.*, *Z. Phys.* C33 (1987) 505.
94. EMC Collaboration, J. Ashman *et al.*, *Z. Phys.* C56 (1992) 21.
95. M. Cacciari and M. Krämer, *Phys. Rev. Lett.* 52 (1996) 4128.
96. CDF Collaboration, F. Abe *et al.*, *Phys. Rev. Lett.* 69 (1992) 3704;
CDF Collaboration, A. Sansomi, FERMILAB-CONF-95/263-E.
97. M. Krämer *et al.*, *Phys. Lett.* B348 (1995) 657;
M. Krämer, *Nucl. Phys.* B459 (1996) 3.
98. L. Frankfurt, W. Köpf and M. Strikman, *Phys. Rev.* D54 (1996) 3194;
see also: H. Abramowicz, L. Frankfurt and M. Strikman, DESY-95-047, hep-ph/9503437 (1995);
L. Frankfurt and M. Strikman, hep-ph/9510291 (1995).
99. G. Feldman *et al.*, *Phys. Rev. Lett.* 38 (1977) 1313.
100. ZEUS Collaboration, J. Breitweg *et al.*, *Phys. Lett.* B401 (1997) 192.
101. H1 Collaboration, S. Aid *et al.*, *Nucl. Phys.* B472 (1996) 32.
102. CIF Collab., M.S. Atiya *et al.*, *Phys. Rev. Lett.* 43 (1979) 414;
BFP Collab., A.R. Clark *et al.*, *Phys. Rev. Lett.* 45 (1980) 682;
SLAC HFP Collab., K. Abe *et al.*, *Phys. Rev.* D30 (1984) 1;
EMC Collab., M. Arneodo *et al.*, *Z. Phys.* C35 (1987) 1;
PEC Collab., M. Adamovich *et al.*, *Phys. Lett.* B187 (1987) 437;
E691 Collab., J.C. Anjos *et al.*, *Phys. Rev. Lett.* 65 (1990) 2503;

- NA-14' Collab., M.P. Alvarez *et al.*, Z. Phys. C60 (1993) 53.
103. S. Frixione *et al.*, Phys. Lett B348 (1995) 633;
Nucl. Phys. B454 (1995) 3.
104. M. Glück, E. Reya and A. Vogt, Phys. Lett. B306 (1993) 391.
105. ZEUS Collaboration, J. Breitweg *et al.*, DESY 97-089 (1997).
106. H1 Collaboration, C. Adloff *et al.*, Z. Phys. C72(1996) 593.
107. H. Abramowicz, K. Charchula and A. Levy, Phys. Lett. B269 (1991) 458.
108. E. Laenen *et al.*, Nucl. Phys. B392 (1993) 162;
Nucl. Phys. B393 (1993) 229; Phys. Lett. B291 (1992) 325.
109. S. Riemersma, J. Smith and W.L. van Neerven, Phys. Lett. B347 (1995) 143.
110. EMC Collaboration, J.J. Aubert *et al.*, Nucl. Phys. B213 (1983) 31.
111. H1 Collaboration, I. Abt *et al.*, Z. Phys. C63 (1994) 377.
112. ZEUS Collaboration, M. Derrick *et al.*, Z. Phys. C70 (1996) 1.
113. DELPHI Collab., P. Abreu *et al.*, Phys. Lett. B311 (1993) 408.
114. H1 Collaboration, S. Aid *et al.*, Z. Phys. C72 (1996) 573.
115. Z. Koba, H.B. Nielsen and P. Olesen, Nucl. Phys. B40 (1972) 317.
116. G. Ingelman, Proceedings of the Workshop on Physics at HERA, DESY Vol. 3 (1992) 1366;
M. Bengtsson, G. Ingelman, T. Sjöstrand, Nucl. Phys. B301 (1988) 554.
117. T. Sjöstrand, Comp. Phys. Comm. 39 (1986) 347;
T. Sjöstrand and M. Bengtsson, *ibid.* 43 (1987) 367.
118. EMC Collaboration, M. Arneodo *et al.*, Z. Phys. C35 (1986) 417.
119. E665 Collaboration, M.R. Adams *et al.*, FNAL-Pub 93/245-E (1993);
Phys. Lett. B272 (1991) 163.
120. EMC Collab., J. Ashman *et al.*, Z. Phys. C52 (1991) 361.
121. E665 Collab., M.R. Adams *et al.*, Phys. Lett. B272 (1991) 163.
122. H1 Collaboration, C. Adloff *et al.*, Nucl. Phys. B485 (1997) 3.
123. G. Marchesini *et al.*, Comp. Phys. Comm. 67 (1992) 465;
M. Seymour, Lund preprint LU-TP-94-12 (1994) and Nucl. Phys. B436 (1995) 443;
B.R. Webber, Nucl. Phys. B238 (1984) 492.
124. ZEUS Collaboration, M. Derrick *et al.*, Z. Phys. C67 (1995) 93.
125. H1 Collaboration, S. Aid *et al.*, Nucl. Phys. B445 (1995) 3.
126. H1 Collaboration, C. Adloff *et al.*, DESY 97-108 (1997).
127. Yu.L. Dokshitzer *et al.*, "Basics of Perturbative QCD", Editions Frontières (1991);
Ya.I. Azimov *et al.*, Z. Phys. C31 (1986) 213; Z. Phys. C27 (1985) 65;
Yu.L. Dokshitzer, V.A. Khoze and S.I. Troyan, Phys. Lett. 202B (1988) 276.
128. TASSO Collaboration, W. Braunschweig *et al.*, Z. Phys. 47 (1990) 187; Phys. Lett. B311 (1993) 408;
DELPHI Collaboration, P. Abreu *et al.*, Phys. Lett B311 (1993) 408;
OPAL Collaboration, G. Alexander *et al.*, Z. Phys. C72 (1996) 191; K.Z. Akrawy *et al.*, Phys. Lett. B247 (1990) 617.
ALEPH Collaboration, R. Barate *et al.*, CERN PPE 96-186.
129. H1 Collaboration, S. Aid *et al.*, Nucl. Phys. B480 (1996) 3.
130. ZEUS Collaboration, M. Derrick *et al.*, Z. Phys. C68 (1995) 29.
131. DELPHI Collab., P. Abreu *et al.*, Z. Phys. C65 (1995) 587
132. E665 Collab., M.R. Adams *et al.*, Z. Phys. C61 (1994) 539
133. A. Ringwald and F. Schremmp, DESY 94-147;
M.J. Gibbs, A. Ringwald and F. Schremmp, DESY 95-119;
M.J. Gibbs, A. Ringwald, B.R. Webber and J.T. Zadrozny, Z. Phys. C66 (1995) 285.
134. H1 Collaboration, T. Ahmed *et al.*, Phys. Lett. B346 (1995) 415.
135. ZEUS Collaboration, M. Derrick *et al.*, Phys. Lett. B363 (1995) 201.

136. JADE Collab., W. Bartel *et al.*, Z. Phys. C33, (1986) 23;
137. Particle Data Group, R.M. Barnett *et al.*, Phys. Rev. D54, (1996) 1.
138. H1 Collaboration, S. Aid *et al.*, Z. Phys. C63 (1994) 377.
139. ZEUS Collaboration, paper 0391, submitted paper to EPS Conference, Brussels, July 1995.
140. H1 Collaboration, pa02-073, submitted paper to ICHEP'96, Warsaw Poland, July 1996.
141. H1 Collaboration, S. Aid *et al.*, Phys. Lett. B356 (1995) 118
142. H1 Collaboration, pa03-049, submitted paper to ICHEP'96, Warsaw Poland, July 1996.
143. J. Bartels *et al.*, Phys. Lett. B384 (1996) 300.
144. K. Goulianos, Phys. Rep. 101 (1983) 169.
145. UA8 Collaboration, A. Brandt *et al.*, Phys. Lett. B297 (1992) 417;
R. Bonino *et al.*, Phys. Lett. B211 (1988) 239.
146. D0 Collaboration, S. Abachi *et al.*, Phys. Rev. Lett. 72 (1994) 2332.
147. CDF Collaboration, F. Abe *et al.*, Phys. Rev. Lett. 74 (1995) 855.
148. ZEUS Collaboration., M. Derrick *et al.*, Phys. Lett. B315 (1993) 481.
149. H1 Collaboration, T. Ahmed *et al.*, Nucl. Phys. B429 (1994) 477.
150. R.P. Feynman, "Photon-Hadron Interactions", p 344, Benjamin (1972).
151. J.D. Bjorken, Proceedings of International Workshop on Deep Inelastic Scattering, Eilat, Israel, 1994, ed. A. Levy, World Scientific (1995) 144.
152. V. Del Duca, hep-ph/9506355 in Proceedings of the 10th Topical Workshop on Proton-Antiproton Collider Physics, Fermilab, Batavia, Illinois, May 9-13, 1995.
153. A. Donnachie and P.V. Landshoff, Nucl. Phys. B244 (1984) 322; Phys. Lett. B191 (1987) 309; Nucl. Phys. B303 (1988) 634; Phys. Lett. B285 (1992) 172.
154. G. Ingelman and P. Schlein, Phys. Lett. 152B (1985) 256.
155. H1 Collaboration, T. Ahmed *et al.*, Phys. Lett. B348 (1995) 681.
156. ZEUS Collaboration, M. Derrick *et al.*, Z. Phys. C68 (1995) 569.
157. ZEUS Collaboration, M. Derrick *et al.*, Phys. Lett. B332 (1994) 228.
158. H1 Collaboration, pa02-061, submitted paper to ICHEP'96, Warsaw Poland, July 1996.
159. M.F. McDermott and G. Briskin, hep-ph/9610245, in Proceedings of the Workshop on Future Physics at HERA, Volume 2 (1996) 691.
160. K. Goulianos, "Results on diffraction", to be published in the Proceedings of the XVII International Conference on Physics in Collision, Bristol (1997), ed. H.F. Heath, World Scientific.
161. W. Buchmüller and A. Hebecker, Phys. Lett. B355 (1995) 573.
162. K. Goulianos, Phys. Lett. B358 (1995) 379; B363 (1995) 268.
163. J.C. Collins *et al.*, Phys. Rev. D51 (1995) 3182.
164. T. Gehrmann and W.J. Stirling, Z. Phys. C70 (1996) 89.
165. J. Ellis and G. Ross, Phys. Lett. B384 (1996) 293.
166. B. Andersson *et al.*, Phys. Rep. 97 (1983) 31.
167. ZEUS Collaboration, M. Derrick *et al.*, Z. Phys. C70 (1996) 391.
168. ZEUS Collaboration, M. Derrick *et al.*, Phys. Lett. B356 (1995) 129.
169. CDF Collaboration, F. Abe *et al.*, Phys. Rev. Lett 78 (1997) 2698.
170. CDF Collaboration, F. Abe *et al.*, "Measurement of diffractive dijet production at the Fermilab Tevatron", submitted to Phys. Rev. Letters, as reported in ¹⁶⁰.
171. ZEUS Collaboration, "Study of Events with an Energetic Forward Neutron in *ep* collisions at HERA", contributed paper N-641 to EPS-97 conference, Jerusalem, (1997). ZEUS FNC group, S. Bhadra *et al.*, DESY 97-006 and hep/ex 9701015.
172. ZEUS Collaboration, M. Derrick *et al.*, Phys. Lett. B384 (1996) 388.

173. ZEUS Collaboration, M. Derrick *et al.*, *Z. Phys.* C72 (1996) 47.
174. ZEUS Collaboration, M. Derrick *et al.*, *Z. Phys.* C73 (1997) 253.
175. H1 Collaboration, "The H1 Forward Proton Spectrometer", contributed paper pa17-025 to ICHEP'96, Warsaw, Poland, July 1996.
176. ZEUS Collaboration, presented by E. Barberis, Proceedings of DIS'96, Roma, ed. G. D'Agostini and A. Nigro, World Scientific (1997) 343.
177. A. Mehta, J. Phillips and B. Waugh, Proceedings of the Workshop on Future Physics at HERA, Volume 1 (1996) 704.
178. H1 Collaboration, S. Aid *et al.*, *Phys. Lett.* B379 (1996) 319.
179. ZEUS Collaboration, M. Derrick *et al.*, *Phys. Rev. Lett.* 75 (1995) 1006.
180. ZEUS Collaboration, J. Breitweg *et al.*, *Z. Phys.* C74 (1997) 207.
181. H1 Collaboration, C. Adloff *et al.*, *Z. Phys.* C74 (1997) 191.
182. ZEUS Collaboration, presented by D. Krakauer, to be published in Proceedings of Hadron Collider Physics XII, State University of New York at Stony Brook, 1997.
183. S. Kuhlmann, H. L. Lai, W. K. Tung, hep-ph/9704338.
184. CDF Collaboration, F. Abe *et al.*, *Phys. Rev. Lett.* 77 (1996) 438.
185. J. Huston *et al.*, *Phys. Rev. Lett.* 77 (1996) 444.
186. G. Altarelli *et al.*, hep-ph/9703276.
187. M. Drees, *Phys. Lett.* B403 (1997) 353.
188. Proceedings of the Workshop on Future Physics at HERA, ed. G. Ingleman, A. De Roeck and R. Klanner, DESY, Volumes 1 & 2 (1996). DESY, Hamburg, 1996.